UPPSALA
UNIVERSITET

Digital Comprehensive Summaries of Uppsala Dissertations
from the Faculty of Science and Technology 1276

Amorphous and crystalline functional materials from first principles

LEYLA ISAEVA

ACTA
UNIVERSITATIS
UPSALIENSIS
UPPSALA
2015

ISSN 1651-6214
ISBN 978-91-554-9311-0
urn:nbn:se:uu:diva-260704

Dissertation presented at Uppsala University to be publicly examined in Å80101, Ångströmlaboratoriet, Lägerhyddsvägen 1, Uppsala, Friday, 9 October 2015 at 09:00 for the degree of Doctor of Philosophy. The examination will be conducted in English. Faculty examiner: Prof. Jörg Neugebauer (Max-Planck-Institut für Eisenforschung).

Abstract

Isaeva, L. 2015. Amorphous and crystalline functional materials from first principles. *Digital Comprehensive Summaries of Uppsala Dissertations from the Faculty of Science and Technology* 1276. 105 pp. Uppsala: Acta Universitatis Upsaliensis. ISBN 978-91-554-9311-0.

This thesis deals with various functional materials from first-principles methods and is divided into two major parts according to the underlying atomic structure of the system under study. The first part of the thesis deals with the temperature-induced structural phase transitions in metallic β'-AuZn and perovskite oxide $LiOsO_3$. The former one, i.e. binary AuZn, belongs to a class of shape-memory alloys that regain their initial shape due to a reversible martensitic phase transformation. Here, by means of density functional and density functional perturbation theories, we show that the martensitic transition is due to coupling between the Fermi surface nesting and anomalies in the phonon dispersion relations. The other metallic system, perovskite $LiOsO_3$, exhibits a ferroelectric-like transition and is currently the first and sole realization of the Anderson and Blount idea. By means of *ab initio* molecular dynamics simulations, we investigate the mechanism behind this structural phase transformation.

Another part of the thesis is dedicated to modelling and characterization of topologically disordered materials on atomic level. The structural and electronic properties of amorphous W-S-N are addressed regarding its outstanding tribological properties, i.e. almost vanishing friction coefficient. Molecular dynamics “melt-and-quench” technique has been employed in order to construct a model structure of amorphous W-S-N. Further analysis of the atomic structure revealed a formation of quasi-free N_2 molecules trapped in S cages, which, together with the complex atomic structure of W-S-N, is the key to ultra-low-friction in this functional material.

In the last chapter of the thesis a magnetic class of amorphous materials is addressed. Magnetic order in amorphous Gd-Fe ferrimagnet has been shown to undergo magnezation switching driven by a femtosecond laser pulse. Here, we combine first-principles density functional theory and atomistic spin dynamics simulations to explore this phenomena. A possible mechanism behind magnetization reversal in Gd-Fe based on a combination of the Dzyaloshinskii-Moriya interaction and exchange frustration is proposed.

Keywords: first-principles theory, lattice dynamics, phase transitions, amorphous materials, tribology, ultrafast magnetism

Leyla Isaeva, Department of Physics and Astronomy, Materials Theory, Box 516, Uppsala University, SE-751 20 Uppsala, Sweden.

© Leyla Isaeva 2015

ISSN 1651-6214
ISBN 978-91-554-9311-0
urn:nbn:se:uu:diva-260704 (http://urn.kb.se/resolve?urn=urn:nbn:se:uu:diva-260704)

To my father

List of papers

This thesis is based on the following papers, which are referred to in the text by their Roman numerals.

I **Lattice dynamics of cubic AuZn from first principles**
L.Isaeva, P.Souvatzis, O.Eriksson and J.C.Lashley
Phys. Rev. B **89** 104101 (2014)

II **Understanding the phase transition in $LiOsO_3$**
V.V. Ravi Kishore, Leyla Isaeva, Abhinav Kumar, Olle Hellman, Igor Abrikosov, Olle Eriksson, Priya Mahadevan and D.D.Sarma
In manuscript

III **Amorphous W-S-N thin films: The atomic structure behind ultra-low friction**
Leyla Isaeva, Jill Sundberg, Soham Mukherjee, Christopher J. Pelliccione, Andreas Lindblad, Carlo U. Segre, Ulf Jansson, D.D.Sarma, Olle Eriksson and Krisztina Kádas
Acta Materialia **82** 84 (2015)

IV **All thermal switching of amorphous Fe-Gd alloys: analysis of structural properties and magnetization dynamics**
Raghuveer Chimata, Leyla Isaeva, Krisztina Kádas, Anders Bergman, Biplab Sanyal, J.Mentink, M.I.Katsnelson, Theo Rasing, Andrei Kirilyuk, Alexey Kimel, Olle Eriksson and Manuel Pereiro
Accepted in Phys. Rev. B

Papers not included in the thesis

V **Ab initio phonons in magnetic Ni_2MnAl**
L.Isaeva, D.Bazhanov, E.Isaev, O.Eriksson
Jpn. J. Appl. Phys. **50** 05FE07 (2011)

VI **Dynamic stabilization of cubic AuZn**
Leyla Isaeva, Olle Hellman, Jason C.Lashley, Igor Abrikosov and O.Eriksson
Accepted in Materials Today: Proceedings

VII **Interplay between effect of Mo and chemical disorder on the stability of β/β_0-TiAl phase**
David Holec, Dominik Legut, Leyla Isaeva, Petros Souvatzis, Helmut Clemen and Svea Mayer
Intermetallics **61** 85 (2015)

Reprints were made with permission from the publishers.

Contents

1 Introduction 9

2 Theoretical background 12
- 2.1 Many body problem 12
- 2.2 Density functional theory 13
  - 2.2.1 Kohn-Sham equations 14
  - 2.2.2 Exchange-correlation energy 16
  - 2.2.3 Pseudopotential method 17
  - 2.2.4 Projector augmented wave method 19
- 2.3 Molecular dynamics 21
  - 2.3.1 Integration schemes 22
  - 2.3.2 Measurement and ergodicity 24
  - 2.3.3 Thermostats 25
- 2.4 Ab initio lattice dynamics 26
  - 2.4.1 Harmonic lattice 26
  - 2.4.2 Beyond the harmonic approximation 28

3 Phase stability 30
- 3.1 Stability of β and β' phases 30
  - 3.1.1 Structural transition in shape-memory AuZn 35
- 3.2 Ferroelectric-like transition in the metallic state 42
  - 3.2.1 Understanding the phase transition in $LiOsO_3$ 43

4 A random world 49
- 4.1 Preparation and amorphous morphology 50
- 4.2 Modelling of amorphous solids 53
  - 4.2.1 Stochastic quenching method 54
- 4.3 Applications to tribology 55
  - 4.3.1 Atomic structure behind ultra-low friction in amorphous W-S-N thin films 62
- 4.4 Amorphous magnetism 70
  - 4.4.1 Ultrafast magnetization dynamics 71
  - 4.4.2 Atomistic spin dynamics at finite temperatures 78
  - 4.4.3 Magnetization switching in amorphous Gd-Fe 80

5 Summary and Outlook 90

6 Sammanfattning pa Svenska 93

7 Acknowledgements 96

References 97

1. Introduction

Functional materials are those, whose certain characteristics are tailored to serve a specific purpose. These characteristics are nothing more than a response of the system to an external stimuli. Examples of functional materials include such systems as shape memory and magnetic shape memory alloys, piezoelectrics, multiferroics etc. This thesis deals with a range of functional materials with a great diversity of structural properties and fields of applications, ranging from tribology to magnetic data storage devices. To emphasize the important role of the atomic arrangements on production and control of materials properties for various applications, the thesis is divided into two major parts based on the underlying atomic structure of considered systems, i.e. *crystalline* and *amorphous*.

The first part of the thesis is fully dedicated to *crystalline* structures, namely, metallic β'-AuZn and perovskite oxide $LiOsO_3$. The former one, i.e. β'-AuZn, is a representative of a large family of shape memory alloys. These materials are widely used in medicine as catheters for trapping “wandering” blood clots in cardiac blood vessels, in different thermomechanical and thermostatic devices, as well as in aerospace industries, such as i.e. space antennas activated upon by solar heating [1, 2]. The shape-memory alloys are characterized by a complete strain recovery when heated above a certain critical temperature. This effect is structurally associated with a temperature, pressure or magnetic field induced reversible phase transition and has been observed in many metallic systems, including Hume-Rothery phases (CuZn, AuZn, AuCd [2] etc.) and magnetic Heusler alloys (NiMnIn [3], NiFeGa [4], NiMnGa [5] etc.), suggesting an interplay between the electronic and lattice dynamical properties. A theoretical analysis of the microscopical mechanism behind such transitions is something we address in AuZn system from first principles.

Perovskite oxide $LiOsO_3$, is another highly ordered system and our interest in this material is purely fundamental, as $LiOsO_3$ undergoes a ferroelectric-like transition in the metallic state. At first glance ferroelectric type transitions and the metallic state seem to be incompatible due to conduction electron screening of the internal electric fields. However, back in 1965 it was proposed by Anderson and Blount that in certain cases structural phase transitions in the metallic state can be ferroelectric-like [6]. Such “ferroelectric” phase transition has been very recently experimentally observed in the metallic $LiOsO_3$, making it the first known realization of the Anderson and Blount’s idea [7]. There are currently several theories explaining this ”ferroelectricity”, however, the type of the phase transition (order-disorder or displacive type), and lattice dynamical properties of $LiOsO_3$ at finite temperatures have not been studied yet. Hence, by means of first-principles molecular dynamics simulations we investigate the nature of this phase transition in details.

The second half of this thesis deals with the theoretical modeling and characterization of topologically disordered, i.e. *amorphous* materials. There are many well-known industrial application of amorphous materials, including amorphous Se films as xerographic photoreceptors in copying machines, ultratransparent glass fibers for optical communications, Ge-Sb-Te thin films for digital versatile disks (DVD), amorphous hydrogenated silicon, a-Si:H, for solar cells and thin-film transistors (TFT), to name a few [8]. Here, we focus on other two important fields of application, namely, tribology and data storage technologies.

First we address the applications of amorphous materials in the field of tribology. This branch of materials science deals with interacting surfaces in relative motion, and related phenomena, such as friction, wear and lubrication. Liquid lubricants are the first and oldest known example of lubrication. However, liquid lubricants containing various chemical additives are not always the best choice for engineering applications, especially those operating at extreme conditions. In this case, a use of coating materials with low-friction properties, i.e. solid lubricants, is optimal. Transition-metal dichalcogenides (TMDC), such as WS_2, MoS_2 etc. are well-known intrinsic solid lubricants, and their low-friction properties are due to the layered and highly anisotropic atomic structure [9, 10]. Different additional elements have been combined with TMDC's to obtain a stable surface for easier WS_2 tribofilm formation. At the same time, addition of high amount of N introduces a disorder in the structure, so it becomes amorphous [11]. Amorphous W-S-N thin films with N content of about 37 at.% have been shown to exhibit ultra-low friction by formation of WS_2 tribofilm, i.e. a thin lubricating layer formed directly in the tribological contact, with virtually vanishing friction coefficient ($\mu < 0.003$) [12]. We, therefore, model amorphous structure of W-S-N to investigate the local atomic arrangement in this system which give such an optimum condition for the tribofilm formation and, as a result, an extremely low friction.

Storing and processing information in magnetic data storage materials, where the spin of the electron serves as an information carrier, are among the motivations to study spin dynamics. The speed at which the spins can be reversed determines how fast the information can be written. Current magnetic data storage devices offer charactersitic magnetization reversal time on the order of nanoseconds, which allows to write about a billion bits of information per second. To achieve faster reversal time high magnetic or damping fields can be used, however, for industrial applications neither of these methods are favorable. Another way to control magnetization switching is by applying femtosecond laser pulse as observed in an amorphous ferrimagnet GdFeCo [13]. In this case magnetization switching is thermally induced and does not involve any external magnetic field, and allows faster spin reversal compared to the present technologies. Recently, two different magnetization dynamics have been experimentally obtained for Gd and Fe sublattices in GdFeCo system (with 9.5 at.% Co) where depending on the homogeneity of the probed region either Gd, or Fe sublattice switched its magnetization first [14]. These experiments suggest a possibility to manipulate magnetic bits by femtosecond laser pulses. In the final part of the thesis we attempt to understand the microscopic mechanism of magnetization switching in amorphous ferrimagnetic Gd-Fe alloy driven by femtosecond laser pulse, and take into account its underlying topologically disordered structure.

This thesis is organized as follows. In Chapter 2 the basic concepts of the density functional theory is given, along with the backgrounds of molecular dynamics simulations and lattice vibrations in crystalline solids. Structural transitions in shape-memory AuZn and metallic perovskite oxide $LiOsO_3$ are addressed from first principles in Chapter 3. Chapter 4 deals with amorphous materials. In this chapter various approaches for modelling of amorphous structures on atomic level, including molecular dynamics simulations and stochastic quenching method, are also reviewed. The rest of the chapter deals with the origin of the ultra-low friction in triboactive W-S-N films and magnetization reversal in ferrimagnet Gd-Fe. Summary and outlook are given in Chapter 5.

2. Theoretical background

The aim of this chapter is to provide a reader with the theoretical backgrounds and methods used throughout the thesis. First, we describe the density functional approach to many-body problem in Section 2.1. Next, in Section 2.2 we give a short introduction to *ab initio* molecular dynamics and discuss related concepts of ergodicity and Lyapunov instability. Finally, the background behind the dynamical theory of lattices, as well as lattice-dynamical calculations using the density functional perturbation theory and frozen phonon techniques are discussed in Section 2.3.

2.1 Many body problem

The dynamics of non-relativistic many-body system consistent of N electrons and M nuclei is governed by time-dependent Schrödinger equation

$$i\hbar\frac{\partial\Psi}{\partial t}=\hat{H}\Psi, \tag{2.1}$$

where

$$\Psi=\Psi(\mathbf{r}_1,...,\mathbf{r}_N;\mathbf{R}_1,...,\mathbf{R}_M) \tag{2.2}$$

is a many-body wavefunction that depends on spatial positions $\{\mathbf{r}\}$ and $\{\mathbf{R}\}$ of electrons and ions. The explicit form of the Hamiltonian reads as follows

$$\begin{aligned} H=&-\frac{\hbar^2}{2m}\sum_i\frac{\partial^2}{\partial\mathbf{r}_i{}^2}-\sum_I\frac{\hbar^2}{2M_I}\frac{\partial^2}{\partial\mathbf{R}_I{}^2}+\frac{1}{2}\sum_{i\neq j}\frac{e^2}{|\mathbf{r}_i-\mathbf{r}_j|} \\ &-\sum_{i,k}\frac{eZ_k}{|\mathbf{r}_i-\mathbf{R}_J|}+\frac{1}{2}\sum_{I\neq J}\frac{Z_IZ_Je^2}{|\mathbf{R}_I-\mathbf{R}_J|}, \end{aligned} \tag{2.3}$$

where m is the mass of an electron, while M_I and Z_I refer to the mass and atomic number of Ith nucleus. The first and second terms in the Hamiltonian (2.3) are the kinetic energies associated with the motion of electrons and nuclei, and the third, forth and fifth terms describe the electron-electron, electron-nuclei and nuclei-nuclei electrostatic interactions, respectively.

In practice, the many-body Schrödinger equation is not possible to solve, as the number of electrons and nuclei in macroscopic solids is of order $\sim 10^{23}$. As a result, the quantum mechanical wave function depends on an enormous number of variables, and the additional complication arise from the fact that the motion of particles are not independent. This is known as the *many-body problem.* In attempting to approach this problem, several approximations should be introduced. The first step is to separate electronic and nuclear degrees of freedom based on the *Born-Oppenheimer (adiabatic) approximation* [15], which assumes that the lighter electrons ($M_I >> m$) adiabatically adjust to the motion of heavier nuclei, rapidly relaxing to the instantaneous ground-state. With the Born-Oppenheimer approximation it is possible to decouple the electronic and nuclear degrees of freedom, and to solve the electronic problem in an external potential of frozen nuclei

$$H = -\frac{\hbar^2}{2m}\sum_i \frac{\partial^2}{\partial \mathbf{r}_i{}^2} + \frac{1}{2}\sum_{i \neq j} \frac{e^2}{|\mathbf{r}_i - \mathbf{r}_j|} - \sum_{i,k} \frac{eZ_k}{|\mathbf{r}_i - \mathbf{R}_J|}. \tag{2.4}$$

The complexity of the initial problem is now significantly reduced. However, the problem still remains too difficult to solve, as the motion of an electron is influenced by other electrons via the electron-electron correlation term. Further enormous simplification is the introduction of the *density functional theory* by Kohn and Sham [16, 17], which replaces the many-body problem in Eq.(2.4) of $3N$ variables with an equation for the electron density consisting of only 3 space variables, which we shortly discuss in the following subsection.

2.2 Density functional theory

The basic idea behind the density functional theory is to replace the problem for a system of interacting electrons in an external field to an effective potential problem of non-interacting quasiparticles. It is required, that the effective potential should reproduce the same ground state density as the one of the interacting system. Once the effective potential is known the problem of non-interacting quasiparticles subjected to the effective potential is immediately solved using one-electron Schrödinger equation. The original formulation of the density functional theory is based on the two following theorems.

Theorem 1

For any system of interacting particles in external potential $v_{ext}(\mathbf{r})$, there is a one-to-one correspondence between the ground state density $n(\mathbf{r})$ and the external potential $v_{ext}(\mathbf{r})$.

In other words, the potential $v_{ext}(\mathbf{r})$ is determined uniquely by the ground state particle density $n(\mathbf{r})$, up to a trivial additive constant. Hence, all the observables may be expressed in terms of the ground state electron density $n(\mathbf{r})$, and in this sense, the electron density carries as much information as the wave function.

Theorem 2

For any external potential $v_{ext}(\mathbf{r})$ there exists a universal functional $F_{HK}[n(\mathbf{r})]$ such that the total energy functional

$$E_{tot}[n(\mathbf{r})] = F_{HK}[n(\mathbf{r})] + \int v_{ext}(\mathbf{r})n(\mathbf{r})d\mathbf{r}, \tag{2.5}$$

is minimized by the ground-state electron density corresponding to the external potential $v_{ext}(\mathbf{r})$. Furthermore, the value of the minimum corresponds to the ground-state energy.

2.2.1 Kohn-Sham equations

With these two theorems Kohn and Sham were able to map the interacting problem onto the equivalent non-interacting one. The functional form of the total energy reads as

$$E_{tot}[n] = T[n] + E_H[n] + E_{xc}[n] + \int v_{ext}(\mathbf{r})n(\mathbf{r})d\mathbf{r}, \tag{2.6}$$

where $v_{ext}(\mathbf{r})$ is the external potential, $T[n]$ is the kinetic energy, $E_H[n]$ is the Hartee energy, and $E_{xc}[n]$ takes into account all the many body effects. An explicit form of the exchange-correlation energy functional ($E_{xc}[n]$) is unknown, but might be approximated as discussed further in this chapter. We now seek to find the electron density $n(\mathbf{r})$ that minimizes the energy functional $E_{tot}[n]$ (Eq. (2.5)). For this we define the Lagrangian function $\mathscr{L}$ and perform a minimization procedure via the Lagrange multiplier method [18]

$$\begin{aligned} \mathscr{L} &= E_{tot}[\phi_i] - \sum_i \varepsilon_i \left(\int \phi_i^*(\mathbf{r})\phi_i(\mathbf{r})d\mathbf{r} - 1 \right) \\ \delta\mathscr{L} &= \int \frac{\delta\mathscr{L}}{\delta n(\mathbf{r})}\delta n(\mathbf{r})d\mathbf{r} = 0, \end{aligned} \tag{2.7}$$

where ε_i are Lagrange multiplyers, which physical meaning will become clear later. The total number of particles, N, is the constraint in this optimization, i.e.

$$n(\mathbf{r}) = \sum_i^N \phi_i(\mathbf{r})^*\phi_i(\mathbf{r}), \quad \int n(\mathbf{r})d\mathbf{r} = N. \tag{2.8}$$

Here, single-particle orbitals $\phi_i(\mathbf{r}), i = 1,..,N$ define the N-particle ground state with density $n(\mathbf{r})$, and the variation of the electronic density with respect to the orbitals $\phi_i(\mathbf{r})$ is

$$\delta n(\mathbf{r}) = \sum_i \left(\delta\phi_i\phi_i{}^* + \phi_i\delta\phi_i{}^*\right). \tag{2.9}$$

The variation of the Lagrangian $\mathscr{L}$ with respect to ϕ_i^* should vanish at the minimum of action

$$\frac{\delta\mathscr{L}}{\delta\phi_i^*} = \frac{\delta E_{tot}}{\delta\phi_i^*} - \varepsilon_i\phi_i = 0, \tag{2.10}$$

and, hence, we ought to find the exact form of $\delta E_{tot}/\delta\phi_i^*$. This is done by performing the variation of the functionals in Eq. (2.6) with respect to ϕ_i^*. The kinetic energy functional can be defined as [1]

$$T[n] = -\frac{1}{2}\sum_i \langle\phi_i|\nabla^2|\phi_i\rangle = -\frac{1}{2}\sum_i \int \phi_i^* \frac{\partial^2}{\partial\mathbf{r}^2}\phi_i d\mathbf{r}, \tag{2.11}$$

and, therefore, the corresponding variation of $T[n]$ is

$$\begin{aligned}\frac{\delta T[n]}{\delta\phi_i^*} = \frac{\delta}{\delta\phi_i^*}\left(-\frac{1}{2}\sum_i \int \phi_i^* \frac{\partial^2}{\partial\mathbf{r}^2}\phi_i d\mathbf{r}\right) &= -\frac{1}{2}\frac{\partial^2}{\partial\mathbf{r}^2}\phi_i \\ &= \frac{\delta T[n]}{\delta n(\mathbf{r})}\frac{\delta n(\mathbf{r})}{\delta\phi_i^*} = \frac{\delta T[n]}{\delta n(\mathbf{r})}\phi_i.\end{aligned} \tag{2.12}$$

Next, variation of the Hartree functional $H[n]$ reads as

$$\frac{\delta E_H[n]}{\delta\phi_i^*} = \frac{\delta E_H[n]}{\delta n(\mathbf{r})}\frac{\delta n(\mathbf{r})}{\delta\phi_i^*} = \underbrace{\frac{\delta E_H[n]}{\delta n(\mathbf{r})}}_{v_H(\mathbf{r})}\phi_i. \tag{2.13}$$

The last functional derivative we are interested in, is the one for the exchange-correlation $E_{xc}[n]$

$$\frac{\delta E_{xc}[n]}{\delta\phi_i^*} = \frac{\delta E_{xc}[n]}{\delta n(\mathbf{r})}\frac{\delta n(\mathbf{r})}{\delta\phi_i^*} = \underbrace{\frac{\delta E_{xc}[n]}{\delta n(\mathbf{r})}}_{v_{xc}(\mathbf{r})}\phi_i. \tag{2.14}$$

Combining the derivatives with respect to the single-orbital ϕ_i^* (Eq. (2.12)-(2.14)) it is straightforward to obtain the following expression for the variation of the total energy $\delta E_{tot}/\delta\phi_i^*$

$$\frac{\delta E_{tot}[n]}{\delta\phi_i^*} = \left(-\frac{1}{2}\frac{\partial^2}{\partial\mathbf{r}^2} + \underbrace{v_H(\mathbf{r}) + v_{xc}(\mathbf{r}) + v_{ext}(\mathbf{r})}_{v_{eff}(\mathbf{r})}\right)\phi_i, \tag{2.15}$$

and by inserting the r.h.s of Eq.(2.15) back to Eq.(2.10), we obtain Schrödinger-like equations for the quasiorbitals ϕ_i

$$\left[-\frac{1}{2}\frac{\partial^2}{\partial\mathbf{r}^2} + v_{eff}[n(\mathbf{r})]\right]\phi_i = \varepsilon_i\phi_i. \tag{2.16}$$

Equations (2.16) describe a system of non-interacting quasiparticles in an external effective potential $v_{eff}(\mathbf{r})$, with the Lagrange multipliers ε_i representing

---

[1] Here, for the sake of simplicity, we set $m = \hbar = 1$.

Kohn-Sham eigenvalues. While deriving Eq.(2.16) we have also assumed that the quasiorbitals ϕ_i produce the ground state electronic density of a system of interacting particles (Eq. 2.8). Hence, Eqs. (2.16) and (2.8) are coupled and form what is known as Kohn-Sham equations. Once an explicit form of the exchange-correlation functional is known, the Kohn-Sham equations can be solved iteratively in a self-consistent fashion to obtain the electronic ground state energy. It can be shown that the ground-state total energy $E_{tot}[n(\mathbf{r})]$ can be equivalently expressed in terms of Kohn-Sham eigenvalues

$$E_{tot}[n(\mathbf{r})] = \sum_i \varepsilon_i - E_H[n(\mathbf{r})] + E_{xc}[n(\mathbf{r})] - \int n(\mathbf{r}) v_{xc}(\mathbf{r}) d\mathbf{r}. \tag{2.17}$$

The Kohn-Sham scheme is, in principle, exact. However, the form of the exchange-correlation energy functional $E_{xc}[n(\mathbf{r})]$ is *a priori* unknown. Various approximations to $E_{xc}[n(\mathbf{r})]$ have been developed and they are shortly discussed in the next subsection.

2.2.2 Exchange-correlation energy

Local density approximation

Already in their original paper Kohn and Sham [17] proposed the local density approximation (LDA) for the exchange-correlation energy. It assumes that the electron density varies slowly in space, so that it can be approximated by the density of the homogenous electron gas. With this assumption, the exchange-correlation functional reads as

$$E_{xc}^{LDA}[n] = \int \varepsilon_{xc}(n)|_{n=n(\mathbf{r})} n(\mathbf{r}) d\mathbf{r}, \tag{2.18}$$

where ε_{xc} is the exchange-correlation energy per particle of a homogenous electron gas with density $n(\mathbf{r})$. Numerical results for ε_{xc} can be obtained from Monte-Carlo simulations and have been parametrized by Perdew and Zunger in a simple analytical form [19]. Corresponding exchange-correlation potential is given by

$$v_{xc}^{LDA}[n] = \left(\varepsilon_{xc}(n) + n \frac{d\varepsilon_{xc}(n)}{dn} \right) \Bigg|_{n=n(\mathbf{r})}. \tag{2.19}$$

The form of the exchange-correlation energy (2.18) becomes exact in the limit of high electronic density $n(\mathbf{r})$, as well as in the case of a slowly varying charge density distribution. Despite its simplicity, the local density approximation works surprisingly well and accurately describes structural and vibrational properties of weakly correlated systems, such as simple metals and semiconductors. However, there are several well-known drawbacks of LDA, including large overestimation of the crystal cohesive and molecular binding energies up to 20 %, as well as underestimation of the optical band gap in insulators. LDA often results in smaller lattice parameters (typically, within 1-3 %) compared to the experimental ones due to overbinding. Another limitation of the LDA approach is that it fails to describe properties of strongly-correlated materials, such as transition-metal oxides.

Generalized gradient approximation

It is natural to extend the local density approximation by taking into account gradient corrections to the charge density distribution, as it is done within generalized gradient approximation (GGA)

$$E_{xc}^{GGA}[n] = \int \varepsilon_{xc}(n, |\nabla n|)|_{n=n(\mathbf{r})} n(\mathbf{r}) d\mathbf{r}. \tag{2.20}$$

There is no unique way to define the gradient of the charge density distribution and different forms of the exchange-correlation functional exist. Most popular parametrizations are those proposed by Perdew and Wang [20], also by Perdew, Burke and Ernzerhof [21]. Generalized gradient approximation typically underbinds, resulting in larger lattice parameters (within 1-3%). The drawback of GGA is that it gives too small bulk moduli, and, as well as LDA, fails describing band gaps in insulators and semiconductors.

2.2.3 Pseudopotential method

To solve the Kohn-Sham equations, the wave function needs to be expanded in a known *basis set*. In real materials, wave functions of electrons have a complicated behavior in different regions of space. The wave functions of the valence electrons are very smooth, while the wave functions of the core electrons due to large attractive potential of the nucleus have highly oscillating form (Figure 2.1). It is therefore a rather nontrivial task to construct such basis function which could accurately describe both the “wiggles” in the core region and smooth behavior in the valence band. The main idea of the pseudopotential method is to consider the core electrons as *frozen*, as they do not participate in bonding and are weakly influenced by it, and replace the highly oscillating core wave functions to a smooth wave function without any node in the core region. This saves time of the electronic structure calculation without sacrificing the quality of the calculation.

The work by Phillips and Kleiman [22] laid the theoretical background of the pseudopotential method and we describe its main ideas here. Let us illustrate how to construct a pseudopotential in terms of the exact core $|\phi_c\rangle$ and valence states $|\phi_v\rangle$, which satisfy Schrödinger equation for the appropriate single-particle Hamiltonian

$$H|\psi_v\rangle = \varepsilon_v|\psi_v\rangle, \quad H|\psi_c\rangle = \varepsilon_c|\psi_c\rangle. \tag{2.21}$$

Here ε_v and ε_c are eigenvalues of the valence and core wave functions, respectively. Now let us define a new set of valence states (*pseudostates* ϕ_v^{ps}) through

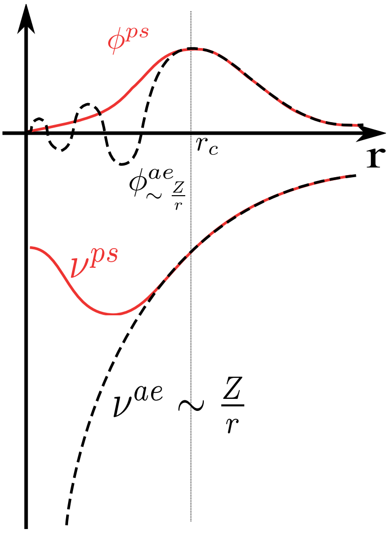

Figure 2.1. Schematic illustration of the pseudopotential (v^{ps}) and the corresponding pseudo wave function (ϕ^{ps}) in reference to the original all-electron potential v^{ae} and the orbital ϕ^{ae}. The all-electron and the pseudo wave functions match outside the core radius r_c.

the following relation

$$|\phi_v^{ps}\rangle = |\phi_v\rangle + \sum_c a_c |\phi_c\rangle, \tag{2.22}$$

where $a_c = \langle\phi_c|\phi_v^{ps}\rangle$ are the expansion coefficients. Inserting this expansion into the Schrödinger equation for the valence states ϕ_v we obtain

$$H|\phi_v\rangle = H|\phi_v^{ps}\rangle - \sum_c a_c H|\phi_c\rangle = H|\phi_v^{ps}\rangle - \sum_c \varepsilon_c |\phi_c\rangle\langle\phi_c|\phi_v^{ps}\rangle, \tag{2.23}$$

which is further reduced to

$$\left(H - \sum_c \varepsilon_c |\phi_c\rangle\langle\phi_c|\right)|\phi_v^{ps}\rangle = H|\phi_v\rangle = \varepsilon_v|\phi_v\rangle. \tag{2.24}$$

On the other hand, we can make use of the expansion of the valence wave function

$$\varepsilon_v|\phi_v\rangle = \varepsilon_v|\phi_v^{ps}\rangle - \varepsilon_v \sum_c \langle\phi_c|\phi_v^{ps}\rangle|\phi_c\rangle \tag{2.25}$$

and rewrite (2.24) as

$$\left(H - \sum_c \varepsilon_c |\phi_c\rangle\langle\phi_c|\right)|\phi_v^{ps}\rangle = \varepsilon_v|\phi_v^{ps}\rangle - \varepsilon_v \sum_c \langle\phi_c|\phi_v^{ps}\rangle|\phi_c\rangle. \tag{2.26}$$

Now it is possible to define a new energy-dependent pseudo-Hamiltonian H^{ps}

$$H^{ps} = H + \sum_{c} (\varepsilon_v - \varepsilon_c) |\phi_c\rangle\langle\phi_c|. \tag{2.27}$$

The Schrödinger-like equation for the new pseudo wave function $|\phi_v^{ps}\rangle$ takes the form

$$\left[-\frac{1}{2}\frac{\partial^2}{\partial \mathbf{r}^2} + v^{ps} \right] |\phi_v^{ps}\rangle = \varepsilon |\phi_v^{ps}\rangle, \tag{2.28}$$

where the pseudopotential v^{ps} is

$$v^{ps} = v_{eff} + \sum_{c} (\varepsilon_v - \varepsilon_c) |\phi_c\rangle\langle\phi_c|. \tag{2.29}$$

Therefore, the new pseudostates ϕ_v^{ps} are solutions of a single-particle equation with a modified potential v^{ps} (Eq.2.29), but with the same eigenvalues ε_v as the initial states. As a result of the transformation (Eq.2.22) we have removed the core wiggles out of the electronic structure problem at the expense of introducing an energy-dependent non-local pseudopotential. However, the drawback of the method is that the information about the full wave function close to the nuclei is completely lost.

While constructing the pseudopotential such criteria as *softness* and *transferability* have to be fulfilled [23, 24]. A *soft* pseudopotential requires only few plane waves, while *transferability* implies that a psedopotential can be used regardless the local environment, i.e. in molecules, periodic solids, surfaces etc. When applied to d- or f-electron systems, or treating semicore states as valence as often necessary for early transition metals, the pseudopotential method in combination with a plane-waves basis set may result in complications. The pseudopotentials become very "hard" and requiring a large basis set, which may affect its transferability. The idea of *ultrasoft* pseudopotentials allowing smaller cutoff kinetic energies, as introduced by Vanderbilt, overcomes this problems by relaxing the norm-conservation condition [25].

2.2.4 Projector augmented wave method

The projector augmented method (PAW) is an all-electron method that combines the plane-wave pseudopotential approach with the augmented-wave method [26]. The central idea of the PAW method is an introduction of the linear transformation $\mathscr{T}$ that maps the exact *all-electron* wave function Ψ to an auxiliary wave function $\tilde{\Psi}$, much like in the pseudopotential method

$$|\Psi\rangle = \mathscr{T} |\tilde{\Psi}\rangle. \tag{2.30}$$

Knowing the transformation $\mathscr{T}$ from the auxiliary wave function $\tilde{\Psi}$ to the exact all-electron Ψ wave function, it is straightforward to obtain the expectation value $\langle A \rangle$ of an operator A related to a certain physical quantity

$$\langle A \rangle = \langle \tilde{\Psi} | \tilde{A} | \tilde{\Psi} \rangle, \quad \tilde{A} = \mathscr{T}^{\dagger} A \mathscr{T}. \tag{2.31}$$

Applying the variational principle with respect to the auxiliary wave function $\tilde{\Psi}$, we arrive at the transformed Kohn-Sham equation

$$\mathscr{T}^{\dagger} H \mathscr{T} | \tilde{\Psi} \rangle = \varepsilon_i \mathscr{T}^{\dagger} \mathscr{T} | \tilde{\Psi} \rangle, \tag{2.32}$$

and may introduce the pseudo Hamiltonian $\tilde{H} = \mathscr{T}^{\dagger} H \mathscr{T}$ and overlap operator $\tilde{O} = \mathscr{T}^{\dagger} \mathscr{T}$, accordingly. The linear transformation $\mathscr{T}$ differs from the unity by a sum of local atom centered contributions $\hat{\mathscr{T}}_R$

$$\mathscr{T} = 1 + \sum_R \hat{\mathscr{T}}_R. \tag{2.33}$$

Here each local contribution $\hat{\mathscr{T}}_R$ acts within some augmented region Ω_R enclosing an atom centered at R. This implies that the all-electron (Ψ) and auxiliary ($\tilde{\Psi}$) wave functions match outside the augmentation region (core region in the pseudopotential approach). Let $|\phi_i\rangle$ be a solution of the Schrödinger equation for an isolated atom. Furthermore, let us assume that $|\tilde{\phi}_i\rangle$ is a solution of the Schrödinger equation with the one atom potential replaced by a pseudopotential. As noted, within the augmented region Ω_R the real wave functions $|\phi_i\rangle$ are replaced by $|\tilde{\phi}_i\rangle$ and outside the augmented region they should match, i.e. $|\phi_i\rangle = |\tilde{\phi}_i\rangle$. The local operator $\mathscr{T}_R$ is then defined as

$$|\phi_i\rangle = (1 + \hat{\mathscr{T}}_R) |\tilde{\phi}_i\rangle. \tag{2.34}$$

We make use of the fact that inside each augmented region Ω_R, pseudo wave functions $\tilde{\Psi}$ can be expanded into pseudo partial waves as

$$|\tilde{\Psi}\rangle = \sum_i |\tilde{\phi}_i\rangle a_i. \tag{2.35}$$

Further, as $|\phi_i\rangle = \mathscr{T} |\tilde{\phi}_i\rangle$, the all-electron wave function takes the following form

$$|\Psi\rangle = \mathscr{T} |\tilde{\Psi}\rangle = \sum_i |\phi_i\rangle a_i. \tag{2.36}$$

As a result, we can express the all electron wave function in terms of pseudo wave function and pseudo partial wave functions as

$$|\Psi\rangle = |\tilde{\Psi}\rangle - \sum_i |\tilde{\phi}_i\rangle a_i + \sum_i |\phi_i\rangle a_i. \tag{2.37}$$

The transformation $\mathscr{T}$ is linear, hence the expansion coefficients a_i are nothing more than just scalar products of the pseudo wave function with projector functions $\langle \tilde{p}_i |$, localized inside the augmentation spheres

$$a_i = \langle \tilde{p}_i | \tilde{\Psi} \rangle. \tag{2.38}$$

The projector operators must fulfill the completeness and the orthogonality conditions within the augmentation region Ω_R

$$\begin{aligned} \sum_i |\tilde{\phi}_i\rangle\langle\tilde{p}_i| &= 1, \\ \langle\tilde{p}_i|\tilde{\phi}_j\rangle &= \delta_{ij}. \end{aligned} \tag{2.39}$$

Finally, we can establish a linear transformation between the all-electron and the pseudo wave functions as

$$\hat{\mathscr{T}} = \hat{1} + \sum_i (|\phi_i\rangle - |\tilde{\phi}_i\rangle)\langle\tilde{\phi}_i|. \tag{2.40}$$

and with this transformation the all-electron wave function can be obtained from the pseudo wave functions via

$$|\Psi\rangle = |\tilde{\Psi}\rangle + \sum_i (|\phi_i\rangle - |\tilde{\phi}_i\rangle)\langle\tilde{\phi}_i|\tilde{\Psi}\rangle. \tag{2.41}$$

By this decomposition, the original wave function is separated into the smooth auxiliary and rapidly oscillating wave functions, which contribute only to a small regions. Unlike to pseudopotential method, for which the Kohn-Sham equations are solved for the valence state only, the PAW method also maps the core states to some manageable wave functions and is, therefore, an *all-electron* method.

2.3 Molecular dynamics

An experimental setup typically consists of the following stages: preparation and initialization of the system of interest followed by the actual measurement of the desired observables. *Ab initio* molecular dynamics due to clear parallels to experiment is sometimes called a “virtual laboratory” [27], where a system of interest, apparatus for manipulations over this system (for example, thermostats to control the temperature) and a measurement tool are represented *in silico*. This analogy with experimental setup makes molecular dynamics a robust and versatile method for a broad spectrum of applications. This includes studies of properties of polymers and macromolecular materials, description of dynamical processes including chemical reactions, diffusion, simulations of water and aqueous solutions, photophysics and photochemistry, as well as various applications of molecular dynamics in life sciences and physics of matter at extreme conditions. In this thesis molecular dynamics simulations have been employed for designing amorphous triboactive W-S-N thin films (Paper III) and temperature-induced ferroelectric-like structural transition in metallic $LiOsO_3$ (Paper II).

Statistical mechanics and classical Newtonian dynamics form the basis of molecular dynamics simulations. Nuclei of a many-body system are considered as classical point objects, and hence, their motion obeys Newton’s second law

$$m\ddot{\mathbf{r}}_\mathbf{i} = -\frac{\partial E}{\partial \mathbf{r}_\mathbf{i}} = \mathbf{f}_\mathbf{i}(\{\mathbf{r}_\mathbf{j}\}), \tag{2.42}$$

where $\mathbf{f}_\mathbf{i}$ represent forces due to other nuclei at positions $\mathbf{r}_\mathbf{j}$ ($\mathbf{r}_\mathbf{i} \neq \mathbf{r}_\mathbf{j}$). In classical formulation of molecular dynamics, forces are obtained through the effective pair potentials, such as Lennard-Jones, Morse, or empirical potentials to include certain effects. Advances in electronic structure theory made it possible to derive forces without any empirical input, but purely from first-principles, and allowing *ab initio* molecular dynamics (AIMD) simulations. Depending on how the nuclei and electronic degrees of freedom are treated within AIMD one can distinguish between Car-Parinello and Born-Oppenheimer molecular dynamics [28]. The Car-Parinello algorithm solves the quantum electronic problem and the dynamics of nuclei simultaneously. This is achieved by constructing a fictitious Lagrangian with a fictitious kinetic energy for the electronic states. Born-Oppenheimer molecular dynamics, which is extensively used in the thesis, instead, is based on a separation of electronic and nuclei degrees of freedom. In this way, the dynamical evolution of the nuclear system is defined by the electronic potential energy surface. The electronic problem itself is solved using the Kohn-Sham equations and forces acting on the nuclei are given by the Hellman-Feynman (force) theorem

$$\mathbf{f} = -\langle \psi | \frac{\partial \hat{\mathbf{H}}}{\partial \mathbf{r}} | \psi \rangle, \tag{2.43}$$

where $\hat{\mathbf{H}}$ is the Hamiltonian of the many-body system, and ψ is the corresponding ground-state wave function.

An algorithm which carries the most essential steps of molecular dynamics simulations can be shortly described as follows. A system is prepared at given conditions, such that the number of particles, density, temperature, time step for integration equation of motions and etc. are defined. Next, the system is initialized with certain initial positions and momenta. Further, forces acting on each nuclei are calculated numerically and then the equations of motion are integrated. These two last steps are repeated for a sufficient number of timesteps until the system is equilibrated, so that the desired averages can be extracted. The schemes for numerical integration of equations of motion are discussed below.

2.3.1 Integration schemes

Let us consider a many-body system with conserved number of particles N. Classical equations of motion for such system

$$\dot{\mathbf{r}} = \frac{\mathbf{p}}{m}, \qquad \dot{\mathbf{p}} = \mathbf{f} \tag{2.44}$$

form $6N$ coupled differential equations for position $\mathbf{r}$ and conjugate momenta $\mathbf{p}$. These equations of motion are time-reversible, i.e. invariant with respect to interchange of t to $-t$, and energy conserving. To solve these equation of motion various integration schemes are applied with the simplest one being the Verlet algorithm. This algorithm relates position of a particle at time step $t+\Delta t$ with its positions at previous timesteps separated by Δt

$$\mathbf{r}(t+\Delta t) \approx 2\mathbf{r}(t) - \mathbf{r}(t-\Delta t) + \frac{\mathbf{f}(t)}{m}\Delta t^2 + O(\Delta t^4), \tag{2.45}$$

where Δt defines a timestep between two consecutive force calculations. This relation can be obtained from the Taylor expansion of position of a particle at two times, i.e. $\mathbf{r}(t+\Delta t)$ and $\mathbf{r}(t-\Delta t)$, and further subtraction of one expression from another. The power of such integration scheme is that the terms of odd power are cancelled out, thus reducing a truncation error in Eq.(2.45) from $\mathscr{O}(\Delta t^3)$ down to $\mathscr{O}(\Delta t^4)$ order. When the trajectory is known one can also derive velocities

$$\mathbf{v}(t) = \frac{\mathbf{r}(t+\Delta t) - \mathbf{r}(t-\Delta t)}{2\Delta t} + O(\Delta t^2). \tag{2.46}$$

The velocities are not important for Verlet algorithm, however, they are used to obtain the instantaneous temperature $T(t)$ through the kinetic energy. It can be shown that Verlet algorithm is time-reversible and area-preserving in phase spase, i.e. a space of all positions and momenta. Another advantage of the Verlet algorithm is that it has a small energy drift for long time simulations, in contrast to a modest energy conservation for short runs.

In molecular dynamics simulations force calculation is the most time consuming task. Thus, at first glance, larger time steps Δt might seem preferable compared to smaller ones, due to less frequent force calculation. It is also important that the chosen integration scheme is time-reversible in analogy with the classical equation of motion (2.44). However, it turns out that many algorithms are not time-reversible, but can become such only in the limit of infinitely short time steps, which is numerically not feasible. As mentioned above, equations of motion are energy-conserving, thereby, the integration scheme should also satisfy this criterion. When choosing the integration scheme a long-time accuracy should be preferred over the short-time one.

Except the Verlet algorithm, discussed above, there is a number of higher-order schemes, such as “leap frog” and Beeman algorithms [29]. These integration schemes demand larger computational cost, as more memory is required to collect forces and corresponding high-order derivatives. In contrast to low-order integration schemes, higher-order algorithms usually exhibit a satisfactory energy conservation for a few timesteps, but they result in an undesirable energy drift for long-time runs. Hence, the lower order integration algorithms are usually preferred over the higher-order ones. Time reversability together with the small energy drift over the simulation time, makes the Verlet algorithm superior compared to the higher-order schemes.

Another important issue to discuss regarding the equations of motions, is the stability of their solution. For a many-body particle system, the phase space trajectories are extremely sensitive with respect to the initial conditions. The separation $\Delta\mathbf{r}(t)$ between the two trajectories obtained from the same set of equations of motions, but with slightly different initial conditions $\Delta\mathbf{r}_0$, is linear in t for small times. However, for sufficiently long time it diverges exponentially

$$|\Delta\mathbf{r}(t)| \sim \Delta\mathbf{r}_0 e^{\lambda t}. \tag{2.47}$$

This is known as Lyapunov instability, and the exponential coefficient λ is the so-called Lyapunov exponent. Due to this instability one can only accurately predict the trajectories for a short simulation time. At first sight, this ruins the validity of the results obtained from molecular dynamics simulations. However, since we are interested in statistical averages, we are satisfied with the wrong trajectories as long as they give the correct average values.

2.3.2 Measurement and ergodicity

In statistical mechanics the average of any function A, which depends on position $\mathbf{r}$ and conjugated momenta $\mathbf{p}$, is determined through ensemble averaging, i.e. averaging over all possible states of N-particle system

$$\langle A\rangle_{ensemble} = \frac{\int d\mathbf{p}^N d\mathbf{r}^N A(\mathbf{r}^N,\mathbf{p}^N) exp(-H(\mathbf{r}^N,\mathbf{p}^N)/k_BT)}{\int d\mathbf{p}^N d\mathbf{r}^N exp(-H(\mathbf{r}^N,\mathbf{p}^N)/k_BT)}. \tag{2.48}$$

It is extremely difficult to work with this expression. Molecular dynamics instead employs an aproach similar to the experimental one, i.e. an average behavior of a system is obtained by allowing a system to evolve numerically for a sufficiently long time and then performing averaging over all time steps. Time average of $A(\mathbf{r}^N,\mathbf{p}^N)$ in molecular dynamics simulations is defined as

$$\langle A\rangle_{time} = \lim_{\tau\to\infty} \frac{1}{\tau}\int_0^\tau dt A(\mathbf{r}^N(t),\mathbf{p}^N(t)) = \frac{1}{N_T}\sum_{t=1}^{N_T} A(\mathbf{r}^N,\mathbf{p}^N), \tag{2.49}$$

where N_T is the total number of timesteps. The *ergodic hypothesis* states that for a large class of systems, i.e. *ergodic systems*, the ensemble average is equal to the time average

$$\langle A\rangle_{time} = \langle A\rangle_{ensemble}. \tag{2.50}$$

This tell us that the ergodic system is independent on the initial condition, i.e if the system evolves in time infinitely long, it forgets its initial state, and samples the whole phase space. Equation (2.50) states that average of function $A(\mathbf{r}^N,\mathbf{p}^N)$ can be obtained either by averaging over all possible states, which is essentially Monte-Carlo approach, or by time averaging procedure, which is the approach used in molecular dynamics simulations.

2.3.3 Thermostats

Troughout this thesis the NVT, or canonical ensemble, which preserves number of particles N, volume V and temperature T, is used. In such simulations it is important to control the target temperature. For a classical many-body system in thermal equilibrium temperature is introduced via the equipartition theorem, which relates temperature with average kinetic energy per degree of freedom $k_B T = m\langle v_\nu^2 \rangle$, where m is particle mass, v_ν is its velocity component and k_B is Boltzmann constant. An instantaneous temperature $T(t)$, hence, can be written as

$$k_B T(t) = \sum_{i=1}^{N} \frac{m\mathbf{v}_i^2(t)}{N_f}, \qquad (2.51)$$

where N_f is the number of degrees of freedom. It might seem straightforward to keep temperature constant by performing velocity rescaling at each time step of molecular dynamics with a factor of $(T/T(t))^{\frac{1}{2}}$, where $T(t)$ is temperature at a time t. However, in this case the total kinetic energy does not fluctuate, as it does in a real constant-temperature ensemble. Another way to introduce temperature into consideration, is to keep a system in contact with an imaginary heat bath, *a thermostat*. Below we briefly discuss the two most common approaches, i.e. Andersen [30] and Nose [31] thermostats, which are employed in Paper III and II, respectively.

In Andersen approach, the heat reservoir controls the constant temperature of a system by implying stochastic forces on random particles and assigning them new momenta randomly extracted from the Maxwell-Boltzmann distribution. The coupling strength between the system and heat reservoir is defined by the frequency of stochastic collisions ν. As the two successive collisions are uncorrelated, the probability of the collision with thermostat is given by Poisson distribution $\mathscr{P}(\nu,t) = \nu e^{-\nu t}$. Between these two consecutive collisions the system evolves according to classical equation of motion (2.44). Taken together, the randomness of stochastic forces and classical dynamics of the system turn molecular dynamics into a Markov process [29]. Running a simulation for a sufficiently long time will ensure that all possible quantum states are visited, and a canonical ensemble is generated. Andersen thermostat typically gives good results for static properties, however, time-dependent properties, such as diffusion rate (or any other transport properties), which is solely defined by velocity autocorrelation function, are not possible to determine within this approach. This is due to randomness of the stochastic forces which make two subsequent velocities of a point particle completely uncorrelated in time and does not allow realistic description of kinetic properties.

Energy fluctuations can be also induced by the Nose thermostat, which is another way for isothermal molecular dynamic simulations. This method is based on introduction of additional degrees of freedom associated with the heat bath. Such fictitious coordinates and velocities enter a new, so-called *extended* Lagrangian formulation, which considers a system of many particles and a heat reservoir as a whole. The full Hamiltonian of the coupled system takes the form

$$\mathscr{H} = \mathscr{H}_{system} + \mathscr{H}_{heatbath} = \sum_{i}^{N} \frac{p_i^2}{2m_i s^2} + U(\mathbf{r}) + \frac{p_s^2}{2Q} + L\frac{lns}{k_B T}, \tag{2.52}$$

where s is the coordinate corresponding to a heat bath, p_s its conjugate momenta, Q is an effective mass associated to s and determines the energy exchange rate of a system with the heat bath. Integrating out these additional degrees of freedom, the canonical ensemble for the initial system characterized by temperature T can be obtained.

2.4 Ab initio lattice dynamics

Atomic vibrations in solids are responsible for many phenomena, including specific heat of crystals, thermal conductivity, thermal expansion, phase transitions, melting etc. In periodic solids the vibrations are described not in terms of vibrations of individual atoms, but in terms of collective excitations, corresponding to a coherent motion of all the atoms in the solid. A *phonon* is a quanta of these collective excitations, which is characterized by frequency ω, wave vector $\mathbf{q}$ and a certain polarization s. There is a number of semi-empirical models to calculate phonon dispersion relations, $\omega_s(\mathbf{q})$, based on parameters fitted to experimentally determined elastic constants, phonon frequencies and electric polarizabilities. These include Born-van Kármán model, shell model, valence force field method [32, 33, 34] and others. However, the accuracy of such semi-empirical methods is limited to the conditions at which the experimental parameters are fitted. *Ab initio* phonon dispersion relations can be calculated in the framework of Born-Oppenheimer approximation and density functional theory. The theory of lattice vibrations and its description from the electronic structure theory is the subject of this section.

2.4.1 Harmonic lattice

The behavior of a system of interacting n electrons and N nuclei is governed by the time-dependent Schrödinger equation

$$i\hbar\frac{\partial\Phi(\mathbf{r},\mathbf{R};t)}{\partial t} = \left(-\frac{\hbar^2}{2m}\sum_i \frac{\partial^2}{\partial \mathbf{r}_i^2} - \sum_I \frac{\hbar^2}{2M_I}\frac{\partial^2}{\partial \mathbf{R}_I^2} + V(\mathbf{r},\mathbf{R};t)\right)\Phi(\mathbf{r},\mathbf{R};t), \tag{2.53}$$

where $\mathbf{r} = (\mathbf{r}_1,..,\mathbf{r}_n)$, $\mathbf{R} = (\mathbf{R}_1,..,\mathbf{R}_N)$ refer to electronic and nuclear positions, m and M_I are their corresponding masses, and $V(\mathbf{r},\mathbf{R};t)$ describes electrostatic interactions

$$V(\mathbf{r},\mathbf{R};t) = \frac{1}{2}\sum_{i\neq j}\frac{e^2}{|\mathbf{r}_i - \mathbf{r}_j|} - \sum_{i,I}\frac{Z_I e^2}{|\mathbf{r}_i - \mathbf{R}_I|} + \frac{1}{2}\sum_{I\neq J}\frac{Z_I Z_J e^2}{|\mathbf{R}_I - \mathbf{R}_J|}.$$

As already discussed, adiabatic approximation allows to decouple the vibrational and electronic degrees of freedom as

$$\Phi(\mathbf{r},\mathbf{R};t) = \phi(\mathbf{R})\psi(\mathbf{r}|\mathbf{R})e^{\frac{-i\mathscr{E}t}{\hbar}}, \tag{2.54}$$

and hence it is possible to split the problem into an electronic problem upon fixed nuclear positions

$$\left(-\frac{\hbar^2}{2m}\sum_i \frac{\partial^2}{\partial \mathbf{r}_i^2} + V(\mathbf{r},\mathbf{R})\right)\psi(\mathbf{r}|\mathbf{R}) = E(\mathbf{R})\psi(\mathbf{r}|\mathbf{R}) \tag{2.55}$$

and a nuclear problem for an effective interatomic potential defined by the electrons

$$\left(-\sum_I \frac{\hbar^2}{2M_I}\frac{\partial^2}{\partial \mathbf{R}_I^2} + E(\mathbf{R})\right)\phi(\mathbf{R}) = \mathscr{E}\phi(\mathbf{R}). \tag{2.56}$$

Here $E(\mathbf{R})$ determines the *(Born-Oppenheimer) potential energy surface*. At the equilibrium nuclear configuration forces acting on each nuclei vanish

$$\mathbf{F}_I = -\frac{\partial E(\mathbf{R})}{\partial \mathbf{R}_I} = 0. \tag{2.57}$$

In the *harmonic* approximation the effective interatomic potential energy $E(\mathbf{R})$ is expanded in Taylor series up to the second order term. The resulting Hamiltonian can be transformed into a sum of independent harmonic oscillators. Further, vibrational frequencies $\omega(\mathbf{q})$ of normal modes and displacements $u_s^\alpha(\mathbf{q})$ are determined by solutions of the secular equation

$$\left(D_{IJ}^{\alpha\beta}(\mathbf{q}) - M_s\omega^2(\mathbf{q})\delta_{st}\delta_{\alpha\beta}\right)u_t^\beta(\mathbf{q}) = 0 \tag{2.58}$$

where and $D_{IJ}^{\alpha\beta}(\mathbf{q})$ is the Fourier transform of the matrix of interatomic force constants (IFC), i.e. the second order derivatives of the Born-Oppenheimer energy with respect to the nuclei positions

$$C_{IJ}^{\alpha\beta} = \frac{\partial^2 E(\mathbf{R})}{\partial \mathbf{R}_I^\alpha \partial \mathbf{R}_J^\beta}, \tag{2.59}$$

where α (β) are the Cartesian components of nuclear positions $\mathbf{R}_I$ ($\mathbf{R}_J$). Hence, the squared phonon frequencies, $\omega(\mathbf{q},s)^2$, are the eigenvalues of the $3N \times 3N$ dynamical matrix

$$D_{IJ}^{\alpha\beta} = \frac{1}{\sqrt{M_s M_t}}\sum_{\mathbf{R}} C_{IJ}^{\alpha\beta}(\mathbf{R})e^{-i\mathbf{q}\cdot\mathbf{R}}. \tag{2.60}$$

The second-order derivatives of the Born-Oppenheimer energy can be calculated using the Hellman-Feynman theorem, which leads to

$$\frac{\partial^2 E(\mathbf{R})}{\partial \mathbf{R}_I \partial \mathbf{R}_J} = -\frac{\partial \mathbf{F}_I}{\partial \mathbf{R}_J} = \int \frac{\partial n_{\mathbf{R}}(\mathbf{r})}{\partial \mathbf{R}_I} \frac{\partial V_{\mathbf{R}}(\mathbf{r})}{\partial \mathbf{R}_J} d\mathbf{r} \tag{2.61}$$

$$+ \int n_{\mathbf{R}}(\mathbf{r}) \frac{\partial^2 V_{\mathbf{R}}(\mathbf{r})}{\partial \mathbf{R}_I \partial \mathbf{R}_J} d\mathbf{r} + \frac{\partial^2 E_N(\mathbf{R})}{\partial \mathbf{R}_I \partial \mathbf{R}_J}, \tag{2.62}$$

where $V_{\mathbf{R}}(\mathbf{r})$ is the electron-nucleus interaction

$$V_{\mathbf{R}}(\mathbf{r}) = -\sum_{iI} \frac{Z_I e^2}{|\mathbf{r}_i - \mathbf{R}_I|}, \tag{2.63}$$

and $E_N(\mathbf{R})$ is the electrostatic interaction between nuclei

$$E_N(\mathbf{R}) = \frac{1}{2} \sum_{I \neq J} \frac{Z_I Z_J e^2}{|\mathbf{R}_I - \mathbf{R}_J|}. \tag{2.64}$$

Hence, to obtain the Hessian of the Born-Oppenheimer energy the knowledge of the charge density, $n_{\mathbf{R}}(\mathbf{r})$, and its *linear response* to a distortion of the nuclear configuration, $\partial n_{\mathbf{R}}(\mathbf{r})/\partial \mathbf{R}_I$, are required [35]. Further, we can Fourier transform the interatomic force constants $C(\mathbf{R})$ to find the dynamical matrices $D(\mathbf{q})$, which are then diagonalized in order to obtain the phonon frequencies at $\mathbf{q}$.

An alternative way to calculate phonon dispersion relations $\omega_s(\mathbf{q})$ is so-called *frozen phonon* approach. The perturbation of finite amplitude is frozen in the system, which is modelled by a supercell having $\mathbf{q}$ as a reciprocal lattice vector. Within the frozen phonon approach, phonon frequencies are calculated directly from the forces produced by finite atomic displacements. This method is rather straightforward to implement, however, the major drawback of this approach is that it is limited to supercells for which $\mathbf{q} = \mathbf{G}/n, n = 2, 3...$, where $\mathbf{G}$ is a reciprocal lattice vector, i.e. the supercell size should be commensurate with the wave vector of the perturbation $\mathbf{q}$. The linear response, instead, has the same vector $\mathbf{q}$ as the perturbation, and, therefore, does not involve any supercell into consideration. In this thesis, both the linear response and frozen phonon methods are employed, as implemented in Quantum ESPRESSO [36] and PHON [37] packages, respectively.

2.4.2 Beyond the harmonic approximation

One of the major shortcomings of the harmonic approximation is that it does not account for phonon-phonon interaction, i.e. does not predict evolution of phonon dispersion relation with temperature, and gives an infinite thermal conductivity and phonon lifetimes. The simplest extension of the harmonic approximation is the *quasi-harmonic* approximation (QHA), where the thermal properties of crystals are traced back to those of a system of non-interacting phonons, allowing the phonon frequencies to depend on volume or another constraint.

To account for *anharmonic* effects, i.e. phonon-phonon interaction, and obtain the evolution of the phonon spectra with temperature a so-called temperature-dependent effective potential (TDEP) method [38, 39] can be used (this is the method we employ in Paper II along with molecular dynamics simulations). The main idea behind TDEP is to find the best possible quadratic-form fit to the anharmonic potential energy surface of the system, obtained from Born-Oppenheimer molecular dynamics. The force constant matrices are determined by minimizing the difference between the forces from molecular dynamics simulations and those from the harmonic model. Unlike to quasi-harmonic approximation, using TDEP technique it is possible to obtain force constants that are both temperature and volume dependent. Thus, the method implicitly includes anharmonic effects and allows accurate finite temperature phonon and free energies calculations.

3. Phase stability

Depending on the external conditions, a system may interchange between various ground states (phases), i.e. undergo a *phase transition*. This phenomenon is known from our daily experience, for instance, condensation of water droplets and ice crystals in clouds. However, phase transitions are also important in many branches of science, ranging from the physics of the early universe to condensed matter physics. A short introduction to basic theoretical approaches to phase transitions is given below.

The ground states of a system can be distinguished regarding the fact that one or a number of specific physical quantities, so-called *order parameters*, are different in these states. Based on this observation, Landau formulated phenomenological theory in attempt to describe phase transitions [40]. The central idea behind this theory is to express the free energy of a system in the vicinity of the transition point as a power series of the order parameters. The general form of the Landau free energy, which can be considered as an approximation to Gibbs (or Helmholtz) free energy, is dictated by symmetry considerations. The ground state then corresponds to the minimum of the Landau free energy, that is a function of all internal degrees of freedom. Phenomenological Landau theory provides a simple way to determine many parameters that characterize a phase transition, such as the order of the transition and the critical exponents.

Collective lattice vibrations also give an information concerning the phase stability. The time dependence of the phonon amplitude is given by a factor $e^{-i\omega_s(\mathbf{q})t}$, where $\omega_s(\mathbf{q})$ is the phonon frequency. Having an imaginary frequency $\omega_s(\mathbf{q}) = i\Gamma$ as a solution of the secular equation, an exponential factor $e^{\Gamma t}$ diverges in time, corresponding to large atomic displacements from the ideal positions. The general stability criterion, therefore, can be written as $\omega_s(\mathbf{q})^2 > 0$. Hence, one of the precursors of structural phase transitions is anomalies (*softening*) in the phonon dispersion relations.

Here we address two distinct structural phase transitions in the metallic shape memory alloy AuZn and perovskite oxide $\mathrm{LiOsO_3}$ from first principles, and shortly summarize the major results of Papers I and II.

3.1 Stability of β and β' phases

Martensitic transitions are diffusionless, solid-to-solid phase transitions, characterized by collective atomic movements across distances typically shorter than nearest-neighbor spacings and have been observed in various metals, alloys, but also in ceramics and proteins [41, 1, 42]. Martensitic transformations have been also discovered in biological systems, such as the contractile deformation in the tail sheath of the T4 bacteriophague virus to invade its bacterial host [42, 43]. By definition, martensitic transitions are discontinuous, often driven by a shear-like mechanism and accompanied by spontaneous development of a rich microstructure on heat treatment, i.e. an intricate pattern, which is easily seen in optical micrographs [41]. The high-temperature phase, is referred to as the *austenite* phase, whereas the low-temperature phase with lower symmetry is known as the *martensite* phase [41, 1], in analogy with the corresponding phases in steel. There is a strict crystallographic relation between the parent (austenite) and the product (martensite) phases, and the resulting low-symmetry phase typically exhibits inhomogeneities such as slip, twinning and stacking faults. One of the main characteristics of a discontinuous martensitic phase transition is the presence of overheated and undercooled states that lead to a thermal hysteresis. Martensitic transitions can be irreversible, as observed in quenched steels (Fe-C), and reversible, as seen in *shape memory alloys* (e.g. AuZn, CuZn, CuAl) [41, 1].

Except of the shape memory effect, there is a plethora of phenomena associated with martensitic phase transitions, including rubber-like behavior, superelasticity, and two-way shape memory effects [44]. The very first shape-memory related phenomenon, i.e. a rubber-like behavior in AuCd alloy, was reported by Ölander in 1932 [45, 46]. Now it is known that rubber-like (pseudoelastic) behavior is found in aged martensites, while in just produced (unaged) martensites the deformation is plastic and they exhibit usual shape memory effect. Many other materials are known to exhibit the shape memory effect and by far not complete list include binary InTl, CrMn, CuMn, FePt, CoPt, PdTi, AgCd and ternary CuAlNi, CuZnAl, CuZnSi [47, 48, 44, 2] alloys. All these alloys undergo a crystallographically reversible, thermoelastic martensitic phase transition, with recoverable strain of typically 6-8 %. One of the first patented shape-memory devices was based on AuAgCd which was used for a thermally actuated electrical switch [44], however, the most industrially important discovery is the crystallographically reversible, thermoelastic martensitic transition in paramagnetic NiTi (NiTiNOL) by Buehler *et.al* [49] at the U.S. Naval Ordnance Laboratory. Nitinol is widely used in medicine as catheter for trapping "wandering" blood clots in cardiac blood vessels, in different thermomechanical and thermostatic devices, such as actuators for applications ranging from greenhouse windows to fire doors, as well as in aerospace industries, i.e. space antennas activated upon by solar heating [1, 2].

Among various martensitic structural transformations, those in β (disordered *bcc*) and β' (CsCl-type ordered) phase intermetallics are probably the most studied, and they serve as an excellent example of a connection between interatomic bonding, elastic constants and structural stability. Blackman diagram shown here for binary β'-phase alloys, also referred to as $B2$, makes the connection between lattice distortions and shear instabilities through the reduced Zener elastic constants c_{44}/c_{11} and c_{12}/c_{11}, where c_{11},c_{12} and c_{44} are three independent elastic constants for crystals with cubic symmetry (Figure 3.1) [50]. Plotting reduced elastic constants allows to eliminate elastic-stiffness differences and to emphasize the regions with the constant elastic anisotropy $A = 2c_{44}/(c_{11} - c_{12})$. Materials with similar interatomic bonding tend to cluster together in such a diagram. For instance, binary alloys with $B2$ symmetry predominantly assemble in a small region fulfilling a positive Cauchy condition ($c_{12} > c_{44}$), with the exception of FeTi and YZn, that fall along the Cauchy condition line ($c_{12} = c_{44}$) indicating the presence of central forces in these alloys. Departure from the Cauchy condition $c_{12} = c_{44}$ implies the presence of three-body, or angular forces. All selected $B2$ alloys exhibit a large elastic anisotropy, with the noble metal alloys like AuCd, AuZn, AuCuZn having the highest anisotropies ($8 < A < 12$). Empirically it is known that $B2$ alloys with $A > 4$ show lattice instabilities with respect to shear along [110] symmetry directions and exhibit large softening in phonon dispersion relations.

By considering *bcc* alloys with low $(110)[\bar{1}00]$ shear resistance, such as β-phases for which CuZn is the prototype, Zener suggested principal mechanisms of mechanical stability [51]. A common property of the β-brass alloys is high elastic anisotropy which is a result of an anomalously low value of Voigt elastic stiffness $c' = (c_{11} - c_{12})/2$, where c_{11} is referred to a shear across the (100) plane, while c' is related to the shear along the (110) plane in the $[\bar{1}00]$ direction. According to Zener, the extremely low values of c' in *bcc*-based structures can be interpreted in terms of lattice type and ionic interactions in the following way. In metals the shear resistance emanates primarily from two sources, i.e. the exchange interaction between the nearest neighboring ions, and the electrostatic interaction between ions and conduction electrons [51]. In *bcc*-based structures, the exchange interaction gives a positive contribution to c' when it is attractive, and negative contribution when it is repulsive. This is also the case for compounds with closed ionic shells. The interaction due electrostatic forces between electrons and ions contributes positively to c' independent of the underlying crystal structure. Therefore, a balance between these two interactions defines the mechanical stability in the *bcc* structures. The low values of Voigt stiffness c' correspond to high vibrational entropy, which stabilize the *bcc* structure at high temperatures [51]. In addition, softening of c' and c_{44} due to changes in temperature, composition or pressure can be also regarded as a precursor to a displacive structural transition [52].

It is known that atomic and ionic sizes (which also define clearence parameter), electronegativity, degree of order and electron per atom concentration e/a affect the stability of the β-phase alloys and corresponding phase diagram boundaries [53]. For instance, ternary Ag-Au-Cd alloy near the stoichiometric composition $AgAuCd_2$ exhibit a minimum in martensitic phase transition temperature T_c, which led to suggestion that ordering enhanced the stability of β-phases. However, in Au-Cu-Zn martensitic transition temperature exhibit a maximum close to $AuCuZn_2$ composition, while in AuZn T_c changes linearly with composition from Zn-depleted to Zn-rich region near the equiatomic range. Hence, ordering seems not to play a dominant role in developing an instability in β-phases. The effect of adding elements with different valencies (Cu, Ag, Mg, Cd, Ga, In, Si) has been also considered with respect to the ordered β'-phase of AuZn (CsCl-type) and it has been shown that the transition temperature in AuZn based β'-phase alloys varies in a random fashion regardless of the valence of the solute atoms [53]. Different behavior of T_c is observed for solutes even with the same valence, for instance, substituting Au by Ag with slightly larger atomic size, but the same valency, markedly decreases T_c, hence, providing a stabilization effect. In contrast, substitution with Cu with even smaller atomic radii produces no changes in the martensitic transition temperature [53]. Hence the formation of the martensite phase is not simply related to e/a ratio and there is a lack of correlation between electron per atom ratio and T_c. Similar trend has been also observed for alloys based on β-brass (CuZn) and other noble metal β-phase alloys [53, 54].

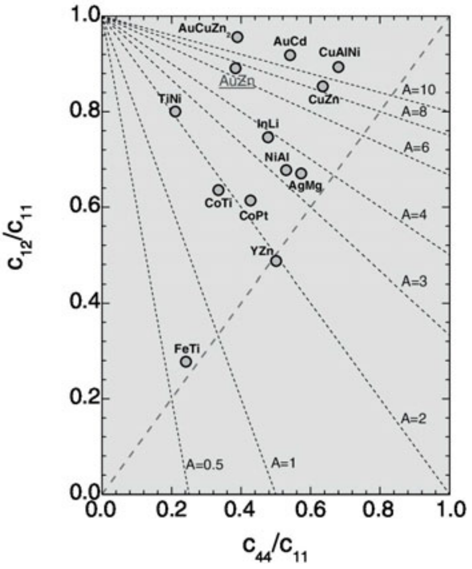

Figure 3.1. Blackman diagram for a range of binary and ternary alloys showing reduced elastic constants and Zener elastic anisotropies, A, plotted as dotted lines. Diagonal dashed line highlights the Cauchy condition $c_{12} = c_{44}$. Adapted from Ref. [50].

Despite the above-mentioned survey, not a great deal is known about the systems which undergo the diffusionless martensitic phase transition and at the same time exhibit the shape memory effect [55]. However, the metallic character of such materials suggests an important role of the electrons in the microscopic mechanism driving the phase transition. It is, therefore, instructive to address noble-metal based shape-memory AuZn. The low-temperature transition, i.e. $T_c = 45$ K in $\mathrm{Au_{0.52}Zn_{0.48}}$ and $T_c = 64$ K in $\mathrm{Au_{0.50}Zn_{0.50}}$ [56], is only accessible using cryogens, which makes AuZn less studied compared to other $B2$ intermetallics [55]. The shape memory effect in AuZn is associated with the reversible structural transformation from the high-temperature $B2$-phase (space group 221, Pm$\overline{3}$m, $\mathrm{O}_h{}^1$, Pearson symbol cP2) to the low-temperature trigonal phase related to the $B2$ phase by small displacements or shuffle [57, 50]. Interestingly, no variation of the resistivity associated with the martensitic phase transition has been reported for AuZn with equiatomic composition [53]. Presumably, this is due to perfect arrangements of the martensitic platelets and, as a result, low electron scattering [53]. The de Haas-van Alphen oscillations in magnetic susceptibility indicate a significant Fermi surface reconstruction associated with the martensitic phase transition in AuZn [55]. The coexistence of Fermi surfaces of the parent and product phases down to 60 mK implies an incomplete phase separation between the austenite and martensite [55], and hence, a first order *discontinuous* character of the structural transition. In fact, the order of phase transition in equiatomic AuZn is a matter of debates [55, 56, 58]. From the excess heat capacity measurements, a λ anomaly has been found at 45 K for off-stoichiometric $\mathrm{Au_{0.52}Zn_{0.48}}$ and at 64 K for $\mathrm{Au_{0.50}Zn_{0.50}}$ as well, however, no latent heat has been observed for the equiatomic composition [56]. Elastic neutron-scattering measurements of the satellike peak intensity along $Q = (1.33, 0.67, 0)$ at the corresponding martensitic transition temperatures show a rapid, almost a step change for $\mathrm{Au_{0.52}Zn_{0.48}}$, while a continuous variation has been observed for the equiatomic AuZn on heating at 64 K [56]. This indicates a *continuous* structural transformation in AuZn, which contradicts the established definition of the diffusionless martensitic transitions. Another supporting evidence of the second order phase transition in AuZn is the lack of thermal hysteresis from electrical-resistivity measurements [56]. The phonon softening with decreasing temperature has been also observed, and the inflection of the $\mathrm{TA_2}$ acoustic branch near $\mathbf{q} = \frac{1}{3}[1,1,0]$ manifests the low shear instability of the $B2$ phase [56, 57].

In light of these data, Paper I addresses from first principles the electronic and vibrational properties of $B2$ AuZn. We reproduce the experimentally observed instability of the transverse acoustic $\mathrm{TA_2}$ branch along the Γ-M [ξ,ξ,0] direction of the Brillouin zone and show that the softening is related to peculiarities in the electronic band structure, i.e. Fermi surface nesting and a peak in the bare Lindhard susceptibility. Landau phenomenological approach to phase transitions, that relies on the expression of the excess free energy in terms of symmetry invariants, is also applied in our study.

3.1.1 Structural transition in shape-memory AuZn

To proceed further with the analysis of the lattice dynamical properties of $B2$ AuZn, we calculate *ab initio* phonon dispersion relations by means of linear response (LR) [35] and direct force (or small displacement) (DF) [37] techniques with ultrasoft (US) pseudopotentials and projector augmented-wave (PAW) method, respectively. As we show below, the accurate description of lattice vibrations along the Γ-M [ξ,ξ,0] direction of the cubic Brillouin zone requires large cutoff energies, as well as consideration of a large number of coordination shells in the direct force method calculations. To ensure the convergence of all the parameters involved in the calculations, the phonon dispersion relations were examined with respect to the charge density cutoff for LR US, and the kinetic energy cutoffs for DF PAW methods (Figure 3.2). As seen from Figure 3.2(a),(c), employing both DF GGA and LR GGA with low cutoff energies seem to be inadequate, as it results in stable TA_2 mode along the Γ-M path. This is in contradiction with the experimentally observed mechanical instability of $B2$ AuZn below 64 K. However, an instability is developed near the wave vector $\mathbf{q} = \frac{1}{3}[1,1,0]$ together with persisting additional imaginary frequencies at around $\mathbf{q} = \frac{1}{6}[1,1,0]$ if the cutoff energy is increased (Figure 3.2(a),(c)-(d)). For the LR LDA calculations (Figure 3.2(d)), higher cutoff energies, instead, allow to pinpoint an instability only near $\mathbf{q} = \frac{1}{3}[1,1,0]$, so the phonon spectrum fully mimics the experimental one.

As mentioned above, the use of too low cutoff energy with GGA functional results in dynamically stable $B2$ AuZn phase ($\omega_M^{DF,GGA} = 0.750$ THz and $\omega_q^{DF,GGA} = 0.274$ THz) at $T = 0$ K, as density functional theory does not involve temperature into consideration (red curve in Figure 3.2(a)). Similar theoretical phonon dispersion relations of $B2$ AuZn calculated within the direct force technique have been previously reported for a 72-atom supercell [58]. We have therefore performed additional direct force GGA calculations for the lattice parameter (3.195 Å) and the cutoff energy (350 eV) used in Ref. [58], but using a larger 6×6×6 supercell containing in total 432 atoms. As a result, we obtained a soft TA_2 acoustic branch with imaginary frequency $\omega_q^{DF,GGA} = -0.197i$ THz, contrary to Ref. [58], where a positive $\omega_q^{DF,GGA} \sim 0.484i$ THz was found. Hence, we emphasize here that it is crucial to take into consideration a sufficient amount of coordination shells for a proper description of lattice dynamics in $B2$ AuZn.

The direct force phonon dispersion relations also show unusual behavior of the optical mode along the Γ-X direction with an abrupt jump in frequencies up to 5.63 THz (PAW LDA) and 6.02 THz (PAW GGA), as well as additional imaginary frequencies near the Γ point along Γ-M ($\omega^{DF,LDA} = -0.411i$, $\omega^{DF,GGA} = -0.382i$) and Γ-R ($\omega^{DF,LDA} = -0.112i$, $\omega^{DF,GGA} = -0.048i$) directions (Figure 3.2(c),(d)). This suggests a numerical instability associated with a small atomic displacement used for interatomic force calculations (0.038 Å), and to investigate this we performed additional DF calculations for

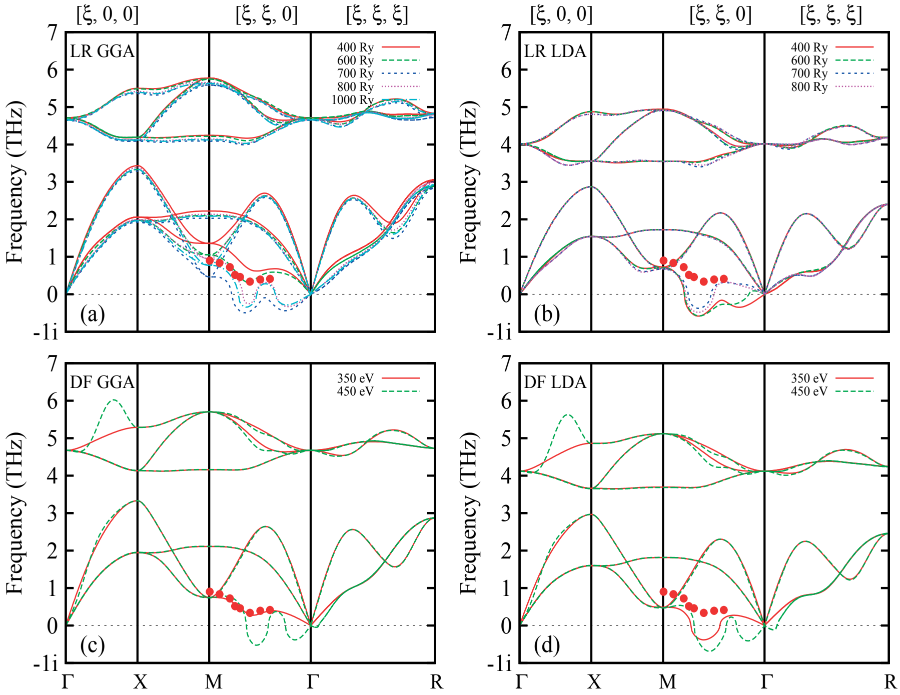

Figure 3.2. Phonon dispersion relations of *B*2 AuZn calculated using linear response (a), (b) and direct force methods (c),(d) with different cutoff energies. The direct force calculations have been performed using the amplitude of atomic displacement of 0.038 Å. The results of the linear response and direct force calculations are shown together with the experimental data (red circles) measured using inelastic X-ray scattering at $T = 200$ K [56].

a range of atomic displacements as shown in Figure 3.3. At smaller cutoff energies, the phonon dispersion relations are not affected by the change in atomic displacements in any way when the GGA functional is used (Figure 3.3(a)). However, for the LDA the smallest displacement results in a phonon softening near $\mathbf{q} = \frac{1}{3}[1,1,0]$, which is gradually stabilized by further increase of the magnitude of atomic displacements (Figure 3.3(b)). Similar trend in the dynamical stabilization of the TA$_2$ is observed at larger cutoff energies for plane waves (Figure 3.3(c),(d)). The kink in the optical mode along the Γ-M is absent for larger atomic displacements, so we can conclude that this is purely a numerical issue. The low energy acoustic TA$_2$ branch is very sensitive with respect to the amplitude of atomic displacement, hence, AuZn is highly anharmonic, i.e. the phonon frequencies are imaginary for small atomic displacements and positive real for larger displacements. Our theoretical results qualitatively agree with the experiment, such that it is possible to pick up the instability of the transversal TA$_2$ acoustic mode along the Γ-M direction and

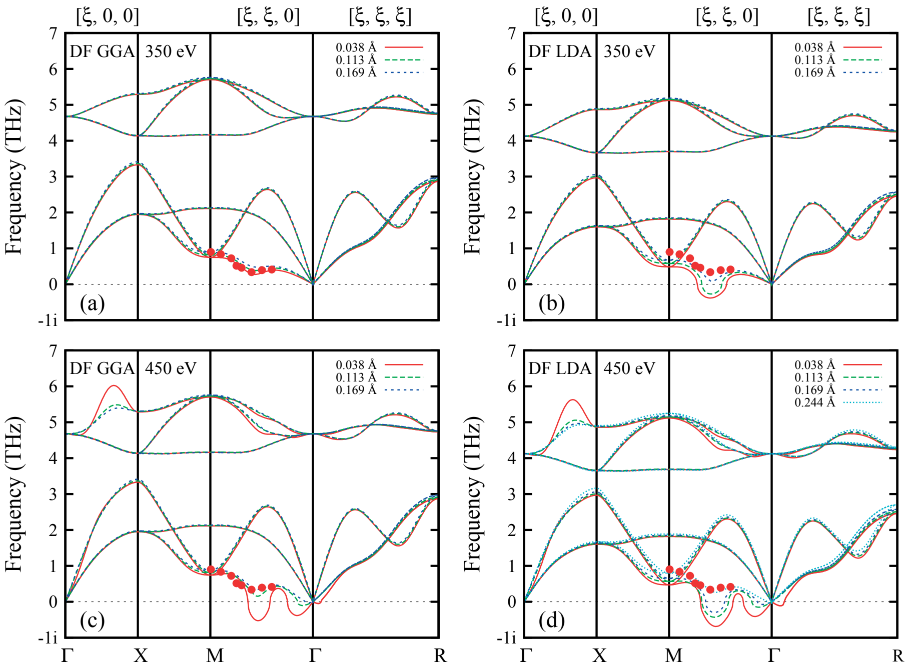

Figure 3.3. Direct force phonon dispersion relations of $B2$-AuZn calculated using different values of atomic displacement and cutoff energy. The results of the linear response and direct force calculations are shown together with the experimental data (red circles) measured using inelastic X-ray scattering at $T = 200$ K [56].

predict the instability of the cubic austenite $B2$ phase at low temperatures. Overall, we find linear response calculations being numerically more stable compared to the small displacement (direct force) method, which is strongly dependent on the magnitude of the atomic displacement used for interatomic force constants calculations. The anomalous phonon softening along [ξ,ξ,0] direction has been also observed in NiTi [59], NiAl [60, 61], AuCd [62], FePt [63] and other binary Hume-Rothery alloys with electron per atom concentration e/a=3:2.

The atomic vibrations are, in general, screened by electrons. However, as it has been pointed out by Kohn [64], in metals this screening might be significant for lattice vibrations associated with certain $\mathbf{q}$ of the Brillouin zone, determined by the shape of the Fermi surface. Kohn anomalies may occur only if there are electronic states $\mathbf{k_n}$ and $\mathbf{k_m}$, such that $\mathbf{k_m} = \mathbf{k_n} + \mathbf{q}$, i.e. there is Fermi surface *nesting*. Hence, we address the topology of the Fermi surface to connect with the peculiarities in the phonon dispersion relations (Figure 3.4). The Fermi surface does not reveal any complex topology and consists of a hole sheet that is centered at the Γ point (green) and small, almost flat electron pockets (blue) located close to the R points of the Brillouin zone,

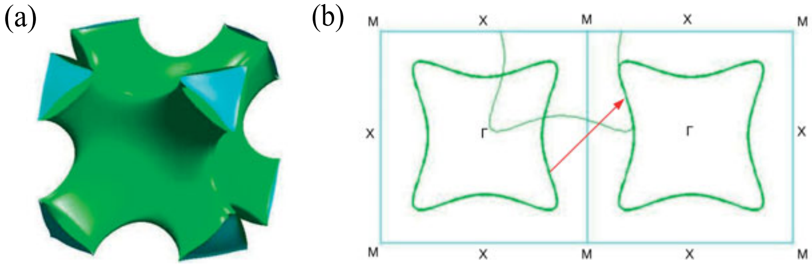

Figure 3.4. (a) Theoretical Fermi surface of $B2$ AuZn at $T = 0$ K. Electron (hole) pockets are shown in blue (green). (b) A cut through the Fermi surface along (001) plane together with the nesting vector (red arrow) $\mathbf{q} = \frac{1}{3}[1,1,0]$.

which show up in de Haas-van Alphen oscillations [55]. Figure 3.4(b) shows a cut through the Fermi surface in the $\mathbf{k_x k_y}$ plane together with the nesting regions and the nesting vector $\mathbf{q} = \frac{1}{3}[1,1,0]$. The nesting vector matches that of the strongly softened acoustic transversal phonon TA$_2$, supporting the connection between the Kohn anomaly and Fermi surface nesting in $B2$ AuZn. The Fermi surface of AuZn resembles one for Ni-Al, an another $e/a = 3:2$ Hume-Rothery electron compound, calculated from first principles [65] and also measured by Compton scattering [66]. In connection to the Fermi surface nesting we have also calculated bare susceptibility function via the Lindhard formula (for details see Paper I). The theoretical bare susceptibility exhibits a quite pronounced peak along [ξ,ξ,0] direction of the cubic Brillouin zone close to $\mathbf{q} = \frac{1}{3}[1,1,0]$. The electron-phonon matrix elements, which are not considered here, are also expected to enhance the strength of the peak even further.

The effect of pressure on the phase stability of the $B2$ AuZn has been also addressed in Paper I. The experimental lattice parameter (3.13 Å) used in our linear response phonon spectra calculations results in a hydrostatic pressure of $P_{LDA} = -5.3$ GPa in US LDA, and $P_{GGA} = 8.0$ GPa in US GGA calculations. If there was a perfect agreement between theory and experiment, the calculated pressure should have been 0 GPa, and the deviation from 0 GPa manifests a slight overbinding of the LDA ($a_{US}^{LDA} = 3.09$ Å) and underbinding of the GGA ($a_{US}^{GGA} = 3.19$ Å) functionals. The phonon spectra calculated at the equilibrium volumes for each of the functionals, also exhibit imaginary frequencies at $\mathbf{q} = \frac{1}{3}[1,1,0]$, such that $\omega_q^{LR,LDA} = -0.392i$ THz for US LDA and $\omega_q^{LR,GGA} = -0.363i$ THz for US GGA, which reflects an instability of the TA$_2$ mode along the Γ-M [ξ,ξ,0] direction and is consistent with the experiment. The evolution of the phonon frequency of the TA$_2$ acoustic branch at $\mathbf{q} = \frac{1}{3}[1,1,0]$ with pressure is collected in Table 3.1. The TA$_2$ mode hardens with pressure stabilizing the cubic $B2$ phase of AuZn at theoretical

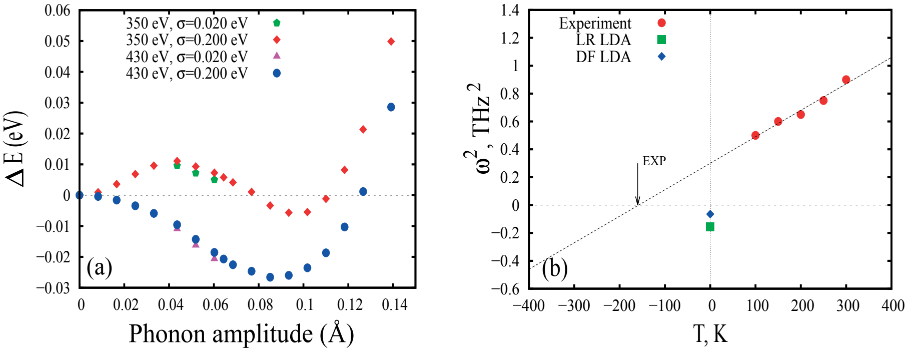

Figure 3.5. (left) The excess (frozen phonon) energy as a function of frozen phonon amplitude calculated with respect to the ideal $B2$ phase. The calculations have been performed using PAW potentials together with a LDA functional and a $4\times4\times4$ k-point mesh. Energies shown in the figure correspond to the energy per cell containing 432 atoms. (right) Square frequencies ω^2 at the wave vector $\mathbf{q} = \frac{1}{3}[1,0,0]$ as a function of temperature T. Here, σ is the band smearing. Measurements (red circles) are performed using inelastic X-ray scattering [67].

pressure of 11.2 GPa for US GGA and at 11.5 GPa for US LDA, respectively. The pressure dependence of the phase transition temperature measured by ac transport where $B2$ phase stabilizes under pressure ≈ 3 GPa [56], confirms our findings. Due to the unknown form of the exact exchange-interaction, as well as the effect of spin-orbit coupling which might be important in $B2$ AuZn, but not considered here, the theoretical equations of state do not exhibit minimum at the experimental lattice parameter (3.13 Å). As a result, we can not directly compare the experimental and theoretical pressures which stabilize the high temperature $B2$ phase. By assuming that theoretical $p(V)$ curves are the same as the experimental one, we can, in principle, recalculate an experimental volume compression at 3 GPa from the theoretical equation of states. We obtain the experimental volume compression $\Delta V/V_{US}^{GGA} = 0.027$ and $\Delta V/V_{US}^{LDA} = 0.018$ from the US GGA and US LDA curves, respectively. As represented in Table 3.1, the TA_2 hardens within the pressure range of 8.0-11.2 GPa for US GGA approach, and within 5.5-11.5 GPa for US LDA, so we calculate theoretical volume compressions corresponding to these pressure ranges and obtain $\Delta V/V_{US}^{LDA} = 0.019$ and $\Delta V/V_{US}^{GGA} = 0.029$, which are in favorable agreement with the experimental volume compressions, recalculated from our theoretical data. We have therefore shown that the high temperature $B2$ phase of AuZn can be stabilized by pressure at low temperatures, condensing in the global ground state. Persisting softening of the low-energy acoustic TA_2 branch near $\mathbf{q} = \frac{1}{3}[1,1,0]$ is presumably due to a strong electron-phonon coupling, and, in principle, can give rise to superconductivity at low temperatures.

Table 3.1. *Evolution of the frequency of* TA_2 *mode* ω *at* $\mathbf{q} = \frac{1}{3}[1,1,0]$ *with pressure P. For each pressure we also show corresponding lattice parameter a, volume compression* $\Delta V/V$*, where V is theoretical equilibrium volume. The calculations are performed within the linear response method.*

Functional	a, Å	P, GPa	ΔV/V	ω, THz
GGA	3.163	3.4	0.028	-0.464i
	3.130	8.0	0.058	-0.329i
	3.110	11.2	0.076	0.269
	3.050	23.0	0.128	0.733
LDA	3.130	-5.3	-0.036	-0.483i
	3.060	5.5	0.032	-0.299i
	3.030	11.5	0.060	0.180
	2.980	23.8	0.106	0.517

Further, we studied the structural phase transition in $B2$ AuZn by means of phenomenological Landau theory. According to Landau theory of a phase transitions the excess energy of a system, undergoing phase transition can be expanded in Taylor series of the order parameter in the vicinity of the critical temperature T_c [40]. Similar to earlier studies on the martensitic phase transition in AuCd [68], the magnitude of atomic displacement which corresponds to the excitation of the transversal acoustic TA_2 mode is chosen here as the primary order parameter driving the martensitic phase transition to the low temperature phase. We have therefore calculated the energy of a frozen TA_2 mode with the eigenvector $\mathbf{q} = \frac{1}{3}[1,1,0]$, which is the excess energy in this consideration (Figure 3.5(a)). As in the case of phonon spectra calculations discussed above, the Landau potential is very sensitive with respect to the choice of the cutoff energy. Smaller values of the cutoff give rise to a positive curvature of the excess energy ΔE at zero phonon amplitudes, which indicates a stable TA_2 phonon mode at $\mathbf{q} = \frac{1}{3}[1,1,0]$ and overall $B2$ phase stability, which disagrees with the imaginary TA_2 phonon mode along Γ-M [ξ,ξ,0] direction. However, the Landau potential profile is drastically changed if the value of the cutoff energy is increased up to 430 eV (Figure 3.5(a)). The curvature of the potential becomes negative and reflects a shear instability of the $B2$ phase at low temperatures, and is consistent with vibrational spectra shown in Figures 3.2 and 3.3 for converged cutoff energies. We should also mention here, that no dependence of the potential with respect to the band smearing (σ) has been found (Figure 3.5).

The evolution of the excess energy with temperature defines the order of the phase transition. However, as the excess energy calculations are performed within the density functional theory at $T = 0$ K and do not allow any consideration of thermal effects, it is difficult to draw any conclusion on the order of the phase transition, hence, we refer to the experimental data. Figure 3.5(b) shows squared phonon frequencies at the wave vector $\mathbf{q} = \frac{1}{3}[1,1,0]$ measured by means of inelastic X-ray scattering for a set of temperatures [67]. According to Cochran [69], who introduced the notions of "soft mode theory" and "mode softening" with respect to (second order) phase transitions, the $\omega_{\mathbf{q}}^2$ versus temperature is expected to be linear and may provide an estimate for a transition temperature by extrapolating $\omega_{\mathbf{q}}^2(T)$ down to $\omega_{\mathbf{q}}^2(T) = 0$. In our case such extrapolation leads to unrealistic negative phase transition temperature $T_c \approx -150$ K (Figure 3.5(b)). This can be explained if the phase transition is of first order, characterized by an abrupt change of the order parameter, i.e. phonon frequency $\omega_{\mathbf{q}}$ or phonon amplitude, from zero to a non-zero value at the transition point. In the soft mode theory, the frequencies of the mode which drives the phase transition can be approximated as $\omega_{\mathbf{q}}^2(T) \approx a(T - T_c)$, however, such assumption does not hold for $B2$ AuZn. Hence, the structural transition in $B2$ AuZn is of the first order, which is also manifested by the observation of the coexistence of the Fermi surfaces down to 60 mK, i.e. an incomplete austenite to martensite phase transformation [55].

Based on this analysis, we conclude that AuZn is highly anharmonic and requires a very accurate treatment of lattice dynamical properties, especially when studied with the small displacement method. In our study we address the topology of the Fermi surface and show that Fermi surface nesting along $\mathbf{q} = \frac{1}{3}[1,1,0]$ and peak in the bare susceptibility function are coupled to the phonon softening along the Γ-M direction of the cubic Brillouin zone. Hence, we suggest that electron-phonon coupling is likely to be the operative mechanism driving the martensitic phase transition in AuZn. From the experimental $\omega_{\mathbf{q}}^2(T)$ dependence we suggest that the phase transition in AuZn is of the first order. Finally, pressure-induced structural stabilization of $B2$ AuZn at low temperatures in a superconducting state due to strong electron-phonon coupling has been also considered.

3.2 Ferroelectric-like transition in the metallic state

Ferroelectric phase transitions are designated by appearance of a spontaneous electric polarization. Metals are not expected to exhibit ferroelectricity, as the conduction electrons screen the static internal electric fields, and as a result, ferroelectric distortions are forbidden. However, the concept of "ferroelectric metal", which undergoes a ferroelectric-like structural transition, was introduced by Anderson and Blount already in 1965 [6]. It was proposed that such phase transition must be (i) continuous, (ii) accompanied by the appearance of the polar axis in the low-temperature structure, and lastly, (iii) an inversion center should disappear in the low-temperature phase, which therefore is always non-centrosymmetric. Anderson and Blount also suggested that "ferroelectricity" in the metallic state is possible if the coupling between the conduction electrons and the soft ferroelectric phonon mode is weak [6]. Over the last decades several systems have been considered as possible candidates to exhibit metallic "ferroelectricity", including A-15 (or β-W) superconductors V_3Si and Nb_3Sn [6], pyrochlore $Cd_2Re_2O_7$ [70, 71], and electron-doped $BaTiO_{3-\delta}$ [72]. However, the phase transitions in superconducting V_3Si and Nb_3Sn have been later shown to be either weakly first order or electronically driven [73, 74]. Further studies have also revealed that in oxygen-deficient $BaTiO_{3-\delta}$ ferroelectric ordering and the metallic conduction state correspond to two distinct phases [75]. Finally, structural phase transition in cadmium pyrochlore $Cd_2Re_2O_7$ was concluded to be better described as a "piezoelectric", and a unique polar axis, associated with the phase transition, was not identified [70].

However, recent experimental studies have reported on a continuous phase transition in the metallic $LiOsO_3$ ($T_c = 140$ K) [7], which is structurally equivalent to the ferroelectric transition in $LiNbO_3$ ($T_c = 1430$ K) [76]. The phase transition in the perovskite oxide $LiOsO_3$ is also characterized by a reduction of symmetry (from $R\overline{3}c$ to $R3c$) and the loss of inversion center. This makes $LiOsO_3$ a first, and so far, a sole realization of Anderson and Blount idea, who were first to point out such a possibility [6]. According to the experimental findings, the residual resistivity in $LiOsO_3$ is more than an order of magnitude larger than a typical value for a normal metal, suggesting a substantial defect and domain scattering [7]. Experimental observations also show that there is no magnetic ordering and no significant electronic correlations, hence the transition is unlikely to be driven by any collective electron dynamics. In addition, octahedrally coordinated Os ion is not Jahn-Teller active, therefore, the ferroelectric-like transition in $LiOsO_3$ is not due to Jahn-Teller distortions [7]. Structural data refined from the neutron diffraction experiments indicates that the transition is likely driven by a collective shift in the mean Li positions by almost 0.5 Å [7] by either order-disorder or displacive mechanism. This leaves room for discussion regarding the nature of the phase transition $LiOsO_3$ and the role of collective lattice vibrations in this process.

There have been several theoretical studies attempting to explain the nature of ferroelectric-like distortions in metallic $LiOsO_3$. Lattice dynamical properties of the high-temperature $R\overline{3}c$ structure have been analyzed within first principles density functional theory [77]. The softening of the optical mode, associated with the structural phase transition, have been attributed to Li displacements. This is in line with the neutron diffraction experiments which found large anisotropy in the Li displacements along the c-axis [7]. Comparison of the Fermi surfaces of the $R\overline{3}c$ and $R3c$ structures did not reveal any significant differences in their topology, thus, it was argued that the phase transition is not electronically driven [77]. From orbital-resolved density of states it was shown that e_g orbitals of Os, which are nearly empty, hybridize with p orbitals of oxygen and contribute to the formation of ferroelectric distortions, which is similar to a mechanism in ferroelectric pervoskite oxides [78]. At the same time, nearly half-filled t_{2g} bands are responsible for metallicity. It has been also argued that spin-orbit coupling enhances stability of the metallic state of $LiOsO_3$ [78]. Metallic perovskite oxide $LiOsO_3$ has also been shown to possess an inhomogeneous charge distribution which results in highly anisotropic screening, and allows local dipole-dipole interactions [79]. However, these interactions are not completely screened along certain directions, which leads to ferroelectric-like ordering below the phase transition temperature. From the potential energy surface calculations it has been argued that the phase transition in $LiOsO_3$ is of order-disorder type. A tolerance factor, t_R, for ABO_3 hexagonal perovskites has been introduced in Ref. [80]. This factor relates distances between A-ion and its first and second nearest O atoms, to describe the instability in $R\overline{3}c$-type structures with respect to A-ion off-centering. Using the tolerance factor it has been shown that ferroelectric-like distortions in $LiOsO_3$ are due to the instability of Li atoms. This is in contrast to phase transition in $LiNbO_3$ where Nb, a B-ion is Jahn-Teller active and plays a significant role in the phase transition. Recent electronic structure analysis of $LiOsO_3$ with dynamical mean-field theory have also suggested that $LiOsO_3$ is close to Mott transition [81].

In this section we investigate structural and lattice dynamical properties of $LiOsO_3$ at finite temperatures which have not been addressed so far. For this purpose we employ molecular dynamics simulations, as well as recently developed temperature-dependent effective potential method [38, 39].

3.2.1 Understanding the phase transition in $LiOsO_3$

Both the high-temperature $R\overline{3}c$ and the low-temperature $R3c$ structures of $LiOsO_3$ have been fully optimized using generalized gradient (PBE) and local density (LDA) approximations for the exchange-correlation effects. The results are collected in Tables 3.2, 3.3 along with the experimental data. The relaxed internal positions of ions are in a good agreement with those obtained from the neutron diffraction experiments [7], whereas theoretical unit cell volumes are slightly underestimated (overestimated) for the LDA (PBE) calculations. It is also worth to notice an extremely small difference in the ground state volumes of the high-temperature and the low-temperature phases, i.e. $\Delta V_{exp} = 1.5$ Å^3 (0.5%), $\Delta V_{LDA} = 3.1$ Å^3 (1%) and $\Delta V_{PBE} = 1.95$ Å^3 (0.6%). As the volume difference between the two phases is better captured by PBE, we use this functional in all our further calculations.

Table 3.2. *Structural parameters of high-temperature phase (HT) $R\bar{3}c$ of $LiOsO_3$ from first-principles calculations. For local density approximation (LDA) a=5.063 Å, c=12.908 Å, V=286.51 Å; for generalized gradient approximation (PBE) a=5.146 Å, c=13.222 Å, V=303.21 Å^3. Experimental data refined at 300 K: a^{HT}_{exp}=5.064 Å, c^{HT}_{exp}=13.211 Å, V^{HT}_{exp}= 293.37 Å^3 (Ref. [7]).*

Atom	Wyckoff symbol	x	y	z
Li (PBE)	6a	0	0	0.25
Os	6b	0	0	0
O	18e	0.6274	0	0.25
Li (LDA)	6a	0	0	0.25
Os	6b	0	0	0
O	18e	0.6309	0	0.25
Li (exp)	6a	0	0	0.25
Os	6b	0	0	0
O	18e	0.6298(2)	0	0.25

Table 3.3. *Structural parameters of low-temperature phase (LT) $R3c$ of $LiOsO_3$ from first-principles calculations. For local density approximation (LDA) a=4.986 Å, c=13.166 Å, V=283.41 Å^3, for generalized gradient approximation (PBE) a=5.098 Å, c=13.384 Å, V=301.26 Å^3. Experimental data refined at 10 K: a^{LT}_{exp}=5.046 Å, c^{LT}_{exp}=13.239 Å, V^{LT}_{exp}=291.88 Å^3 (Ref. [7])*

Atom	Wyckoff symbol	x	y	z
Li (PBE)	6a	0	0	0.2173
Os	6a	0	0	-0.00044
O	18b	0.6288	-0.0030	0.2518
Li (LDA)	6a	0	0	0.2128
Os	6a	0	0	0.0004
O	18b	0.6339	-0.0037	0.2530
Li (exp)	6a	0	0	0.2147(6)
Os	6a	0	0	0
O	18b	0.6260(5)	-0.0102(9)	0.2525(6)

Previously calculated phonon dispersion relations of the $R\bar{3}c$ phase reveals an imaginary optical mode along all high-symmetry directions of the Brillouin zone [77]. This indicates dynamical instability of the centrosymmetric phase and that there is an infinite number of possible atomic distortions, which could stabilize the $R\overline{3}c$ structure at low temperatures. To further investigate the possibility of stabilization of the ferroelectric-like soft phonon mode at enhanced temperatures, we performed phonon spectra calculations using temperature dependent effective potential (TDEP) method [38, 39].

Phonon dispersion relations calculated for the high-temperature centrosymmetric $R\overline{3}c$ phase at 300 K and the low-temperature non-centrosymmetric $R3c$ phase at 100 K are shown in Figures 3.6 and 3.7 together with the corresponding phonon densities of state. Here, we also avoid showing the evolution of the phonon spectra with temperature for each of the phases for the reasons which will become clear later. Phonon spectra of the $R\overline{3}c$ phase at $T = 300$ K, i.e. where the experimental structure is both dynamically and thermodynamically stable, does not exhibit any softening, in contrast to $T = 0$ K calculations (see Fig.5 in Paper II). Therefore, the high-temperature phase is dynamically stabilized at finite temperatures by anharmonic effects. The low-temperature $R3c$ is also dynamically stable below the phase transition temperature (Figire 3.7).

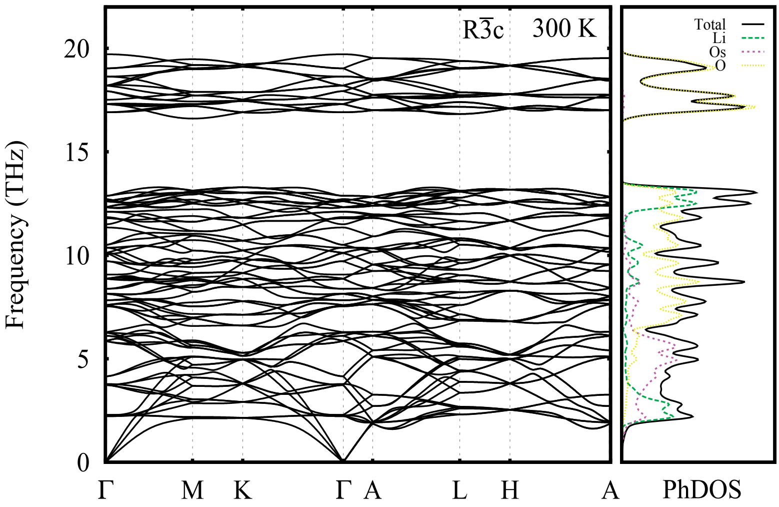

Figure 3.6. Phonon spectra of the high-temperature phase ($R\overline{3}c$) at 300 K. Total and atomic projected phonon densities of states are shown at the right panel.

Next, we analyzed atomic structures of the $R\overline{3}c$ and $R3c$ phases as obtained from molecular dynamics simulation at 100 K and 300 K. To perform such analysis, the final 500 steps (out of total 14000 steps) of the molecular dynamics simulation have been considered, to ensure that all the quantities we are interested in are equilibrated. From this data, the new average atomic positions, as well as atomic displacements with respect to the ideal positions at 0 K (Table 3.4) have been recalculated. As expected, Li atoms being the lightest in the system, have the most significant deviations from the initial (ideal) positions, thus we concentrate on Li displacement and do not consider O or Os atoms in the following discussion.

On “cooling” the $R\bar{3}c$ phase down to $T = 100$ K, i.e. below the experimental phase transition temperature, Li atoms shift from their initially symmetric positions (center between the Os atoms) up and down along the c-axis, and as a result, order in an antiferroelectric-like fashion (Table 3.4 and Figure 3.8). Li atoms are not confined (for example, by oxygen octahedra) and, hence, are easily displaced from the centrosymmetric positions as obtained from our molecular dynamics simulations (Table 3.4). Similar to experimental findings [7], we identify anisotropic thermal displacements in Li positions along the c-axis, i.e. z-displacements being an order of magnitude larger compared to those in x and y directions. Experimentally, the shifts of the Li atoms along the c-axis were suggested as a primary order parameter in ferroelectric-like transition in $LiOsO_3$ [7]. At $T = 300$ K the Li atoms oscillate somewhat around the centrosymmetric positions (see Table 3.4). This suggests that our choice of initial relaxed positions as the reference positions, when calculating the phonon dispersion relations at 300 K, is correct. However, this is not the case for the 100 K calculations, and hence, we do not show phonon spectra for $R\bar{3}c$ phase at 100 K (and for $R3c$ at 300 K), since the initial structures are transformed to another structural configuration. In the low-temperature phase $R3c$ at $T = 100$ K Li atoms also vibrate around the ideal positions. At temperature above the phase transition temperature ($T = 300$ K) Li atoms shift collectively along c-axis toward the centrosymmetric positions. The average displacement of Li atoms (average over 500 molecular dynamics steps and over 48 Li atoms in the 2×2×2 supercell) is $\Delta z^{300K} = 0.235$ Å. If we consider one of the Li atoms

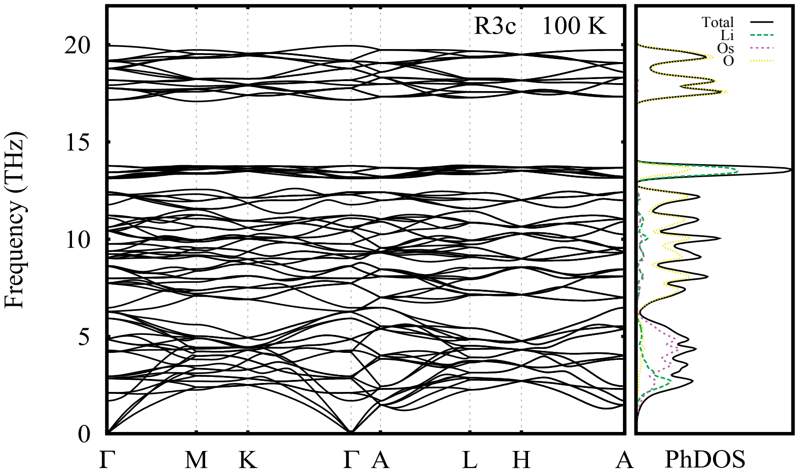

Figure 3.7. Phonon spectra of the low-temperature phase ($R\bar{3}c$) at 100 K. Total and atomic projected phonon densities of states are shown at the right panel.

in our 2×2×2 supercell, e.g. the one in the plane where $z_{LT}^{ideal} = 4.741$ Å, we obtain then the new position $z_{LT}^{ideal} + \Delta z^{300K} = 4.977$ Å. This is very close to the position of Li atom in the centrosymmetric high-temperature phase where $z_{HT}^{ideal} = 4.958$ Å. Hence, the high-temperature phase is likely to be formed by a collective shift of Li atoms towards the centrosymmetric position. However, one should keep in mind $\Delta c = 0.162$ Å difference between the lengths of c-axis in $R\bar{3}c$ and $R3c$ phases. Another important issue related to the molecular dynamics simulations, is that they are performed at constant equilibrium volumes for each phase, and do not take into account a volume change associated with the structural transition.

We have performed additional analysis for the high-temperature phase at 200 K to see whether the antiferroelectric like distortions take place at this temperature, which is just above the experimental transition temperature ($T_c =$ 140 K) and where the centrosymmetric phase is thermodynamically stable. We obtain for $T = 200$ K the following average displacements: $< \Delta z >= 0.015$, $< |\Delta z| >= 0.112$ Å, $< \Delta z_{up} >= -0.090$ Å, $< \Delta z_{down} >= 0.075$ Å. Thus, $< \Delta z >$ is in between corresponding values obtained at $T = 100$ K and $T = 300$ K. Further, by comparing $< \Delta z_{up} >$ and $< \Delta z_{down} >$ we may conclude that the antiferroelectric like distortions are formed even above the phase transition temperature, but with a smaller amplitude.

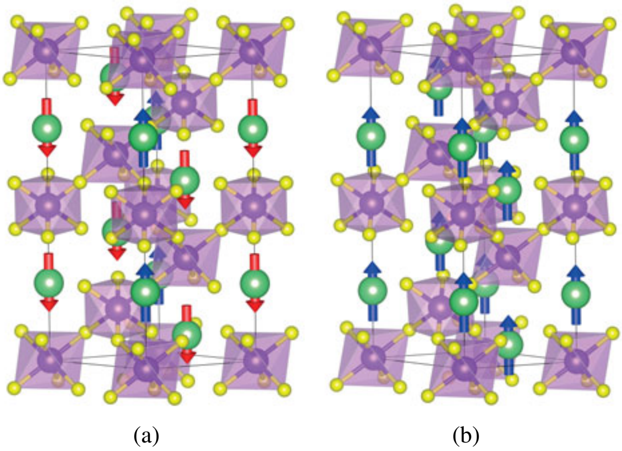
(a) (b)

Figure 3.8. Atomic displacements in HT phase at 100 K (a) and in LT phase at 300 K (b) as obtained from molecular dynamics simulations. This is an idealised picture (not all of the atoms displace at the same amount and in direction in both cases with antiferroelectric- and ferro-like distortions).

In conclusion, *ab initio* molecular dynamics simulations have been employed together with the temperature-dependent effective potential method to address lattice dynamical properties of the $R\bar{3}c$ and $R3c$ phases at finite temperatures. Comparing $T = 0$ K and $T = 300$ K phonon spectra of the $R\bar{3}c$

Table 3.4. *Average atomic displacements (Å) along z-direction with respect to the ideal positions calculated for both phases at* $T = 0$ *K. Note the difference in the length of c-axis: c=12.908 Å for* $R\bar{3}c$ *and c=13.166 Å for* $R3c$*.*

Atom	$< \Delta z^{100K} >$	$< \lvert\Delta z\rvert^{100K} >$	$< \Delta z_{up}^{100K} >$	$< \Delta z_{down}^{100K} >$
Li ($R\bar{3}c$)	0.008	0.163	-0.090	0.098
Li ($R3c$)	-0.010	0.016	-0.029	0.018
	$< \Delta z^{300K} >$	$< \lvert\Delta z\rvert^{300K} >$	$< \Delta z_{up}^{300K} >$	$< \Delta z_{down}^{300K} >$
Li ($R\bar{3}c$)	-0.005	0.087	-0.084	0.079
Li ($R3c$)	-0.233	0.235	-0.245	0.012

phase, we suggest that at elevated temperatures the anharmonic effects harden the soft “ferrolectric” optical mode and provide a stabilization effect. The non-centrosymmetric $R3c$ phase has been shown to be dynamically stable below the transition temperature. Using molecular dynamics simulations, we were also able to show a formation of the Li distortions in the $R3c$ structure at temperatures above T_c. These distortions drive the non-centrosymmetric $R3c$ phase to the high-temperature $R\bar{3}c$ centrosymmetric one upon heating.

4. A random world

Previous chapter has been fully dedicated to crystalline materials. However, depending on the solidification process a liquid/vapor may also condense in a structurally disordered, i.e. *amorphous* state, characterized by the lack of long-range structural order and translational symmetry. The absence of symmetry equivalent atomic sites is the key difference between crystalline and amorphous solids, and which makes a concept of a *unit cell* meaningless when applied to disordered structures. This, in fact, brings tremendous complications to the description of amorphous structures as it precedes the use of mathematical tools such as Brillouin zone, Bloch states or any group theoretical considerations. On the other hand, these challenges lead to new approaches such as Anderson localization theory, mobility edge concept in semiconducting glasses and percolation [82, 8].

Probably one of the most common examples of amorphous materials, organic glass (fused silica SiO_2), has been known for thousands of years. However, glass forming ability of metallic alloys was first demonstrated only in 1960 by Klement *et.al* in $Au_{0.75}Si_{0.25}$ by rapid quenching from the molten state [83]. Since then, it has been conjectured that, in principle, any metal or alloy can be prepared in a non-crystalline structure using sufficiently rapid cooling rates to avoid crystallization [83]. In the late 1970's, metallic glasses have attracted much attention, especially glasses based on iron, due to their soft magnetic properties [84]. Today, intense research in the field of non-crystalline solids is driven by a technological importance of amorphous materials. Successful industrial application include amorphous Se films as xerographic photoreceptors in copying machines, ultratransparent glass fibers for optical communications, application of Ge-Sb-Te thin films for digital versatile disks (DVD), amorphous hydrogenated silicon, a-Si:H, for solar cells and thin-film transistors (TFT), to name a few [8].

This chapter summarizes most important results of Paper III and IV of the thesis. Paper III addresses structural and electronic properties of amorphous W-S-N in relation to its excellent tribological performance to provide a microscopic mechanism behind its superlubricity. Paper IV was aimed to investigate the nature of ultrafast magnetization switching in amorphous ferrimagnet Gd-Fe with respect to its complex atomic and magnetic structures. At first sight, the two topics might seem rather uncorrelated to each other, however, can be unified by the amorphous nature of materials under the study. Hence, an introduction to the preparation and characterization of amorphous solids is necessary and is shortly given below.

4.1 Preparation and amorphous morphology

Preparation

There is a variety of experimental techniques for preparation of amorphous materials, including vapor deposition (evaporation or sputtering), electrodeposition from solution, irradiation or mechanical methods, such as grinding or mechanical alloying, to name a few [84]. However, one of the most commonly used techniques is the *vitrification*, which is the process of quenching of a liquid with high cooling rates. Practically this can be achieved by employing so-called melt-spinning technique. A hot molten metal is injected to the surface of a rotating (usually copper) cylinder. The molten metal solidifies in a very thin film of about 50 μm thick by transforming heat to the metallic cylinder and cools down with a cooling rate of about 10^5 to 10^7 $\mathrm{K{\cdot}s^{-1}}$ [84, 82]. The atomic mobility is heavily suppressed and it is not possible for atoms to arrange themselves into a periodic structure, so the liquid continuously condense into an amorphous state.

It has been also conjectured for a long time that it is not possible to produce pure metallic glasses, as they lack the complexity to "confuse" crystallization [85, 86]. However, it has been recently shown that vitrification of a single-element metallic glasses (Ta, V, W and Mo) is possible by using ultrafast quenching rates of about 10^{14} $\mathrm{K{\cdot}s^{-1}}$ [87]. To achieve such unprecedentedly high cooling rates and suppress spontaneous crystal growth, short (about 4 ns in duration) square electric pulses, have been used to melt two protruded metallic nano-tips made of bcc Ta, V, W and Mo. The heat instantly dissipates through the melted tip towards the device, allowing high cooling rates and further vitrification of the molten substance. The reversible vitrification-crystallization cycle in these single-element metallic glasses have been also controlled by the strength of the electric pulse, and, in principle, can be employed in devices based on a phase change effect [87].

For different materials a minimal cooling rate required for glass formation is different [82, 84]. The composition of amorphous alloys depends on the production method, however, if the critical cooling rate is high, then a wider, or even, continuous concentration range is possible [82, 84]. There are several criteria of glass formation, though. In general, solutes can be destabilized through the difficulty of incorporating additional atoms in the crystalline structures, while the liquid better accommodates chemical disorder and is stabilized through entropy of mixing. Hence, addition of large number of atoms with difference in atomic sizes of components (typically, more than 10-15%) and chemical affinities, introduces frustration to the system which damps the tendency of the alloy to crystallize and prevails the glass transition under cooling [84, 88].

As the solidification occurs below the liquidus (melting) temperature, T_m, and above the glass transition temperature, T_g, the glass formation is easier to achieve when T_m and T_g are as close as possible. One can introduce so-called

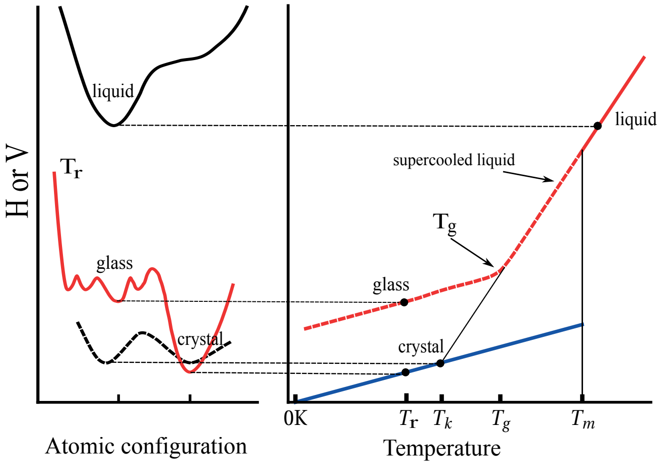

Figure 4.1. Enthalpy H (volume V) of a material as a function of atomic configuration and temperature. In this plot, T_g, T_m, T_r and T_k denote glass, melting, room and Kauzmann temperatures, respectively.

reduced glass formation temperature, T_{rg}, defined as the ratio of the glass transition temperature, T_g, to the melting temperature, T_m. Turnbull has proposed a criterion for the suppression of crystallization [89], and according to it as the reduced glass temperature approaches values about $\sim 2/3$, the nucleation of crystals in the undercooled melt becomes very heavily suppressed. For the phase-change materials, which undergo crystallization-vitrification cycle, the typical value for T_{rg} varies from 0.45 to 0.55 [90]. Hence, the reduced temperature can serve as a guide in search for a good glass formers.

In the context of liquid to glass transition it is interesting to mention the Kauzmann paradox [91]. Figure 4.1 shows typical behavior of the excess entropy, i.e. difference between the entropies of undercooled liquid and crystal, with temperature. As the temperature is lowered, the excess entropy also decreases, and at some point the glass transition occurs. However, extrapolating the curve further down to lower temperatures (still above $T = 0$) the entropy of the liquid becomes lower than that of the crystal, which constitues the *entropy crisis* first recognized by Kauzmann [91]. The temperature at which the excess temperature becomes zero is usually referred to as the Kauzmann temperature, T_K. The simplest way to resolve the paradox is to postulate that the glass transition happens above T_K. Hence, there exists a thermodynamic boundary for the liquid-glass transition set by Kauzmann temperature T_K. The hypothetic glass transition at T_K would result in the most stable and, probably, uniquely determined glass. However, all experimentally produced glasses are metastable and the concept of the *ideal glass* remains abstract.

Characterization

Experimentally, disordered atomic structure manifests itself via broadening of Bragg peaks in the angular distribution of X-rays, electrons and neutrons [82, 8]. A common way to characterize structural properties of such noncrystalline systems with highly stochastic geometries, is to use the radial distribution function (RDF), $g(r)$, which is related to the probability of finding an atom at a particular distance r from the certain fixed atom. The radial distribution function, hence, can be considered as a scalar one-dimensional map of the structure, which gives a local environment, including nearest neighbor distances and coordination numbers, for an average atom of the system. The description of structural properties of amorphous materials is statistical, which is represented by a distribution of interatomic distances as shown in Figure 4.2. RDF usually exhibits few peaks which correspond to the formation of the local short-range structural order, referred to few coordination shells around an atom. However, at larger distances, RDF is almost featureless and the value of $g(R)$ approaches unity, i.e. atoms separated by large enough interatomic distances are completely uncorrelated.

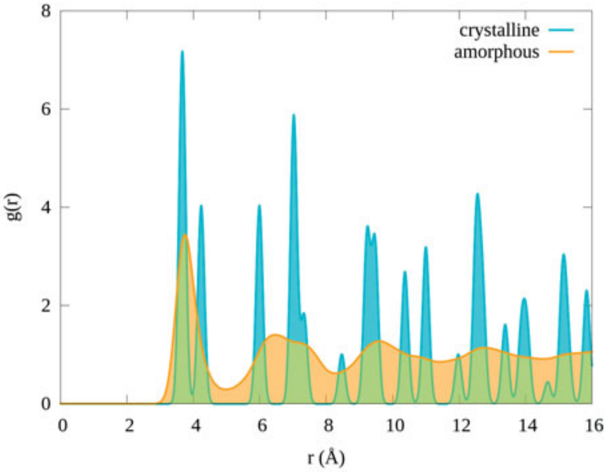

Figure 4.2. Typical radial distribution function g(r) for amorphous and crystalline structures. RDF of a crystalline material at the same characterized by a set of sharp peak at short and large distances, owing a short- and long-range order in crystalline solids. RDF of amorphous structure is almost featureless and similar to one for the liquid state.

As radial distribution function only gives a one-dimensional representation of the structures, no information about the presence of basic atomic configuration (*polyhedra*) which might be dominant in the amorphous system can be extracted from RDF. However, for a system with discrete random atomic structure one can define both Voronoi tesselation, as well as Delauney triangulation, which is dual to it. Amorphous structures can be then described in terms of Voronoi polyhedra of type $\langle i_3, i_4, i_5, .., i_n, .. \rangle$, where n stands for a facet with n edges, and corresponding Voronoi diagram, which gives a distribution of such polyhedra in the sample. Pauling's rule of parsimony [92], which states that the number of chemically different coordination environments of a (ionic) compound tends to be small, however, seems to be not applicable in the case of metallic glasses, where the number of different polyhedra centered at the solute atoms can be large [93]. As a result, in metallic glasses there is no single atomic environment, but rather a plethora of such polyhedra. Voronoi analysis is typically used in addition to common structural analysis via pair distribution function, and has been used to show from the theoretical consideration the existence of local atomic order in amorphous $Zr_{66.7}Ni_{33.3}$ [93].

In the following subsections the first-principles methods for construction of amorphous materials are briefly discussed. Further, we give a short introduction to the fields of tribology and ultrafast magnetization dynamics, followed by the discussion of the main results of Papers III and IV.

4.2 Modelling of amorphous solids

To find a reliable set of atomic positions which would accurately characterize the local environment in a non-crystalline disordered structure, which does not possess long-range translational symmetry and, as a result, can not be described in terms of a unique set of atomic positions, can be a rather daunting task. Through years various structural models have been proposed to describe the disordered materials on atomic level. These include Bernal's hard spheres random close packing appropriate for structures of simple metallic glasses, continuous random network model for covalent amorphous materials, and random coil model for description of polymeric organic glasses [82]. With development of *ab initio* calculations several distinct techniques for construction of stochastic geometries from first principles have become widely available, e.g. molecular dynamics [27], Monte-Carlo [94] and reverse Monte-Carlo simulations [95]. Molecular dynamics has been used to study amorphization of silica SiO_2 [96], amorphous Se [97], tetrahedrally-coordinated amorphous carbon (*ta*-C) [98], structural properties in glassy As_2Se_3 [99] and $Si_{1-x}Ge_x$ [100], generated by means of *ab initio* annealing, studies of electronic properties of amorphous ZrO_2 [101], atomic packing and short-to-medium-range order in amorphous alloys based on transition metals Zr-Pt, Zr-Pd, Ni-Nb [93], and the anomalous transition from liquid-metal to amorphous-semiconductor in Ge [102], to name a few. Molecular dynamics is our method of choice for modelling triboactive self-lubricating W-S-N thin films on atomic level (Paper III), thereby a short overview of molecular dynamics as applied to amorphous structures is given below.

In molecular dynamics approach, stochastic geometries are produced in a "melt-and-quench" fashion in analogy with the experimental glass formation process. The system is melted at high temperatures and equilibrated for a sufficiently long time followed by fast quenching. Standard cooling rates in molecular dynamics are of the order 10^{12} K/s [93], which are several orders of magnitude larger compared to laboratory cooling rates (usually in the range of 10^5 - 10^7 K/s) [84, 82]. The quenching rate in molecular dynamics simulations can be varied, and it has been shown that structural properties are independent[1] of the rate used in the calculation [93]. However, equilibration process in molecular dynamics simulations is rather expensive in terms of computing time as it requires *ab initio* force calculations. An alternative is to use so-called stochastic quenching method [103, 104, 105] that is based on a statistical mechanical description of monotoatomic liquids introduced by Wallace [103]. The method allows to circumvent computationally expensive temperature eqiuilibration in molecular dynamics by only considering quenches from the random atomic configurations. Stochastic quenching method is employed in this Thesis for construction of a model atomic structure of amorphous ferrimagnet Gd-Fe (Paper IV) and the basic ideas behind this method are discussed in the following subsection.

4.2.1 Stochastic quenching method

Stochastic quenching method is based on a single-random valley approximation from vibration-transit theory [103, 104, 105]. Vibration transit theory, originally developed for the monoatomic metal liquids [103], states that the atomic motion can be described by oscillations within a nearly-harmonic valley in the potential energy landscape, $\Phi(\gamma)$ (see Fig. 4.3). These local vibrations are interspersed by transits from valley to valley. Certain equilibrium atomic configuration correspond to energy minima of each valley, and can be referred to as a *structure*, γ. The structures are either crystalline or amorphous, while amorphous can be either completely random or have remnants of crystalline symmetry. However, for a system with large enough number of particles N the potential energy landscape is dominated by degenerate random valleys corresponding to amorphous structures. These random valleys have the same potential energy properties and, as a result, the same macroscopic properties (radial distribution functions, bond angle distributions, densities of states etc.). In the thermodynamic limit, $N \to \infty$, it is then sufficient to find one of such random valleys in the potential energy landscape to obtain a reasonable model of a disordered structure.

To construct stochastic structures a minimum information is required, which only includes knowledge of chemical composition and density of a system under study. By knowing the density, a volume of a cubic cell is selected to give the density identical to the experimental one. A constraint on interatomic distances is introduced in order to avoid a possible overlap between the atoms, as it can lead to numerical instabilities during the structural optimization (quenching). Such constraint excludes undesired atomic configurations with higher energies, and thus reduces the volume of effective $3N$ configuration space. At the next step atomic positions are chosen randomly, and the randomness of the structures can be verified by calculating radial distribution function. The constrained stochastic structures are hence prepared independenly of any internal atomic interaction. Finally, quenches are performed directly from random configurations using any optimization method, e.g. conjugate gradient method. In principle, there is no guarantee that the quenches will condense in a random structure and not in a crystalline one, until the thermodynamic limit is reached. This has to be tested for each system separately, however, it has been shown that approximately 150-200 atomic configurations give accurate structural properties [105].

---

[1] This is, of course, true to some extent. In Ref. [93] the quenching rate has been varied between 4×10^{13} and 4×10^{12} K·s^{-1}.

Stochastic quenching method has been initially tested and verified on monoatomic systems including metallic Na, V and Al [105]. The method have been further shown to provide accurate atomic configurations not only for monoatomic metals but also for multicomponent compound $Zr_{52.5}Cu_{17.9}Ni_{14.6}$ $Al_{10}Ti_5$ (Vitreloy 105) [105], complex amorphous metal carbides, such as Zr-Si-C, where a competing metallic and covalent bonding result in a complex atomic network [106]. The method has been successfully used to model amorphous alumina Al_2O_3 and to show a formation of peroxide ions while molecular dynamics failed [107]. By employing stochastic quenching method it has been predicted, and experimentally verified, that antiferromagnetic chromite oxides $YCrO_3$ and $YbCrO_3$ undergo insulator-to-metal transition under amorphization [108]. Thus, stochastic quenching method have been demonstrated as a powerful technique for theoretical investigations of a variety of amorphous materials with distinct interatomic bonding types.

4.3 Applications to tribology

Energy dissipation associated with friction is ever-present phenomena in any machinery device, ranging from hard disk drives, which use rotating elements, to aerospace components. *Tribology* is a branch of materials science related to interacting surfaces in relative motion and covers such topics as *friction*, *wear* and *lubrication*. *Friction* is a resistive force opposing a sliding motion of contacting surfaces. In some cases a high friction is necessary, e.g. to keep mechanical constructions stable or to light matches, which is also an excellent example of tribochemical reaction. However, a low friction is desired in moving and rolling parts of machines, that would allow to reduce energy consumption and increase lifetime of engineering equipment. *Wear* is a con-

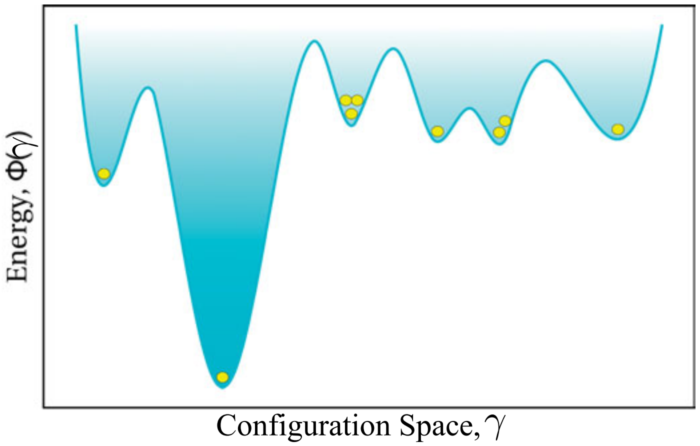

Figure 4.3. Schematic representation of the potential energy landscape of a system of N particles in $3N$-dimensional configuration space. Yellow circles represent possible condensations in various valleys through the procedure of stochastic quenching.

tinuous removal or shift of material at the contact area as a result of sliding or rolling against a countersurface. According to a common classification [109], it is possible to distinguish between adhesive and abrasive wear, wear caused by surface fatigue and due to tribochemical reactions. Some or a combination of these factors might be present and result in degradation or failure of tribo-surfaces. Friction and wear are not unique characteristics of a certain material, but rather a property of a system as whole, including mating surfaces, contact load and environment conditions in which these properties are measured. Friction and wear are not correlated, i.e. high friction may correspond to low wear, and low friction can be accompanied by high wear. To minimize responses of a tribo-system, i.e. friction and wear, and allow machinery to operate on higher loads and longer cycles, a *lubricant* that separates sliding surfaces and prevents a direct solid-on-solid contact is used. Therefore, apart from development of novel cutting-edge materials, an importance of production of fluid lubricants or sustainable low-friction hard coatings to reduce energy losses associated with heating of interacting surfaces, and to prolong machinery duty cycles, is hard to overestimate.

Two major types of lubricants may be distinguished, i.e *liquid* and *solid*. Liquid lubricants such as mineral, synthetic oils and esters have been known for quite a long time and are currently widely used in industrial applications. There are certain advantages of using liquid lubricants, as they provide cooling of the contact area, transfer away wear debris, which might be the source of additional friction, and there is also a possibility to control the temperature of the contact in a narrow range by employing the viscous properties of the liquid. Liquid lubricants can also provide a relubrication of the damaged surface area. However, a number of factors must be considered to select a proper lubricant for a specific application. This include the environmental conditions in which the lubricant should operate, such as temperature, humidity or presence of any reactive medium, such as liquid oxygen. Due to the adverse effects of the liquid lubricants on the environment, various control strategies and legislations impose additional requirements for lubricants, such as non-toxicity, biodegradability and compatibility with all of the materials it comes in contact to. In addition, at extreme operational conditions including very high or very low temperatures or contact pressures, radiation or ultra-high vacuum, or when liquid lubricants are not desired or considered as contaminant, solid lubricants, in the form of hard coatings, may be the only choice to control friction and wear. Most solid lubricants perform well at extreme pressure ranges, and their lubricating properties are less sensitive to fluctuations in temperature. In addition, they are relatively resistant to aqueous solutions or chemically aggressive environments, may provide better thermal and electrical conductivity, and can be stored for a long time [110]. Hence, in many cases solid lubricating coatings are more beneficial compared to their liquid counterparts.

A primary function for protective hard coatings is typically to enhance wear resistance. However, nowadays, one of the major priorities for hard coating development has been to combine wear resistant properties together with friction reduction to achieve longer wear life and duty cycles. Such solid lubricants, including graphite and transition metal dichalcogenides (TMDC), which are discussed in more details below, offer outstanding tribological performance due to a layered structure. However, there are solid lubricants which lack layered atomic arrangements, but still provide very low friction and wear, such as soft metals (In, Pg, Ag etc.), diamond and diamond-like carbon (DLC), certain oxides (Re_2O_7, B_2O_3, MoO_3, V_2O_5 with friction coefficients of μ=0.1-0.3 [111]), polytetrafluoroethylene, better known as teflon, and others [110]. Low friction coefficients (μ=0.1) can be also achieved for TiN when sliding against itself [112]. Even smaller values (μ=0.01-0.05) have been measured for diamond-like carbon sliding against SiN [113] and for diamond coatings sliding against diamond [114]. Amorphous diamond-like carbon yields one of the smallest friction and wear coefficients compared to other solid lubricants [115]. In general, solid lubricants provide friction coefficients in the range μ=0.002-0.2 depending on the operating conditions [110].

Coatings that spontaneously form and maintain a *tribofilm*, i.e. a film developed in the interface between the mating surfaces, and which acts as a lubricant, are referred to as *tribo-active*. These self-lubricating coatings provide not only protective, but also low-friction properties. Such tribofilms are typically few tens of nanometers thick and can have the same composition as of the coating material itself, but with different atomic arrangement resulting in reduced shear strength, however, often they may have different chemistry. With the formation a tribofilm, a coating takes the role of the substrate, while tribofilm acts as the lubricating thin film. It can be shown, that in general, for excellent performance it is advantageous to have as hard as possible substrate under the hard coating, as this will allow to improve the load support, avoid deformation of the coating and decrease the area of contact [116, 117].

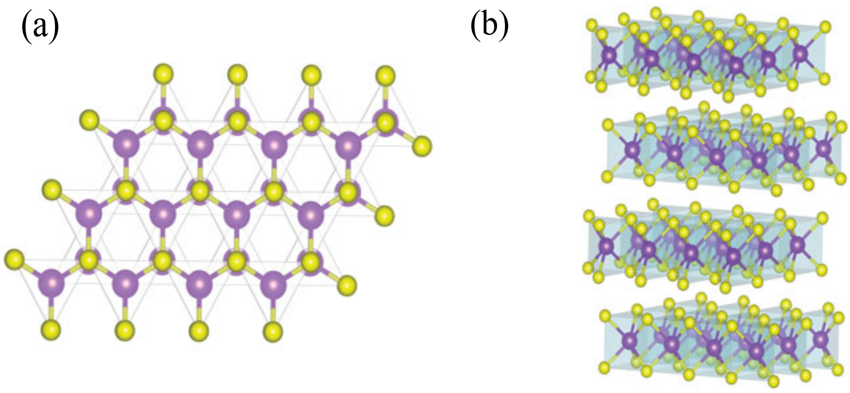

Figure 4.4. Typical structure of transition metal dichalcogenides. Transition metal atoms are shown in purple, while chalcogen are represented by yellow color.

Coatings based on transition metal dichalcogenides (TMDC) with formula unit MX_2, where M is the transition metal and X is chalcogen (S, Se, Te), with excellent solid-lubricating MoS_2 and WS_2, have been studied for decades for engineering applications, and quite recently with the discovery of graphene, interest in TMDC, especially in 2D layers of TMDC, have been renewed again. Some of the transition metal dichalcogenides of group VIII-X are found in non-layered structures, while those of group IV-VII crystallize predominantly in layered structures [10]. The lamellar structure (Figure 4.4) of such dichalcogenides is remnant to that of graphite, with transition metal atom M sandwiched between two layers of chalcogen atom X with typical thickness of the M-X-M layer of 6~7 Å [10]. The coordination of the transition metal atom M in TMDC is either trigonal prismatic (D_{3h}), or octahedral (O_h) (antiprismatic), i.e. each metal atom is coordinated by 6 chalcogen atoms. The bonding within the X-M-X layer, is predominantly covalent in nature. Interaction between the X-M-X layers is weak van der Waals attraction, which is the source of large degree of anisotropy in these systems that give rise to the variety of structural, chemical, electronic and mechanical properties. Due to weak interaction between the layers, there is a variety of polymorphs and stacking sequences associated with bulk TMDCs, with most common being 2H, which is hexagonal with two X-M-X layers in the sequence, and 3R, rhombohedral with three units of X-M-X in the stacking sequence. The chemistry of bulk TMDC is diverse, ranging form insulating HfS_2 and semiconducting (MoS_2, WS_2) to metallic NbS_2 and VSe_2 [10]. Exotic phenomena such as superconductivity, charge density waves and Mott transitions have been reported for some of the bulk TMDC as well ($NbSe_2$ [118], TaS_2 [119]). Single layers of TMDC can be synthesized through exfoliation or bottom-up synthesis [10], and were shown to be stabilized by formation of ripples similar to graphene [120, 121]. The change of electronic structure has been shown in monolayer MoS_2 compared to the bulk, such that at Γ point the band gap is indirect for the bulk and shifts to the direct band gap for the monolayer MoS_2 [122, 123]. This was attributed to quantum confinement effect and change of hybridization between S p_z and Mo d orbitals [122, 123, 124]. This indirect to direct band gap transition is also expected for all MoX_2 and WX_2 dichalcogenides as a result of size effect [125, 126]. Control of the valley pseudospin and applications of TMDC to valleytronics have been also discussed in Ref. [127]. Below we restrict ourselves the discussion only to the properties of low-friction TMDCs, such as WS_2 and MoS_2.

The mechanical properties of TMDC are dictated by weak interaction between the M-X-M layers and strong structural anisotropy. The shear strength along the basal planes is very small and allows easy sliding of M-X-M units with respect to each other, and due to this some of TMDC, such as MoS_2 and WS_2, serve as self-lubricating materials. A prototype system, MoS_2, has been extensively used in aerospace industry due to its stability and low friction in ultra high vacuum [128]. The friction coefficient for MoS_2 can be as low as $\mu \sim 0.01$ providing ultra-low friction, and unprecedentedly long wear lives, up to million of cycles in dry air [129]. The absence of dangling bonds (they appear only at the edges) make the basal planes of WS_2 and MoS_2 inert with respect to reactions with environment, and also explains the degrading friction properties of MoS_2 in humid air. However, not all of the layered TMDC can be characterized as good lubricants with intrinsic low friction properties, some of them are poor lubricants or even abrasive [9]. As discussed above, electronic properties of TMDCs vary substantially, hence a relationship between lubrication performance and electronic structure might be essential to explain this difference in lubrication properties as suggested by Fleischauer in Ref. [9]. The general idea of Ref.[9] can be illustrated on the example of prototype MoS_2 (WS_2) and poor $NbSe_2$ (NbS_2, $TiSi_2$, VS_2 etc.) lubricants, which share the same layered atomic structure, but different electronic properties. Based on molecular orbital theory all accessible orbitals for M (M from group VI transition metals, i.e Mo, W) and S in MS_2 are filled to form strong intralayer bonding, while this is not the case for Nb, what allows interaction between the neighboring layers and results in higher friction. Moreover, electrostatic forces between the layers of TMDC can enhance or reduce the lubricity of these solids. For instance, in good TMDC-based lubricants the region of negative electric charge is concentrated within the “sandwich” layer, such that chalcogen layers are positively charged. This creates a Coulomb repulsion between the “sandwich” layers which results in an easy interlayer slip. Therefore, alternation of the electronic structure by doping may convert $NbSe_2$ into a good lubricant, and conversely, MoS_2 (WS_2) into a poor one.

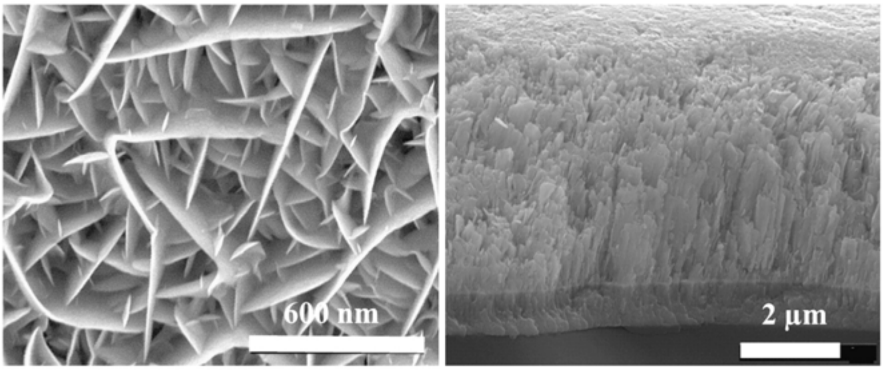

Figure 4.5. Morphology of TMDC thin films. Taken from Ref.[130].

Mechanical properties of deposited MX_2 films also depend on the orientation of the basal planes with respect to the substrate [9]. In type I films slip planes are oriented perpendicular to the surface of the substrate, such that structurally MX_2 consists of randomly oriented and loosely packed platelets. Such columnar morphology leads to the formation of wear debris, and can contribute to the oxidation process when the film is exposed to humid air. The adhesion of such coatings is poor and they are easily degraded. Most of thin films with columnar morphology also show a various degree of porosity and smaller density compared to the pure molybdenite MX_2. Type II films have slip planes parallel to the substrate and are characterized by good lubrication and antiwear properties. Therefore, it is preferred to prepare MX_2 thin films with coplanar orientation. This constitutes a paradox for layered TMDC, as the same basal planes required to obtain good adhesion to the substrate, provide the film with extremely low shear strength for good lubrication [9].

Typically, lubricants are developed to perform at some certain conditions, however, the new generation, or so-called “chameleon coatings” allow self-adaptation under different operating conditions, including wide temperature changes, and are based on composite materials. For instance, self-adaptation of a nanocomposite WC/DLC/WS_2 aimed for potential aerospace applications, have been shown in Ref. [131]. Another studies have been focused on production of TMDC nanotubes [132, 133] and fullerene-like TMDCs, such as hollow WS_2 nanoparticles (with size > 30 nm) [134, 135]. The latter have been shown to perform better than common bulk 2H-WS_2 and 2H-MoS_2 in terms of friction, wear and lifetime of the lubricant. This was related to chemical inertness of the hollow particles, which allows nanoparticles to roll, rather than slide in the contact, and to prevent contact between the mating surfaces. However, despite promising performance in laboratory conditions, these materials seem to be impractical for industrial applications [130].

As discussed earlier in this chapter, due to anisotropic structure, TMDCs can serve as excellent solid lubricants with friction lower than μ =0.01, with the lowest friction (μ =0.001) reported for MoS_2 in ultra high vacuum [136]. In fact, friction of order μ =0.01 is more than sufficient for practical applications. However, there are certain difficulties associated with the use of pure TMDC. One reason has been already mentioned, and this is a formation of randomly oriented WS_2(MoS_2) platelets oriented perpendicular to the substrate surface during the film deposition by magnetron sputtering. Orientation responsible for low friction, with van der Waals planes aligned parallel to the substrate, can be achieved only for thin films with thickness below tens of nanometers [137]. Next, pure TMDC can react with environment forming WO_{3-x} (MoO_{3-x}) oxides, which do not possess low-friction properties and, therefore, are not desired. It has been shown that storing disulfide WS_2 (MoS_2) in presence of H_2O or O_2, rather than in inert environment such as N_2, strengthens the bonding between the layers resulting in degradation of the film and higher friction. Finally, hardness of TMDC is rather low compared to other coatings, e.g. DLC, and typically lies in the range 0.3-2 GPa [130].

Hence, many studies have been addressed to improve the mechanical properties of TMDC with the general approach to modify the chemical composition of the coatings by alloying TMDCs with third components (Ti, Cr, Au, Al, Pb, and Ni [138, 139, 140, 141]). An improvement of wear resistance and load-bearing capacity was evident, with the most successful alloying probably being MoS_2 with Ti, or MoST^{TM} by Teer Coating Ltd, which were commercialized and introduced to the markets [130]. However, many metals are poor lubricants and are prone to formation of oxides, which are not desired in a sliding contact. Therefore, to optimize tribological performance of TMDC non-metallic N and C might be a good choice, as the oxides of their oxides are gaseous and may easily leave the contact. When co-sputtered with non-metallic elements, N and C, mechanical properties of WS_x improve substantially [11, 142], e.g. hardness for coatings containing C/N reaches 5.5 GPa, while W-S films it is about 0.5 GPa. However, addition of C and N with content greater than 20 at.% makes the structure of W-S-N(C) films structurally featureless, i.e. amorphous [11]. Denser W-S-N(C) films with increased hardness and better adhesion to the metallic substrate can be produced by introducing Ti or Cr interlayers [143, 144, 145], however, with no improvement on tribological properties. Further, W-S-N films deposited by magnetron sputtering with the 34 at.% of N was shown to yield virtually disappearing friction coefficient ($\mu < 0.003$) in dry N_2 and humid air environment [12], which is almost an order of magnitude smaller than traditional TMDC-based thin films. The observed ultra-low friction have been shown to be induced by formation of a WS_2 tribofilm with the easy-slip planes accommodated parallel to the sliding direction [12]. This lubricating layer is therefore supported by underlying hard amorphous W-S-N. This allow small contact area and provides support for self-ordering of the WS_2 platelets on the outermost surface, which also results in continuous regeneration of the worn contact layers. The films are extremely wear resistant and are not worn until about 2.1 million laps with load of 20 N, which correspond to removal of WS_2 "sandwich" layer every 500 laps [12].

However, the atomic structure and bonding arrangements in amorphous W-S-N, which provide optimal conditions for formation of WS_2 tribofilm and ultra-low friction are not known. These questions are addressed in Paper III of this thesis, which was aimed to elucidate the nature of the chemical bonding and structure of amorphous W-S-N in relation with its outstanding tribological properties. This was done by obtaining realistic atomic models of amorphous W-S-N by extensively employing "melt-and-quench" technique within *ab initio* molecular dynamics simulations, as well as employing experimental extended and near edge X-ray absorption fine structure (EXAFS and NEXAFS) techniques for structural analysis. The quality of the generated amorphous samples was controlled by comparing the experimental and theoretical EXAFS signals. Further, the structures of amorphous W-S-N were systematically analyzed in terms of local atomic environment and electronic properties, to provide a microscopic mechanism behind the experimentally observed ultra-low lubricity in the triboactive W-S-N film.

4.3.1 Atomic structure behind ultra-low friction in amorphous W-S-N thin films

To analyze excellent tribological properties of amorphous W-S-N thin films we generated three atomic structures of $W_{0.33}S_{0.33}N_{0.34}$ (labelled further as A,B and C) for which ultra-low friction was observed [12], by means of molecular dynamics simulations. The reliability of our atomistic models was examined by comparing EXAFS oscillations, $\chi(k)$, with simulated EXAFS signals, $\chi_i(k)$, $i = A,B,C$, for the three atomistic models. As EXAFS gives an information of the average local environment, the average $\chi(k)$ from the individual $\chi_i(k)$ have been calculated as well (Figure 4.6). A remarkable agreement between the experimental and theoretical curves up to 9 Å^{-1} in reciprocal space illustrates an accuracy of our model structures and allows further analysis of structural and electronic properties of W-S-N.

Directing our attention to the theoretical RDF curves (Figure 4.7), we find that the structures show no partial crystallization and exhibit a short-range order up to 6-7 Å. Due to disordered atomic structure of amorphous W-S-N there is no single nearest neighbor distance between any atomic pair, but a distribution of these distances, as represented by RDF (Figure 4.7). Average values of nearest neighbor distances for various atomic pairs are collected in Table 4.1 together with the experimental data and corresponding bond lengths in a

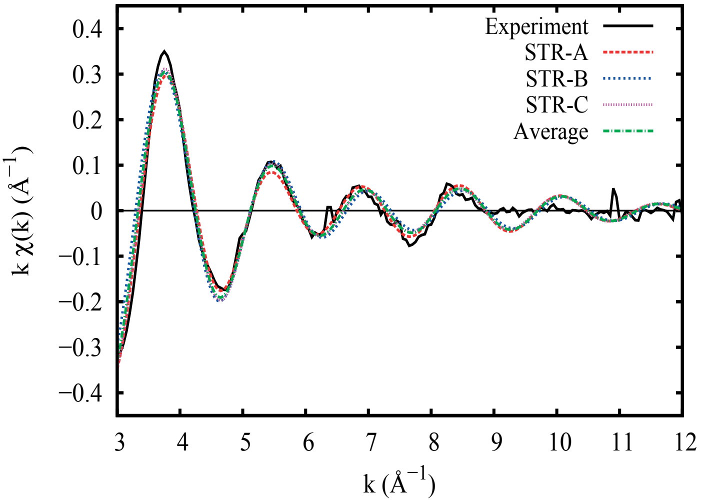

Figure 4.6. Comparative k-weighted $\chi(k)$ oscillations of the experimental EXAFS for the film with 31 at.% and simulated EXAFS from the three different theoretical structures for $W_{0.33}S_{0.33}N_{0.34}$ as well as their weighted average.

number of selected reference systems. For instance, theoretical W-W nearest neighbor distance (2.835-2.921 Å) for the amorphous W-S-N was found to be slightly longer than the W-W bond length in hexagonal WN (2.826 Å and 2.893 Å [146]), and *bcc* W (2.735 Å [147]), suggesting a weaker bonding between W atoms in amorphous $W_{0.33}S_{0.33}N_{0.34}$ compared to these crystalline solids. No comparison was possible with the EXAFS data due to a broad distribution of W-W bond lengths, which were ignored in our analysis. The W-S nearest neighbors distances (2.366-2.389 Å) are in excellent agreement with the data obtained from EXAFS measurements (2.387±0.015 Å), but are shorter compared to the W-S bond length in hexagonal WS_2 [148, 149, 150]. Also, for W-N atomic pairs, the theoretical nearest neighbor distances (1.941-1.964 Å) are in good agreement with the experimental one (1.925±0.027 Å), as well as comparable to the W-N bond length in WN (2.065 Å in cubic WN [151], 2.188 Å in hexagonal WN [146]) and in organometallic $W\text{-}N_2$ complexes (1.967-1.972 Å [152, 153]). We attribute shorter W-S and W-N bonds in amorphous $W_{0.33}S_{0.33}N_{0.34}$ compared to corresponding bonds in crystals to the reduced coordination of S and N, respectively (Figure 4.8). The theoretical S-S and S-N nearest neighbor distances are significantly longer compared to the corresponding bond lengths in crystalline S_8 [154] and tetrasulfur tetranitride S_4N_4 [155]. Interestingly, we find additional peaks in theoretical S-S (for structure *C*) and S-N (for structures *A* and *C*) RDF curves with smaller peaks located at shorter distances. These peaks are due to formation of S-S and S-N bonds with bonds lengths of 2.101 Å and 1.577-1.650 Å, which are

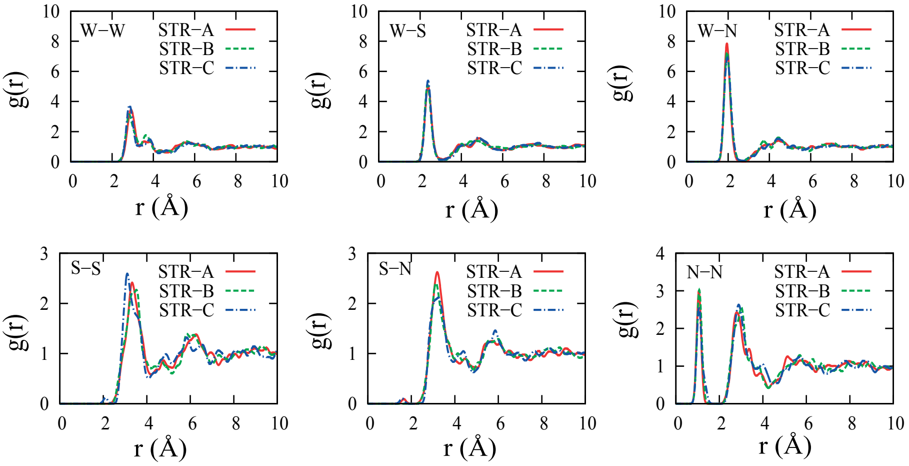

Figure 4.7. Radial distribution functions calculated for amorphous $W_{0.33}S_{0.33}N_{0.34}$ for various atomic pairs.

in good agreement with those in S_8 and S_4N_4.

The radial distribution function calculated for N-N atomic pairs show a separate peak at $\sim$ 1 Å , which corresponds to the formation of N_2 molecules in the amorphous matrix of W-S-N. Approximately 21-24 at % of total number of nitrogen atoms in the structure were found to be bonded in N_2 molecules with interatomic distances 1.108-1.127 Å. The effect of O-O dimerization (formation of peroxide) have been also previously reported for amorphous alumina Al_2O_3 [107] and silica SiO_2 [156]. Our simulations show that N_2 molecules accumulate in a cage formed by S atoms, with S-N interatomic distance varying from 2.776 Å to 4.186 Å . These nearest neighbor distances are approximately 1.2-2.8 Å longer than the S-N bond distance, and indicates the absence of strong interaction between N_2 molecules and surrounding S atoms of the cages. Hence, these N_2 molecules might be considered as quasi-free. We also found that some of the N_2 trapped in the cages were bonded to W atoms, which result in weaker N-N triple bond and, therefore, longer N-N bonding distances in the range of 1.120-1.467 Å, i.e. longer compared to that of quasi-free N_2 molecules (1.108-1.127 Å). For the structure *A*, which gives the best description of $W_{0.33}S_{0.33}N_{0.34}$ (as shown by comparison between experimental and theoretical EXAFS signals) the sulphur cage, containing five quasi-free N_2 molecules (out of 7 found in the structure *A*) and other neighboring N and W atoms, is shown in Figure 4.9. The length of this cage is about the size of the cubic unit cell used in molecular dynamics simulations ($\sim$ 15.2 Å), with the diameter of cross-section about 10.6-11.5 Å. This indicates that the size of the theoretical unit cell might be not enough to capture the essence of formation of N_2 and their clustering within the sulphur pores, and larger sizes should be considered. Further, by analyzing NEXAFS spectra of the W-S-N sample with 37 at.% N (the film with the highest N concentration among the deposited samples considered in our work) a N_2 N1$s \rightarrow \pi^*$ resonance was observed (not shown here). Resulting NEXAFS signal compares quite well to a spectrum for a gaseous N_2 with corresponding Lorentzian lifetime broadening 0.6 eV larger compared to the isolated N_2 molecule.

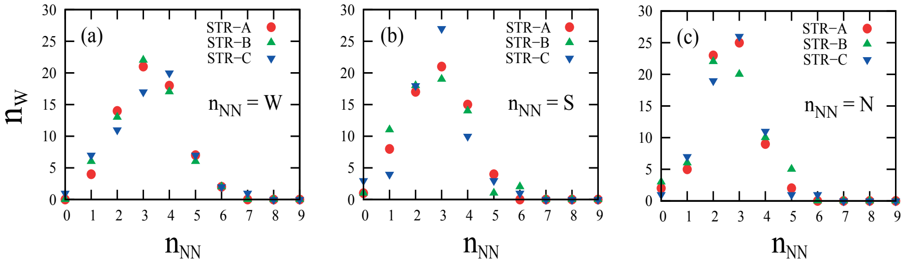

Figure 4.8. Local environments calculated for three different structures of amorphous $W_{0.33}S_{0.33}N_{0.34}$ obtained by molecular dynamics simulations. n_W denotes the number of W atoms surrounded by the number n_{NN} of nearest neighbors.

Another important characteristic of the local atomic environment is given by coordination numbers. From theoretical calculations we obtain that on average, W atoms are coordinated by 3.2 W, 2.7 S and 2.7 N atoms. The latter two are in a good agreement with experimental coordination numbers n_{NN}=2.7 for S and n_{NN}=2.7 for N atoms determined by EXAFS. Analyzing the local atomic environment for W (Figure 4.8), we find that most of them have 2-4 W, 2-4 N and 2-3 S nearest neighbors. The average coordination number is decreased from 6 in crystalline WS_2 to 2.7 in $W_{0.33}S_{0.33}N_{0.34}$ suggesting the presence of WS_3 building blocks in the amorphous structure.

Next we proceed with the analysis of the electronic properties of $W_{0.33}S_{0.33}N_{0.34}$ by considering theoretical density of states (DOS) (Figure 4.10). From finite DOS at the Fermi level, we predict metallic character of this compound, for optical properties as well as electron transport (Figure 4.10(a)). Main contribution to finite DOS at the Fermi level is due to W 5d states, similarly to crystalline hexagonal WN (Figure 4.10(b)). Metallic character of amorphous W-S-N is in sharp contrast to semiconducting WS_2 with a band gap of 2.1 eV [157] (Figure 4.10(c)). The resistivity of amorphous metals is usually significantly smaller compared to their crystalline counterparts, with typical values in the range 100-200 $\mu\Omega$ cm, however, higher values up to $\sim$600 $\mu\Omega$ cm have been also reported for alloys containing metalloid elements [158]. In our work, measured sheet resistivity for the amorphous W-S-N thin films with 31 at.% of N, which is compositionally close to $W_{0.33}S_{0.33}N_{0.34}$ studied from first-principles, is 432 $\mu \cdot \Omega$ cm. As expected, this value lies in the range of resistivity for WN (9 $\mu \cdot \Omega$ cm [159]) and WS_2 (10^5 $\mu \cdot \Omega$ cm [157]).

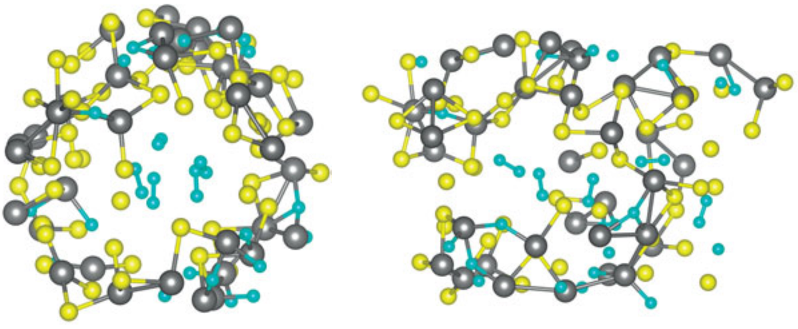
(a) *YZ plane* (b) *YX plane*

Figure 4.9. The cross-section (a) and side views (b) of a large cage, containing five N_2 molecules in the theoretical structure *A* of amorphous $W_{0.33}S_{0.33}N_{0.34}$. W, S and N atoms are shown in gray, yellow and cyan, respectively.

Analyzing orbital projected density of states, W $5d$, S $3p$ and N $2p$ orbitals hybridize in the energy range from about -8 to 0 eV and correspond to the formation of strong covalent W-N and W-S bonds, similar to crystalline WN and WS_2 (Figure 4.10(a)-(c)). Covalent W-N bonds appear at lower energies compared to W-S, and therefore are in general stronger. Despite the chemical preference, the number of W-S bonds is slightly larger than for W-N bonds, since fewer N atoms are available for bond formation between W and N, as approximately 20 % of N atoms are engaged in the formation of N_2 molecules. The number of metallic W-W bonds is almost twice smaller than the number of W-N and W-S bonds, therefore W mainly forms bonds of covalent character with N or S. Partial density of states for nitrogen atoms can be separated into two contributions, with one coming from N atoms which are bonded in N_2, and those which are not. In particular, N $2s$ and $2p$ orbitals of quasi-free N_2 molecules show up deep in energies (about -23 eV), and correspond to the formation of σ_2 molecular orbital, similar to that in free N_2. At the same time, there are few N_2 molecules, located in a smaller cage, which are bonded to W atoms, and this is reflected in the hybridization of N $2p$ states of N_2 and W $5d$ states in the energy range from -8 to -5 eV (Figure 4.10(a)). Due to formation of bonding with W, W-N bond length becomes weaker and therefore larger (2.047-2.288 Å) compared to average W-N bond (1.941 Å) found for the generated amorphous structures.

Further, from Bader population analysis we found that W atoms have in average 4.1 electrons, which means that almost 30% of W valence electrons are transferred to N and S for bond formation. In crystalline WN and WS_2 there are 4.71 and 4.97 valence electrons on average, hence, in amorphous W-S-N electron transfer from W to N and S is larger compared to hexagonal tungsten nitride (WN) and disulphide (WS_2), respectively. Sulphur atoms,

Table 4.1. *Theoretical and experimental nearest neighbor distances (Å) in amorphous* $W_{0.33}S_{0.33}N_{0.34}$ *and the deposited film with 31 at.%, respectively. The distances in the corresponding crystalline or organometallic materials are listed for comparison. The numbers given in parentheses correspond to the separate peaks in the RDFs.*

Atomic pair	Theory STR-A	STR-B	STR-C	Experiment	Reference
W-W	2.921	2.835	2.844	-	2.826 [146]
W-S	2.389	2.366	2.387	2.387±0.015	2.478 [148], 2.411 [149] 2.405 [150]
W-N	1.941	1.955	1.964	1.925±0.027	2.188 [146] 1.967 [152], 1.972 [152] 1.991 [153]
S-S	3.326	3.423	3.103 (2.101)	-	2.031-2.045 [154]
S-N	3.193 (1.650)	3.137	3.186 (1.577)	-	1.596-1.634 [155]
N-N	1.118	1.130	1.174	-	1.095 [160]

instead, gain more negative charge in amorphous W-S-N compared to WS_2, which is also reflected in the average number of electrons (6.64 for W-S-N and 6.52 in WS_2). Nitrogen atoms in W-S-N in average have less valence electrons (6.16) compared to crystalline WN (6.29). In amorphous $W_{0.33}S_{0.33}N_{0.34}$, N atoms which are not engaged into formation of N_2 molecules gain almost twice more electrons compared to S atoms. Overall, charge transfer analysis shows that covalent W-N and W-S bonds are polarized, i.e. have some ionic character.

Charge density distribution map calculated for $W_{0.33}S_{0.33}N_{0.34}$ (Figure 4.10 (e),(d)) schematically shows interaction between N atoms bounded in N_2 interact with N of other N_2 in the cage, as well as with the S atoms, which form the cage. The number of valence electrons calculated by means of Bader analysis for N_2 molecules (10.02-10.25) shows an extra charge compared to the isolated N_2 (10.00). It implies a charge transfer from S atoms of the cage to N atoms bonded into N_2 molecules and trapped within the cage. These interactions between trapped nitrogen molecules and S atoms that build up the cage, even though being weak, compared to the strong N-N bond, allow to keep N_2 inside the cage.

These theoretical findings allow us to relate the structural properties of amorphous W-S-N to its excellent tribological performance. As it has been discussed already in the introduction, the low-friction properties of WS_2 and other TMDC can be explained by weak van der Waals interaction between the “sandwich” layers, which slide easily along the basal planes. Even though it is theoretically predicted that the “sandwich” layers can slide against each other almost without friction [161], the optimum performance is not necessarily reached by depositing a crystalline film with layers perfectly aligned parallel to the substrate surface. It has been shown that a smooth and mechanically stable surface is desired to support the forming tribofilm in the contact, and in addition, an introduction of third element to WS_2 increases the density and hardness [11, 144, 142]. Amorphous W-S-N have been also shown to perform

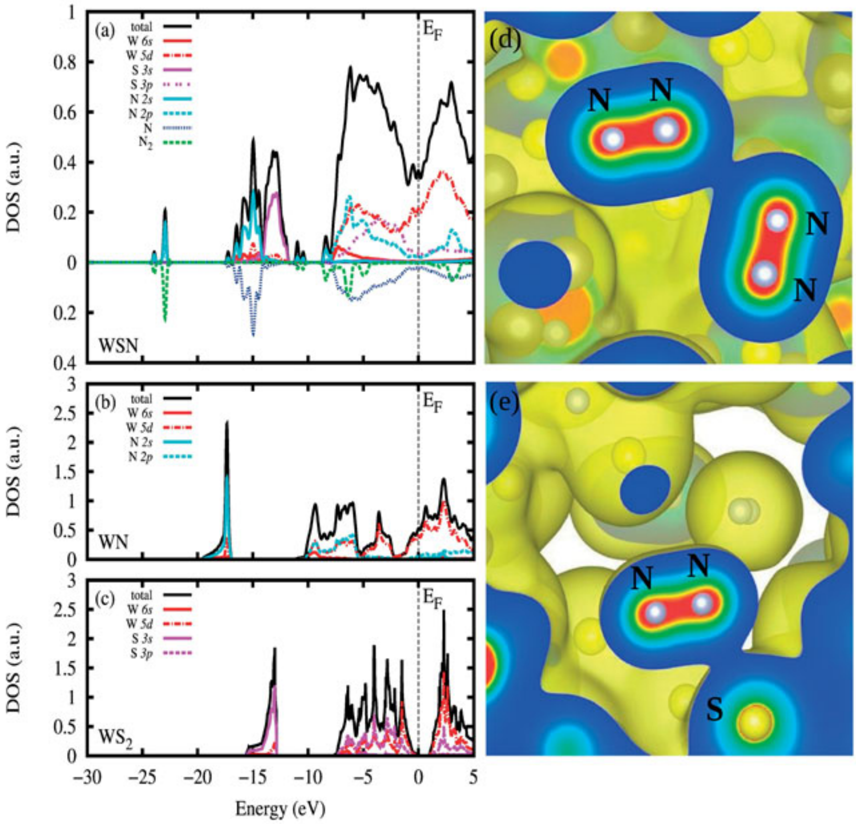

Figure 4.10. (a) Partial density of states calculated for theoretical structure *A* of amorphous $W_{0.33}S_{0.33}N_{0.34}$. In the lower part of panel (a) we show contributions to the DOS from N atoms of N_2 molecules (green dashed curve) and from those, which are not bonded in N_2 (dotted blue curve). The Fermi level, E_F, is shown by vertical dashed line. (b, c) Total and partial DOS calculated for hexagonal WN and WS_2. Charge density distribution between two N_2 molecules (d) and between a N_2 molecule and a S atom of the surrounding cage (e). The maximum isovalues for these isosurfaces 0.007 $Å^{-3}$ (d) and 0.009 $Å^{-3}$ (e).

with exceptional friction properties in dry conditions [11, 12]. Therefore, the presence of crystalline or nano-crystalline WS_2 in the deposited thin film is not required for formation of WS_2 tribofilm, but rather the availability of its constituents for a continuous formation. Thus, WS_2 may be formed at the outermost surface of the amorphous film by the diffusion of individual atoms, rather than by formation of large WS_2 platelets. It should be also stressed that addition of the third element to WS_2 matrix should also not hinder the formation of the tribofilm and N in this sense is the excellent option since its oxides are gaseous and may easily leave the matrix. As we have shown, there is a part of nitrogen atoms which form N_2 which are trapped in large sulphur cages. Hence, we propose the mechanism for ultra-low friction in amorphous $W_{0.33}S_{0.33}N_{0.34}$ as a result of dense and stable surface, good availability of W and S to form WS_2 platelets, absence of high-friction or high-wear secondary phases and easy removal of excess nitrogen from the amorphous matrix in the tribological contact.

4.4 Amorphous magnetism

Generally, several classes of disordered magnetic materials can be distinguished, including spin glasses, which are characterized by quenched-in spins aligned in a random directions, and amorphous ferromagnets, with the latter being the subject of this chapter. A complex structure of amorphous solids poses questions such as what happens to magnetic order in the absence of periodic atomic arrangement? How disorder on atomic level affects the magnetic properties of materials? What the magnetic properties can tell us about the underlying atomic structure?

Magnetic properties of amorphous ferromagnets essentially depend on the underlying atomic configurations. The stochasticity of amorphous structures gives rise to a distribution of magnetic moments even at low temperatures, with the narrowest distribution found in amorphous rare-earth compounds due to localized $4f$-states, shielded from the neighboring atomic environment [162]. Contrary, due to a broad moment distribution, transition metals can coexist both in magnetic and non-magnetic states within the same alloy, for example in $\mathrm{Si}_{1-x}\mathrm{Fe}_x$ and $\mathrm{Ge}_{1-x}\mathrm{Fe}_x$ close to Fe composition $x = 0.50$ [163], while being non-magnetic in $\mathrm{Y}_{1-x}\mathrm{Fe}_x$ close to $x = 0.33$ composition [164].

Another important aspect imposed by the randomness of the structure is the distribution in the exchange coupling constants (J_{ij}), due to their dependence on the interatomic distance. If the exchange coupling between different pairs of spins is not invariably positive (negative) and may have either sign, the magnetic system is therefore *frustrated*, favoring canting in magnetic structure, and may lower the critical ordering temperature in amorphous materials. Single-site anisotropy, i.e. a local easy axis defined for each distinct atomic site, is one more consequence of stochasticity of the amorphous structures. Thus, the direction of each magnetic moment is defined by the competition between the exchange and anisotropy interactions. The local anisotropy term is generally insignificant compared to exchange interaction in transition metals, however, might be important for rare-earths, especially those of non S-state [165]. Therefore, an ultimate description of magnetic order in amorphous ferromagnets include knowledge of magnetic moment distribution in each sublattice. Experimental techniques for resolving magnetic moment distribution involve measurements of hyperfine field distribution by nuclear magnetic resonance (NMR) or Mössbauer spectroscopy [166].

This chapter deals with the theoretical framework for magnetization dynamics in amorphous ferrimagnet GdFeCo induced by ultrashort femtosecond laser pulses [13, 14]. This rare-earth-transition metal alloy can be defined by two magnetic subnetworks (Gd and FeCo) which follow decoupled dynamics after being pumped by laser pulse. All-optical switching makes GdFeCo an exceptional candidate for application in magneto-optical data storage and processing technology. Here, employing a multiscale approach by combining first principles density functional theory with the stochastic quenching method and atomistic spin dynamics, we investigate the magnetization dynamics in a row of GdFe alloys. In the following sections an introduction to femtosecond magnetism and spin dynamics simulations are given along with our theoretical findings.

4.4.1 Ultrafast magnetization dynamics

Recording and storing information in modern magnetic data storage devices, such as hard-disk drives, is based on altering the magnetization direction by means of external magnetic fields with a typical strength of about 1 T [167]. Charactersitic magnetization reversal time for such fields is in the order of nanoseconds. A constant technological development of high-performance and high-density storage devices have triggered an immense interest in a possibility to speed up the process of magnetization reversal at shorter timescales, including subpicosecond regime. Recently, there have been several technique proposed to control fast magnetization switching. Precessional switching is one of such strategies for magnetization reversal with a characteristic time of few hundreds of picoseconds [168]. Another one is manipulation of magnetization direction by spin-polarized electric currents that feed (or drain) the system with spin angular momentum [169, 170], known as spin-transfer torque effect. Technology based on this effect, for example commercially available magnetic random access memories (MRAM), are still under development, offering nowadays reorientation of magnetization on the same timescale of 100 ps.

All these considerations currently set a threshold for magnetization switching process, $\tau_{thr} = 100$ ps, which is a characteristic time of spin precession. This gives rise to principal questions, such as what are the fundamental limits on the manipulation and control of magnetization in a magnetic media? Another question to be addressed is a possibility to reverse magnetization direction in the subpicosecond regime without applying magnetic field. It turns out that ultrashort optical pulses can be an alternative to magnetic fields, and manipulation of magnetic order by femtosecond laser pulses opened avenues for information processing technologies, as well as gave rise to the ultrafast magnetization dynamics field.

The field of femtosecond magnetism stems from the pioneering work by Beaurepaire et al. [171], who used 60 fs laser pulse to excite 22 nm Ni thin films. Subsequently, a large quenching of magnetization was found within the first picosecond (Figure 4.11), i.e. on a timescale of exchange interaction. This result was rather surprising as the maximum speed of demagnetization was expected to be governed by the spin-lattice coupling which is rather weak in Ni. In the following studies similar behavior was observed in a number of transition metals such as Fe [172] and Co [173]. However, earlier time- and spin-resolved photoemission experiments carried out on Gd, roughly estimated demagnetization time of $\tau = 100 \pm 80$ ps [174], revealing three orders of magnitude slower spin dynamics in this rare-earth compared to transition metals such as Ni. Control of magnetic order by optical excitations has been also demonstrated in semiconductors (ferromagnetic $Ga_{1-x}Mn_xAs$ [175, 176]), dielectrics (iron borate $FeBO_3$ [177]) and half-metals (Sr_2FeMoO_6 [178], CrO_2 [179]). Demagnetization process in ferromagnetic insulators is, however, several orders of magnitude slower compared to ferromagnetic metals, due to the absence of intrinsic free electrons.

Femtosecond laser pulses can induce a plethora of different phenomena in magnetically ordered media. If the thickness of the magnetic thin film is comparable to the penetration depth of a femtosecond laser pulses, typically 10-15 nm, then ultrashort laser pulses can act as a picosecond "anisotropy field" that triggers formation of a coherent spin waves [180]. The spin waves have been detected in Ni films, but also in permalloy $Ni_{0.80}Fe_{0.20}$ characterized by a very low crystalline anisotropy. It has been also shown that femtosecond excitations can induce modification of magnetic order, e.g. antiferromagnetic to ferromagnetic structural phase transition in FeRh system [181]. Ultrafast laser pulses have been shown to induce a complete hysteresis loop reversal in the ferromagnetic semiconductor (Ga,Mn)As [182]. More complex magnetization dynamics is expected in materials with multiple magnetic sublattices. As an example, laser-induced magnetization reversal in amorphous ferrimagnet TbFeCo [183], and GdFeCo [184, 13, 14] have been experimentally observed. All-optical ultrafast excitation of magnetic skyrmions have been recently shown in insulating chiral magnet Cu_2OSeO_3 [185].

An experimental setup for femtosecond laser experiments typically employ a pump-and-probe technique. A femtosecond laser pulse is split into the intense pulse in the optical spectra range to pump the material and trigger the magnetization dynamics, and a weaker probe pulse, delayed in time with respect to the pump pulse, to detect the laser-induced changes in the magnetic order. Pump-and-probe experiments typically employ magneto-optical techniques, such as magneto-optical Kerr effect (MOKE), or Faraday effects to monitor the process. More recent techniques include magnetic second harmonic generation (SHG) for probing surface and interface magnetism [186], and element-specific X-ray magnetic circular dichroism (XMCD) [187], which by measuring the dichroism of transition from core levels to empty states above Fermi level allows to probe local magnetic order. No dependence of the subpicosecond magnetization dynamics on the external magnetic field has been reported for Ni thin films [188]. By measuring time resolved magneto-optical Kerr effect in Ni demagnetization time has been shown not to be affected by pump helicity [189].

At the energy range where femtosecond laser pumps the material, i.e. in the optical range, only electrons respond to electromagnetic excitation, and therefore absorb almost instantaneously energy of the laser. Ultrashort femtosecond laser pulses bring the system out of equilibrium creating non-thermal (hot) electrons within ~100 fs. Due to Coulomb scattering, the population of non-thermal electrons decrease in time, while the population of thermal electrons increase. An excess energy is further transferred to spin and lattice heat baths leading to a final reduction of the magnetic order. This assumption postulates different dynamics of spin, electronic and lattice degrees of freedom and allows introduction of phenomenological three temperature model (3TM) to describe the energy flow between the three heat reservoirs [171]. Within this model effective temperatures are assigned to electron (T_e), spin (T_s) and a lattice (T_l) subsystems and the temporal evolution of the system is given by the coupled differential equations as

$$
\begin{aligned}
c_e \frac{dT_e}{dt} &= -g_{el}(T_e - T_l) - g_{es}(T_e - T_s) + p(t) && (4.1)\\
c_s \frac{dT_s}{dt} &= -g_{es}(T_s - T_e) - g_{sl}(T_s - T_l) && (4.2)\\
c_l \frac{dT_l}{dt} &= -g_{el}(T_l - T_e) - g_{sl}(T_l - T_s), && (4.3)
\end{aligned}
$$

where, c_e is the electronic specific heat, c_s and c_l are the magnetic and lattice contributions to the specific heat, g_{el}, g_{es}, g_{el} define coupling between the heat reservoirs, and $p(t)$ represents the laser source. Typical temperature profiles are shown in Figure 4.10(b). It must be emphasized, that effective temperatures can only be assigned if the heat reservoirs are in thermal equilibrium. While the absorption of optical energy brings the electron system to highly non-equilibrium state resulting in the formation of non-Dirac electrons, the 3TM must be taken into consideration carefully, as imposing a certain temperature to a system on such a short timescales might be invalid.

Although 3TM successfully interprets the processes followed by femtosecond laser pulse excitation in terms of the energy flow picture, it gives no microscopic explanation of the demagnetization process. No unique quantitative model of the femtosecond dynamics have been presented over the years. The complications arise from the fact that the interactions between three different systems (electron, spin and lattice) on different time and length scales must be taken into account within the same description. At the same time a successful model should be able to explain diverging demagnetization timescales in transition metals (Ni, Co and Fe) and rare-earth Gd.

A step towards understanding the microscopic mechanism behind ultrafast demagnetization, is to recall that in quantum mechanics, the magnetization $\mathbf{M}$ is built up by the expectation values $\langle \mathbf{S_e} \rangle$ and $\langle \mathbf{L_e} \rangle$ of spin and orbital angular momentum, $\mathbf{M} \propto \langle \mathbf{L_e} \rangle + g\langle \mathbf{S_e} \rangle$, where g is the spin g-factor. Decrease of $\mathbf{M}$ in the demagnetization process, if we only consider transition metals where the orbital momentum is nearly completely quenched, should also lead to a decrease of the expectation value of spin $\langle \mathbf{S_e} \rangle$. Generally, in the demagnetization process, angular momentum must be drained from the spin system, and as a result of angular momentum conservation, should be absorbed by the electron

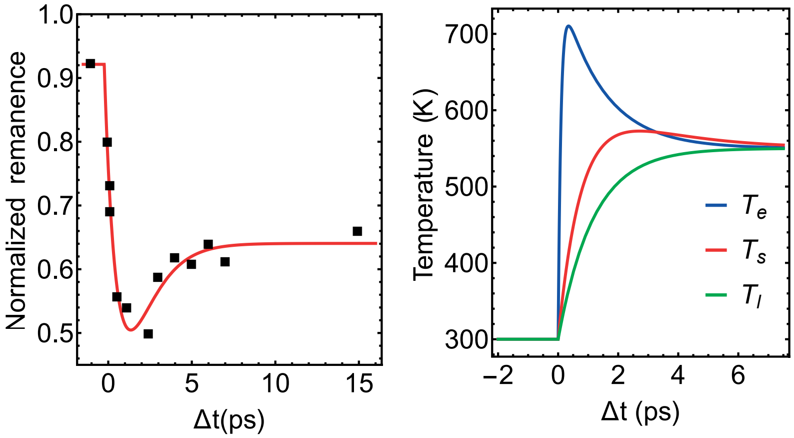

Figure 4.11. (a) Ultrafast quenching of magnetization in Ni thin films as measured by MOKE signal. (b). Schematic representation temperatures of heat reservoirs in phenomenological three-temperature model. Redrawn from [171].

and lattice systems. Thus, another challenge associated with understanding the microscopic mechanism of ultrafast demagnetization, is finding the channels for angular momentum dissipation.

Transfer of angular momentum from the spin system in the demagnetization process ultimately depends on the spin-scattering mechanism. Several models for the angular momentum flow have been suggested including (a) inelastic electron-spin wave scattering, which is effective in case of relatively low photon excitation energies [190, 191]; (b) Stoner excitations which involve a spin reversal [167], and (c) Elliott-Yafet mechanism, i.e. transfer of spin angular momentum to the lattice through the spin-orbit coupling [192, 193]. The Elliott-Yafet mechanism uses the fact that due to spin-orbit coupling, $\mathbf{H}_{\mathbf{so}} = \lambda \mathbf{L} \cdot \mathbf{S}$, the spin eigenstate is no longer an eigenstate of a full Hamiltonian, $\mathbf{H} = \mathbf{H}_0 + \mathbf{H}_{\mathbf{so}}$. As a result, an electronic state is a superposition of two states with the majority $|\uparrow\rangle$ and minority $|\downarrow\rangle$ contributions, i.e. $\psi_{\mathbf{k},\uparrow} = a_{\mathbf{k}}|\uparrow\rangle + b_{\mathbf{k}}|\downarrow\rangle$, where $\mathbf{k}$ is the wave vector, and hence, there is a probability of spin-flipping. To quantify the spin-flipping process the spin-flip matrix can can be introduced through $s_{\mathbf{k}+\mathbf{q},\downarrow;\mathbf{k},\uparrow} = \langle \psi_{\mathbf{k}+\mathbf{q},\downarrow} | \mathbf{H}_0 + \mathbf{H}_{\mathbf{so}} | \psi_{\mathbf{k},\uparrow} \rangle$. The spin-mixing parameters have been calculated from first-principles for several transition metals, including Ni, Co and Fe [194], and it turned out that the spin-mixing parameters for these $3d$ metals are about 25 times larger compared to that of Cu. Despite the fact that it supports the mechanism of angular momentum transfer to lattice via Elliott-Yafet mechanism, it should be noted that this is a single-electron model which considers spin-flip events as independent.

Another attempt to predict magnetization dynamics is based on the microscopic three-temperature model (M3TM) to describe spin-flip mechanism. This model introduces certain parameters into consideration, such as relation between the Curie temperature and magnetic moment on a sublattice, T_c/μ, which accounts for the strength of exchange interaction, and a_{sp}, a spin-flip parameter, which is related to elementary spin-scattering processes and defines thermal coupling between electron and its spin. This approach has been demonstrated to explain "fast" and "slow" demagnetization times in various metals ("slow" rare-earths Gd and "fast" transition metals Ni, Co, Fe, respectively) [195].

Superdiffusive mechanism proposed as a driving mechanism for ultrafast demagnetization process [196], instead, considers spin flips as rare events and is based on difference between transport properties of majority and minority spin channels. Recent experimental studies [197, 198] show that this mechanism can indeed contribute to the demagnetization, however this contribution strongly depends on the system's composition [199], and, in addition, this effect is not dominant in simple ferromagnetic films on insulating substrates [200].

Application in magneto-optical technologies requires materials with a sustainable compensation temperature, T_M, as well as Curie temperature, T_C, above 500 K [201]. A class of rare earth (RE) - transition metal (TM) amorphous alloys ($RE_{1-x}TM_x$) which show peculiar magneto-optical properties and sensitivity of the magnetic properties with respect to small variations in composition, are considered to be of great industrial importance [202, 203]. These materials can be prepared in a wide range of concentrations, are stable at room temperature and do not require addition of glass forming elements (such as boron) to be stabilized in amorphous phase. Ferrimagnetic alloys, formed by rare-earth and transition metals may possess a magnetization compensation temperature, T_M, defined as a temperature at which magnetic moments of two magnetic sublattices cancel each other leading to a zero net magnetization. Amorphous alloys based on rare-earths and Fe have critical temperatures T_c below the crystallization temperature for any Fe concentration [204]. It has been demonstrated that structural and magnetic properties of amorphous $RE_{1-x}TM_x$ with respect to their crystalline counterparts vary dramatically. It has been shown that amorphous $TbFe_2$ and $GdFe_2$ are ferrimagnetically ordered with Curie temperatures about 40% lower compared to the corresponding crystalline Laves phases [205]. The T=0 K saturation magnetization of amorphous and crystalline $GdFe_2$ have the same values ($3.9\mu_B$), however, magnetization in amorphous $TbFe_2$ ($4.2\mu_B$) is significantly lower than in crystalline $TbFe_2$ ($5.4\mu_B$). Anomalously, magnetization isotherms measured for amorphous YFe_2 show no long-range magnetic order above 3.5 K, and suggest the presence of weakly interacting magnetic clusters [205]. Another example of materials for magneto-optical memory applications are amorphous ternary and quaternary rare-earth transition metal intermetallic compounds, such as

$Tb_{1-x}(Fe,Co)_x$, $(Gd,Tb)_{1-x}Fe_x$ or $(Gd,Tb)_{1-x}(Fe,Co)_x$. In these compounds the concentration range is almost continuous, therefore the ratio $(1-x)/x$ and Co concentration can be tuned to obtain required compensation T_M and Curie T_C temperatures [206]. For instance, thermomagnetic writing using laser pulses was proposed in amorphous GdTbFe using 16 ns laser pulses [207]. It was shown that the magnetization time critically depends on the initial temperature of the sample, and faster switching times required initial temperatures below the compensation point T_M.

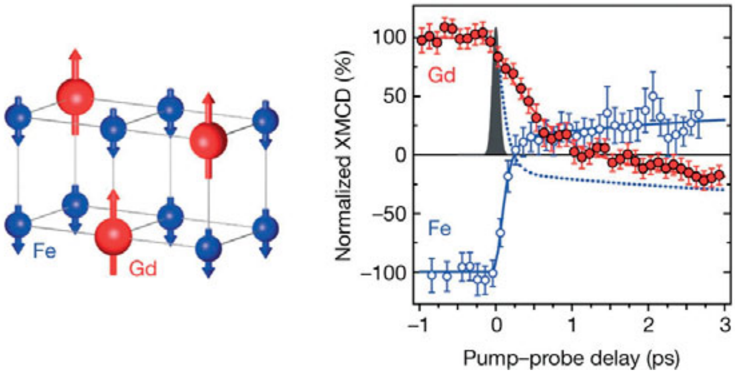

Figure 4.12. (a) Antiferomagnetic coupling between Gd and Fe magnetic subnetwroks in the ground state. (b) Magnetization dynamics on Gd and Fe subnetworks measured by time-resolved XMCD. Adapted from [13].

Ultrafast magnetization reversal in amorphous GdFeCo

Element-specific X-ray magnetic circular dichroism technique has been used to study optically induced magnetization reversal in ferrimagnetic GdFeCo alloys with Co concentration of 9.5 at.% [13]. The material is formed by two non-equivalent spin sublattices antiferromagnetically coupled in the ground state (Fig. 4.12). The ultrafast magnetization reversal has been shown to occur via a transient state, where Fe(Co) and Gd magnetic sublattices were found to be parallel, i.e. ferromagnetically coupled, for about 1 ps, despite the antiferromagnetic ground state coupling. The magnetization dynamics in the two sublattices is essentially different, with collapse of Gd sublattice at about 1.5 ps with subsequent magnetization reversal, while Fe sublattice showed an order of magnitude faster switching time of 300 fs (Fig. 4.11(b)).

Different theoretical models have attempted to explain these experimental findings. For instance, in Ref. [208] a general theoretical framework for ultrafast laser-induced spin dynamics in multisublattice magnets was introduced to account for longitudinal relaxation of both relativistic and exchange origin. It was argued that non-equivalent sublattices exhibit distinct dynamics when relativistic effects dominate. Another explanation was provided in Ref. [209], where the thermally induced deterministic magnetization switching was ascribed to the excitation of two-magnon bound states.

Recent X-ray diffraction experiments [14] identified chemical and magnetic inhomogeneities in amorphous GdFeCo alloys, which were ascribed to as the route of distinct spin dynamics at the nanometer length scales (≈10 nm). This result was somewhat unexpected regarding earlier observations with spatial-averaging techniques [13, 210] showing faster switching on Fe sublattice. However, faster Gd spin reversal was observed in Gd-rich nanoregions, with Gd concentration higher than in average sample. At the same time, Fe-rich regions show an opposite trend, i.e. with faster magnetization switching on the Fe sublattice. Hence, in amorphous Gd-Fe alloys, magnetization dynamics strongly depend on the concentration of Fe and Gd in local regions of the sample. It was argued that faster Gd magnetic reorientation is due to non-local transfer of angular momentum regions between Fe $3d$ and Gd $4f$ spins following laser excitations [14].

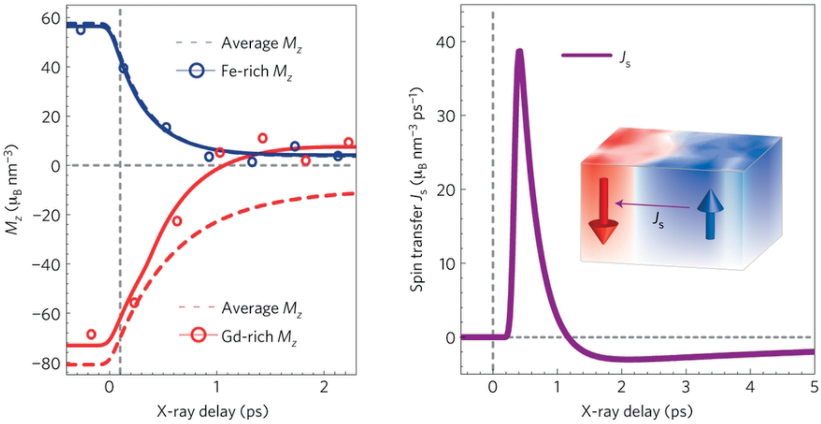

Figure 4.13. (a) Time evolution of the decoupled magnetization dynamics of the Gd and Fe subnetworks measured by resonant X-ray diffraction. (b) Angular momentum flow to the Gd-rich regions. Adapted from [14].

Despite of numerous models proposed for explanation of ultrafast spin reversal in amorphous GdFeCo, none of them address the role of complex underlying atomic structure and inhomogeneous concentration profiles. In this thesis modelling of magnetization dynamics in amorphous ferrimagnet Gd-Fe under the influence of a femtosecond laser pulse is based on a multi-scale approach that couples *ab initio* density functional theory methods with atomistic spin dynamics as implemented in Uppsala Atomistic Spin Dynamics package (UppASD) [211], and heavily relies on the realistic atomic model of GdFe alloy. In the next section theoretical concepts for the description of finite temperature spin dynamics, which gives a clue to the fundamental question on magnetization reversal speed, are briefly reviewed.

4.4.2 Atomistic spin dynamics at finite temperatures

The dynamics of a rigid rotating body in classical mechanics couples the angular momentum **L** of the body and the torque **T** acting on it through the following relation

$$\mathbf{T} = \frac{d\mathbf{L}}{dt}. \tag{4.4}$$

This relation still holds when extended to quantum mechanics by reinterpreting the angular momentum **L** as an operator **S** associated with an electron spin. Recalling that the spin momentum **S** and magnetic moment **M** are related through $\mathbf{M} = -\gamma\mathbf{S}$, where γ is the gyromagnetic ratio, and that the magnetic field **H** exerts torque $\mathbf{T} = [\mathbf{M}\times\mathbf{H}]$ on a magnetic moment **M**, one obtains the following equation of motion for a magnetic moment **M**

$$\frac{d\mathbf{M}}{dt} = -\gamma[\mathbf{M}\times\mathbf{H}]. \tag{4.5}$$

For a system characterized by a discrete set of N magnetic moments $\mathbf{M_i}$, $i = 1...N$, Eq. (4.5) is valid for each individual moment $\mathbf{M_i}$, such that $d\mathbf{M_i}/dt = -\gamma[\mathbf{M_i}\times\mathbf{H}]$. This equation of motion can be then written for a torque of any nature if the so-called effective field $\mathbf{H^i_{eff}} = -\partial\mathscr{H}(\{\mathbf{M_i}\})/\partial\mathbf{M_i}$ is introduced, where $\mathscr{H}(\{\mathbf{M_i}\})$ is the effective spin Hamiltonian

$$\begin{aligned}\mathscr{H} = & -\sum_{i\neq j} J_{ij}\mathbf{M}_i\cdot\mathbf{M}_j + \sum_{i\neq j} D_{ij}[\mathbf{M}_i\times\mathbf{M}_j] + \sum_i K_i(\mathbf{M}_i\cdot\mathbf{e}_K)^2 \\ & - \frac{1}{2}\sum_{i\neq j} Q^{\mu\nu}_{ij} M^\mu_i M^\nu_j - \sum_i \mathbf{B}\cdot\mathbf{M}_i,\end{aligned} \tag{4.6}$$

which includes the exchange, J_{ij}, and Dzyaloshinskii-Moriya, D_{ij}, interactions between moments $\mathbf{M_i}$ and $\mathbf{M_j}$, anisotropies K_i, tensor of dipolar interactions $Q^{\mu\nu}_{ij}$, and the external field **B**. Equation (4.5) corresponds to the time evolution of the conservative system that does not exchange energy with its environment, and thus describes only the precessional motion of the local magnetic moment **M** around the direction the effective magnetic field $\mathbf{H_{eff}}$. To take into account the effect of damping one must include a dissipative term to force the magnetic moment **M** to align with the effective magnetic field $\mathbf{H_{eff}}$. Landau and Lifshitz introduced the phenomenological double cross product form of the damping term into the equation of motion to account for transverse relaxation [212]

$$\frac{d\mathbf{M}}{dt} = -\gamma\mathbf{M}\times\mathbf{H_{eff}} - \gamma\frac{\lambda}{M}[\mathbf{M}\times[\mathbf{M}\times\mathbf{H_{eff}}]]. \tag{4.7}$$

Here the added damping term is constructed such that it is perpendicular both to the magnetic moment and the precession term (see Figure 4.14) and rotates the magnetic moment $\mathbf{M}$ toward the effective magnetic field $\mathbf{H_{eff}}$. The Landau-Lifshitz equation of motion is a good approximation for small damping terms, however, it encounters problems for large damping, for example in FePt thin films with large uniaxial magnetic anisotropy [213]. The problem for large damping terms can be resolved by adding Rayleigh's dissipation function to the Lagrangian formulation of the equation of motion to obtain the Landau-Lifshitz-Gilbert equation [214]

$$\frac{d\mathbf{M}}{dt} = -\gamma \mathbf{M} \times \mathbf{H_{eff}} + \frac{\alpha}{M}\mathbf{M} \times \frac{d\mathbf{M}}{dt}, \tag{4.8}$$

where α is a dimensionless Gilbert damping parameter, which accommodates dissipation of energy and angular momentum, and brings the system to equilibrium. It can be shown that the damping terms in Landau-Lifshitz and in Landau-Lifshitz-Gilbert equations are mathematically identical if one redefines the effective gyromagnetic ratio γ as $\gamma/(1+\alpha^2)$ and setting $\lambda = \alpha$. As a result Landau-Lifshitz equation can be rewritten in the following form

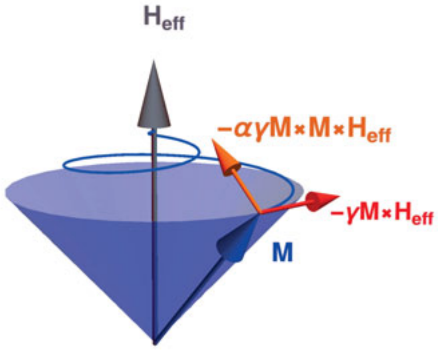
$\mathbf{H_{eff}}$
$-\alpha\gamma\mathbf{M}\times\mathbf{M}\times\mathbf{H_{eff}}$
$-\gamma\mathbf{M}\times\mathbf{H_{eff}}$
$\mathbf{M}$

Figure 4.14. Illustration of the precessional dynamics governed by Landau-Lifshitz equation of motion (Eq.4.7). The precessional moment (shown in red) is responsible for the precessional motion of the magnetic moment $\mathbf{M}$. The damping torque (shown in orange) acts on magnetic moment $\mathbf{M}$ to align it with the effective field $\mathbf{H_{eff}}$.

$$\frac{d\mathbf{M}}{dt} = -\frac{\gamma}{1+\alpha^2}\left(\mathbf{M} \times \mathbf{H_{eff}} + \frac{\alpha}{M}\mathbf{M} \times [\mathbf{M} \times \mathbf{H_{eff}}]\right). \tag{4.9}$$

The difference between the Landau-Lifshitz and Landau-Lifshitz-Gilbert descriptions is negligible for small damping parameters ($\alpha^2 \ll 1$).

Thermal effects can be introduced into Landau-Lifshitz-Gilbert formulation of magnetization dynamics by coupling the system to a heat bath. This is done within Langevin dynamics which is conceptually similar to modelling of Brownian motion of a small particles in a fluid. At finite temperatures the fluctuating magnetic moments are exerted to stochastic torques, then, in the spirit of Brownian picture, the torques can be defined by random fields $\mathbf{s}_i(t)$ introduced for each individual magnetic moment $\mathbf{M_i}$. The effective magnetic field should be then redefined to take into account the random field: $\mathbf{H_{eff}} \rightarrow \mathbf{H_{eff}} + \mathbf{s}(\mathbf{t})$. The stochastic field $\mathbf{s}_i(t)$ thus enters the equation of motion in both the precession and damping terms. We assume that the stochastic field $\mathbf{s}_i(t)$ is Gaussian distributed and fulfills the following criteria for the two first moments

$$\begin{aligned} \langle s_i^{\mu}(t) \rangle &= 0, \\ \langle s_i^{\mu}(t) s_j^{\nu}(t') \rangle &= 2D\delta_{ij}\delta_{\mu\nu}\delta(t-t'), \end{aligned} \tag{4.10}$$

where μ, ν are the Cartesian components of spins. The strength of the thermal fluctuations, D, is chosen according to the fluctuation dissipation theorem, such that $D = \frac{\alpha}{(1+\alpha^2)} \frac{k_B T}{\mu_B M}$, with M being the magnetization of each spin and α is the Gilbert damping parameter. According to relation (4.10), the time average of the stochastic field $\langle \mathbf{s}(t) \rangle$ is zero. The second moment, $\langle s_i^{\mu}(t) s_j^{\nu}(t') \rangle$, or the variance of $\mathbf{s}(t)$, states that the noise is uncorrelated in time (t), space (i, j), in the Cartesian components of spin (μ, ν), and, therefore, has a zero correlation radius. By introducing the stochastic field $\mathbf{s}(t)$, the Landau-Lifshitz-Gilbert equation becomes

$$\frac{d\mathbf{M}}{dt} = -\frac{\gamma}{1+\alpha^2} \left(\mathbf{M} \times [\mathbf{H_{eff}} + \mathbf{s}(t)] + \frac{\alpha}{M} \mathbf{M} \times [\mathbf{M} \times [\mathbf{H_{eff}} + \mathbf{s}(t)]] \right). \tag{4.11}$$

The complexity immediately arise from the fact that due to temporal evolution of spins, the effective magnetic fields $\mathbf{H^i_{eff}}$ are no longer static. Here, the Stratonovich interpretation of the stochastic equation following [215] is used, which preserves the individual spin length. In our calculations, the stochastic fields do not allow significant deviations of spins from the easy magnetization axis, allowing treatment of damping parameter α as a number and ignoring its tensorial nature. Finally, in our atomistic spin dynamics simulations the stochastic Landau-Lifshitz-Gilbert equation (4.8) is evolved according to a semi-implicit integration scheme [216].

4.4.3 Magnetization switching in amorphous Gd-Fe

This chapter closely follows the results presented in Paper IV of this thesis. As discussed in the introduction to this chapter, magnetic properties are intimately coupled to an underlying atomic structure, hence a relevant description of femtosecond laser induced magnetization dynamics in amorphous GdFeCo heavily relies on the validity of the model amorphous structure. Since transition metals Co and Fe belong to one magnetic sublattice, consisting of 3*d*, as well as mobile *s* and *p* spins [14], we ignore small experimental concentrations of Co (9.5 at.%) and consider pure amorphous Gd-Fe compound in our analysis. Complex atomic structure, magnetic order, together with the localized Gd $4f$ states, which require a description within LDA+U approach, make amorphous structure generation from molecular dynamics simulations for Gd-Fe rather computationally costly. Thus, the stochastic quenching method, described earlier in Section 4.2.1, was used to construct amorphous $\mathrm{Gd}_x\mathrm{Fe}_{1-x}$ ($x = 0.24, 0.50, 0.76$) within first-principles approach for structural optimization from the initial random configurations. The atomic models were further verified with respect to interatomic distances and local atomic environment by radial distribution function (RDF) (Figure 4.15, Tables 4.2 and 4.3, respectively). Structural properties of the generated amorphous samples show an excellent agreement with available X-ray diffraction data for melt-quenched Gd-Fe with close concentrations. It has been shown that slightly different structural properties in melt-quenched and sputtered Gd-Fe films are possible, as a result of different preparation conditions [217]. Stochastic quenching does not mimic neither melt-quenching, nor sputtering technique, however, our results in comparison to the experimental data illustrate high efficiency and accuracy of the method. Generated amorphous structures possess very large coordination numbers with up to $\sim$12 neighbors for Gd-Fe pair in $\mathrm{Gd}_{0.24}\mathrm{Fe}_{0.76}$ (see Table 4.1) reflecting highly packed atomic structures of these ferrimagnets, and allowing dense random hard sphere model for their description. The *ab initio* structural models are used as reference systems in our further investigation of magnetic properties of amorphous Gd-Fe.

Table 4.2. *Bond lengths (Å) in amorphous $\mathrm{Gd}_x\mathrm{Fe}_{1-x}$ system. The bond distances in selected crystalline and amorphous systems are listed for comparison.*

System	Gd-Gd	Gd-Fe	Fe-Fe
$\mathrm{Gd}_{0.24}\mathrm{Fe}_{0.76}$	3.47	3.02	2.50
$\mathrm{Gd}_{0.50}\mathrm{Fe}_{0.50}$	3.55	2.98	2.43
$\mathrm{Gd}_{0.76}\mathrm{Fe}_{0.24}$	3.52	2.97	2.44
hcp Gd [218]	3.57	-	-
bcc Fe [219]	-	-	2.54
GdFe_3 [220]	3.21	2.97	2.37
GdFe_2 [221]	3.22	3.08	2.63
am-$\mathrm{Gd}_{0.22}\mathrm{Fe}_{0.78}$ [222]	3.47	3.11	2.57
am-$\mathrm{Gd}_{0.56}\mathrm{Fe}_{0.44}$ [222]	3.54	2.95	2.51

Next, based on the dense random sphere packing model, we constructed larger amorphous structures of $\mathrm{Gd}_x\mathrm{Fe}_{1-x}$ with $x = 0.20-0.30$ containing 1600 atoms (compared to 200 atoms in our *ab initio* calculations) in the vicinity of $\mathrm{Gd}_{0.24}\mathrm{Fe}_{0.665}\mathrm{Co}_{0.095}$ composition for which magnetization reversal have been experimentally observed. The structures were optimized within classical molecular dynamics approach employing LAMMPS code [223]. Interatomic interaction was modelled by Morse potential, and for the relaxation process the experimental distances between different atomic pairs and the potential depths were taken from Ref.[224]. To verify the structures from molecular dynamics simulations a new set of RDF's were calculated and compared with the RDF's obtained for our *ab initio* structures (solid black lines in Figure 4.14). Position of the peaks from *ab initio* stochastic quenching and classical molecular dynamics simulations correspond to practically the same bonding distances, and reflects the accuracy of the models built using molecular dynamics.

Table 4.3. *Average coordination numbers for amorphous Gd_xFe_{1-x} system. Coordination numbers in reference systems are listed for comparison in the lower part of the table. In $GdFe_3$ the coordination for Gd and Fe atoms with different site symmetries is different. Therefore, we show coordination for all inequivalent positions (specified in parentheses).*

System	Gd-Gd	Gd-Fe	Fe-Gd	Fe-Fe
$Gd_{0.24}Fe_{0.76}$	4.6	11.0	3.5	7.6
$Gd_{0.50}Fe_{0.50}$	9.1	5.7	5.7	4.5
$Gd_{0.76}Fe_{0.24}$	10.9	2.4	7.5	2.0
$GdFe_2$ [225]	4	12	6	6
$GdFe_3$ [220]	(3*a*) 2 (6*c*) 1-3	(3*a*) 6-12 (6*c*) 3-6	(3*b*) 6 (6*c*) 3 (18*h*) 1-2	(3*b*) 6 (6*c*) 3 (18*h*) 1-2
am-$Gd_{0.22}Fe_{0.78}$ [222]	3.0	8.8	2.5	7.9
am-$Gd_{0.56}Fe_{0.44}$ [222]	7.5	3.2	4.2	3.0

Exchange parameters essentially define the magnetic order and can be, in principle, calculated from first principles. However, here we use the model exchange parameters from Ref. [226], for neighboring transition metal ($J_{Fe-Fe} = 0.80$ mRy) and rare-earth ions ($J_{Gd-Gd} = 0.15$ mRy) which give the correct Curie temperature for the correspoding bulk materials. For the intersublattice exchange, i.e. between the rare-earth and transition metal lattices, the value $J_{Gd-Fe} = -0.25$ mRy was chosen to fit experimental temperature dependence of saturation magnetization of both Fe and Gd sublattices [226]. The negative value of intersublattice exchange guarantees antiferromagnetic coupling between the rare-earth and transition metal lattices in Gd-Fe ferrimagnet. Magnetic interactions in Gd-Fe in our model are mapped onto a Heisenberg exchange Hamiltonian, $\mathscr{H} = -\sum_{i \neq j} J_{ij} \mathbf{M}_i \cdot \mathbf{M}_j$. The magnetic moments used in our atomistic spin dynamics simulations are 7.6 μ_B and 2.1 μ_B for Gd and Fe, and correspond to the bulk values. It should be emphasized here, that our first principles calculations for Gd-Fe with three distinct compositions ($x = 0.24, 0.50, 0.76$) result in a distribution of the magnitude of the magnetic moments, as well as in non-collinear, i.e. canted, magnetic structure. However, as it has been discussed in Section 4.4.2, our model considers only transverse relaxations of magnetic moments, therefore only one value of magnetic moment is assigned in each sublattices.

Using the model exchange coupling parameters, we performed compensation, and Curie temperature calculations for Gd_xFe_{1-x} alloys for $x = 0.22 -$

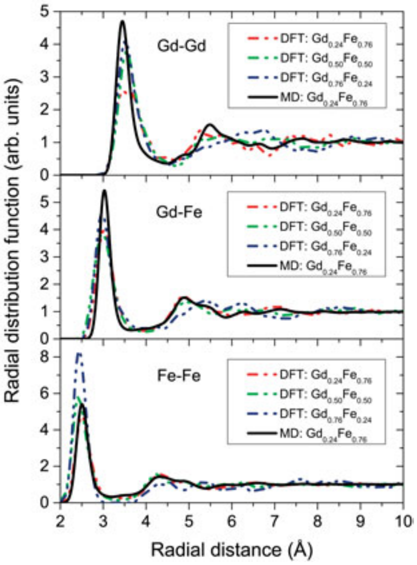

Figure 4.15. Radial distribution function calculated for Gd_xFe_{1-x} with three different stoichiometries. The dashed lines show data calculated with DFT, while the black solid line represents data provided by molecular dynamics calculations.

0.30, which are shown in Figure 4.16 together with the corresponding experimental data. Compensation temperatures (T_M) were obtained by finding a compensation point where the magnetization on the Fe and Gd sublattices were equal in magnitude but opposite in direction, such that the net magnetization vanished. To calculate Curie temperatures (T_C) finite scaling analysis [227] have been used along with the calculation of Binder cumulants [228] defined as

$$U_L = 1 - \frac{\langle m^4 \rangle_L}{3\langle m^2 \rangle_L^2}, \tag{4.12}$$

where m is the magnetization, L represents the size of the system, and $\langle ... \rangle$ denotes the statistical average taken at a constant temperature. It can be shown that in the thermodynamic limit ($L \to \infty$) below the critical temperature, T_c, when there is certain magnetic order, $U_L = \frac{2}{3}$. Above the critical temperature $U_L = 0$, and at T_c Binder cumulant has a critical value, $U_L = U_c$. Hence Binder cumulant can serve as an order parameter in our model. Finite scaling theory states that the value of U_c at the critical temperature T_c does not depend on the system size and is a universal value. Hence, to obtain the critical temperature it is enough to plot the order parameter U_c as a function of temperature T for a set of different system sizes, and simply find intersection of these curves.

As a result of finite scaling analysis we plot the Curie temperatures as a function of Gd concentration (Figure 4.16) showing a remarkable agreement with experimental data. The critical temperature follows a general trend, i.e.

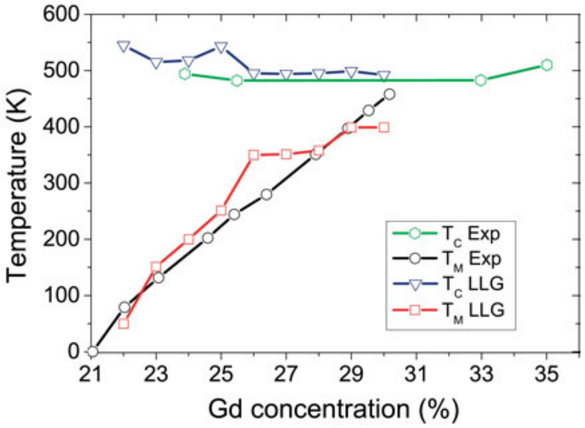

Figure 4.16. Curie (T_C) and magnetic compensation (T_M) temperatures for amorphous Gd_xFe_{1-x} alloys, for different concentrations of Gd. The experimental data has been taken from Ref.[229].

decrease of T_c with increase of Gd concentration. We attribute this magnetic softening in $x = 0.21$ to $x = 0.30$ series to the addition of extra Gd-Gd nearest neighbors, which have a smaller exchange coupling as compared to the Fe-Fe interaction. A deviation from the trend at $x = 0.25$ might be associated with the limited number of atoms used in our models, and, in principle, these fluctuations are expected to vanish in the thermodynamic limit. It has been experimentally shown that compensation temperature in amorphous Gd-Fe alloys is extremely sensitive to small variations in the chemical structure, with increase by ~100 K in T_M when Gd concentration is increased from 22 at.% to 23 at.% [229]. Our simulations accurately reproduce compensation temperatures as well (Figure 4.16), showing a gradual increase with the Gd concentration. The reason for this trend can be referred to a competition between antiferromagnetically coupled Gd and Fe sublattices. Increasing the Gd concentration makes the magnetization of the rare-earth sublattice stronger relative to the transition metal sublattice already at low temperatures. Hence, a higher temperature is required to compensate magnetization on each sublattice.

It must be stressed here that exchange fluctuations due to atomic disorder can also affect the shape of the magnetization saturation curve M_s [230] as well as compensation and Curie temperatures. It has been shown that the influence of the exchange fluctuation parameter $\delta = \sqrt{\langle \sum_{ij} (\Delta J_{ij})^2 \rangle} / \sum_{ij} J_{ij}$ is not negligibly small, and its variation in the range $0 \leq \delta \leq 0.6$ for $Gd_{0.255}Fe_{0.745}$ significantly reduces compensation temperature T_M which ranges between 220 K $\leq T_M \leq$ 295 K [206]. However, we do not consider this effect here, and completely ignore any distance dependence of exchange constants J_{ij}.

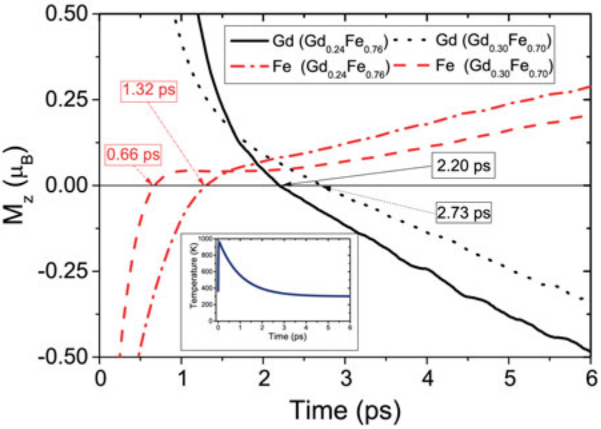

Figure 4.17. Time evolution of the magnetization (M_z) for two different concentrations of amorphous Gd-Fe alloys under the influence of a thermal heat pulse. The solid and dash-dot lines represent the sample concentration $Gd_{0.24}Fe_{0.76}$, while the dash and dot lines are for $Gd_{0.30}Fe_{0.70}$. The magnetization of the two sublattices is plotted separately. In the inset we show a typical temperature profile induced from the laser fluence, as given by the two temperature model.

We further proceed with the dynamic behavior of homogeneous amorphous samples induced by laser pulse excitation using atomistic spin dynamics simulations. Here only temperature effects from the laser pulse were considered, which is modeled by the two-temperature model (2TM) which captures the essential physics of the 3TM model, at the same time allowing to use a simple analytical form

$$T_e = T_{initial} + (T_{peak} - T_0) \cdot (1 - e^{(-t/\tau_i)}) \cdot e^{(-t/\tau_f)} + (T_{final} - T_0)(1 - e^{(-t/\tau_f)}), \tag{4.13}$$

where $T_{initial} = T_{final} = 300K$ are initial and final temperatures, T_{peak} corresponds to a maximum simulation temperature. Another two parameters in this analytical expression involve time τ_i, which defines the rise time of the temperature to its maximum, and τ_f which is the relaxation time of temperature from T_{peak} to T_{final}. We assume that electron and spin temperature follow the same profile defined by relation (4.13). The value of the peak temperature, T_{peak}, represents the laser fluence, and is an important parameter, as it defines the respond of the system. Sufficiently large values of T_{peak} may disrupt any magnetization reversal by introducing large thermal disorder in the spin system and simply demagnetizing it. We have tested the possibility of the magnetization reversal with respect to the intensity of the simulated laser pulse given by peak temperature, T_{peak} ($T_{peak} = 800, 1000$ and 2000 K). If the peak temperature is not sufficiently large ($T_{peak} = 800$ K), there is no magnetization reversal, and magnetic moments just quench to some fractions of their

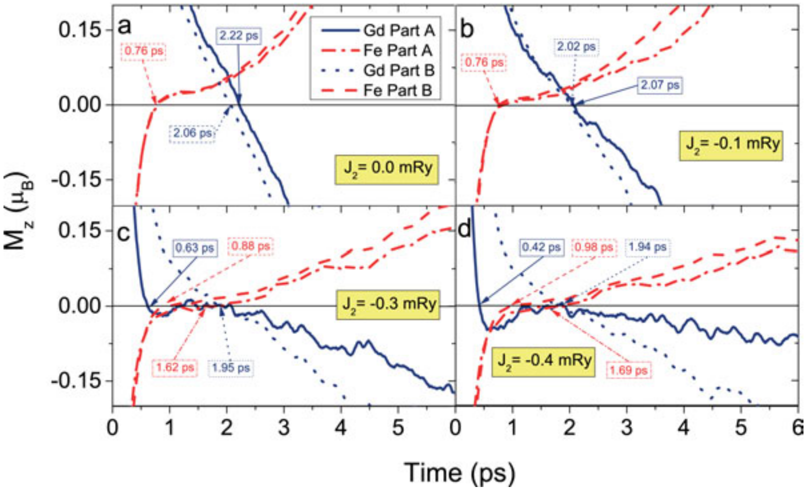

Figure 4.18. Magnetization profile (M_z) for Gd (blue) and Fe (red) sublattices for inhomogeneous samples. The magnetization of Gd rich-regions is shown as solid and dash-dot lines (Part A, $Gd_{0.30}Fe_{0.70}$) while Gd poor-regions are represented by dash and dot lines (Part B, $Gd_{0.22}Fe_{0.78}$). The strength of the second-nearest neighbour exchange parameter (J_2) for Gd rich-regions is different for any of the panels (a, b, c and d) outlined in the figure. For Gd poor-regions the J_2 values are considered as 0 mRy.

initial magnetic moment. If it is too large, as for $T_{peak} = 2000$ K, the system is brought to a state with zero net magnetization. However, for the intermediate temperatures, as for $T_{peak} = 1000$ K deterministic magnetization reversal occurs, and this is the peak temperature we used in further simulations. It is therefore essential to find appropriate laser fluence with respect to the strength of the exchange interaction for all-thermal switching to occur.

Table 4.4. *Degree of non-collinearity predicted by the current DFT calculations with and without spin-orbit (LS) coupling. The collected data represent the average (A) and maximal (M) angle deviation with respect to the z-axis of the magnetic moments on Gd and Fe atoms for amorphous* Gd_xFe_{1-x} *structures (*$x = 0.24, 0.50, 0.76$*).*

System	LS coupling				no LS coupling			
	Gd		Fe		Gd		Fe	
	A	M	A	M	A	M	A	M
$Gd_{0.24}Fe_{0.76}$	3.2°	35.1°	0.6°	1.7°	0.6°	13.6°	0.4°	2.2°
$Gd_{0.50}Fe_{0.50}$	0.6°	35.6°	0.6°	4.3°	0.4°	10.3°	0.3°	1.4°
$Gd_{0.76}Fe_{0.24}$	3.2°	35.8°	1.2°	5.7°	1.2°	17.2°	0.8°	3.2°

From temporal magnetization evolution in amorphous Gd_xFe_{1-x} ($x = 0.22 - 0.30$) alloys constructed by means of classical molecular dynamics simulations, we observed initial reversal of Fe sublattice, followed by switching of

Gd moments, in complete agreement with initial experimental findings [13]. Here, the sample with Gd concentration $x = 0.21$ is out of consideration since it does not exhibit a compensation point. As an example, for 24 at.% and 30 at.% of Gd (shown in Figure 4.17) we obtain that Fe and Gd sublattices demagnetize within 3 ps, while Fe switches its magnetization faster (within 1 ps, depending on the alloys composition), following by Gd reversal about 2 ps later. Therefore, the two magnetic sublattices switch their magnetization through formation of a transient state for 1-2 ps followed by relaxation to the new equilibrium magnetic order. Smaller (larger) Gd concentrations correspond to a smaller (larger) life time of the transient state. It was also argued [231] that for all-thermal switching it is crucial to have the initial temperature below the compensation point T_M, however, in the light of our results for Gd-Fe alloys, this proposed requirement does not seem to be valid.

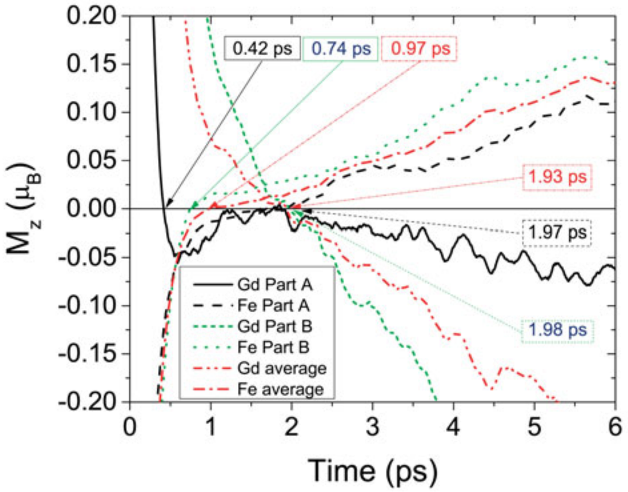

Figure 4.19. Magnetization profile (M_z) for Gd and Fe sublattices for inhomogeneous concentration profiles in a sample with average concentration $Gd_{0.24}Fe_{0.76}$. The magnetization of the Gd rich regions (Part A), Gd poor regions (Part B) and sample average is shown in black, green and red lines, respectively. The strength of the next nearest neighbour exchange parameter (J_2) for the Gd sublattice was -0.4 in this simulation. The figure show also similarities with experimental data reported in Fig. 3c of Ref.[14].

Another experimental investigation reported a non-uniform concentration profile of $Gd_{0.24}Fe_{0.665}Co_{0.095}$ alloys, resulting in some nanoregions about 10-20 nm in size with increased Gd or Fe concentrations compared to the average concentrations in the sample [14]. These regions, referred to as Gd-rich and Fe-rich regions, showed an opposite magnetization dynamics with Gd sublattice switching its magnetization faster than Fe in the Gd-rich regions, while

Fe-rich regions had the same temporal evolution of magnetization in the average sample. As inhomogeneity can be fundamental to switching, as shown in Ref. [14] we proceeded with the modelling of the inhomogeneous Gd-Fe sample. For this, we generated amorphous structures with concentration profiles, such that some regions had enhanced (depleted) Gd (Fe) concentrations with respect to the nominal concentration. To study the effect of chemical inhomogeneity of the structure we considered composition of $Gd_{0.24}Fe_{0.76}$, again ignoring the presence of Co in the experimental samples. Parts of the constructed compositionally inhomogeneous sample are referred to as Part A (Fe-rich region) and Part B (Gd-rich region). In these simulations, we have also considered different degrees of non-collinearity on the Gd sublattice. Such description is justified by our first-principle calculations, which show a certain degree of non-collinearity in the Gd magnetic sublattice (Table 4.3). The exchange driven non-collinear ground state at 0 K become even more pronounced when the spin-orbit coupling is taken into account. Thus, unlike to widely accepted in literature model of *S*-state Gd having a negligibly small magnetic anisotropy [165], we obtain an opposite trend, with the degree of non-collinearity in the rare-earth Gd sublattice enhanced as compared to that of the transition metal one. Since the effect of non-collinearity is significant for Gd, it is the rare-earth sublattice for which we expect larger Dzyaloshinskii-Moriya interaction, which favor canted magnetic configurations.

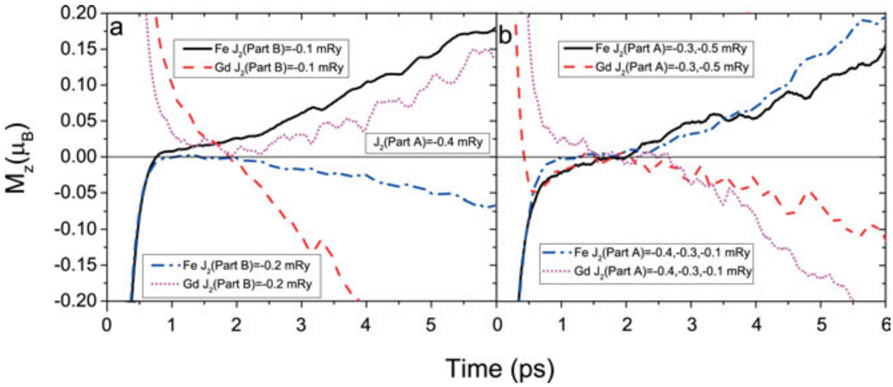

Figure 4.20. Magnetization profile (M_z) for Gd and Fe sublattices for inhomogeneous concentration profiles in a sample with average concentration $Gd_{0.24}Fe_{0.76}$. a) The SNN exchange interaction (J_2) in the Gd-poor region (Part B) has been chosen to be -0.1 and -0.2 mRy while in the Gd-rich region (part A) J_2=-0.4 mRy. b) Two sets of J_2 parameters distributed randomly over the Gd-rich region. The values of J_2 parameters are listed in the insets of the figure.

The microscopic Dzyaloshinskii-Moriya interaction considered here is the antisymmetric exchange interaction related to local violation of the inversion symmetry, which is the typical case in amorphous materials. To model

Dzyaloshinskii-Moriya interaction, we introduce a frustration into the magnetic system via a next-nearest-neighbor exchange parameter J_2 with antiferromagnetic character ($J_2 < 0$). The results of the atomistic spin dynamics simulations for several distinct values of J_2 are summarized in Figure 4.18. Our results reproduce experimental findings, i.e. magnetization dynamics in case of a small degree of non-collinearity is similar to that obtained for the homogeneous sample (Figure 4.18 (a),(b)), which shows all-thermal switching with Fe sublattice switching its magnetization before Gd. Increasing the strength of J_2 causes magnetization reversal on the Gd sublattice before Fe (Figure 4.18 (c),(d)). Hence there is a threshold for the value of $J_2 = -0.3$ mRy to induce faster magnetization reversal on the rare-earth magnetic sublattice. Figure 4.19 shows temporal evolution of magnetization in the different regions of the inhomogeneous sample with overall agreement with the experimental work [14]. We observe that in the Gd-rich regions Gd sublattice switches faster ($\tau = 0.42$ ps) than the Fe ($\tau = 1.97$ ps), while the process is reversed in Fe-rich regions. These results are based on the homogeneous distribution of J_2 between the second nearest neighbors. However, one would argue, that such distribution of next nearest neighbor exchange parameters J_2 is not physical taking into account the stochastic structure of amorphous Gd-Fe alloys and dependence of exchange couplings on distance. Therefore, to study the effect of inhomogeneous distribution of Dzyaloshinskii-Moriya vectors, we performed additional simulations where J_2 were distributed randomly between second nearest neighboring atomic pairs such that its mean value $J_2 = -0.4$ mRy (see Figure 4.20 (b)). As a result, we obtain that an inhomogeneous distribution of J_2 can favor a faster magnetization reversal on Gd sublattice only if all exchange couplings are above the threshold value of $J_2 = -0.3$ mRy. Values of J_2 below threshold value completely eliminates the switching behavior (Figure 4.20 (a)).

The explanation proposed in the experimental study on inhomogeneous GdFeCo [14] is based on the assumption of the existence of spin currents from Fe-rich regions which transfer torque to the Gd-rich regions. Here, we do not explicitly consider any spin currents and our analysis is purely based on the consideration of exchange effects. Therefore, we propose an explanation based on a mechanism driven by combination of Dzyaloshinskii-Moriya interaction and exchange frustration that we model by next nearest exchange interaction between rare-earth Gd in Gd-rich regions.

5. Summary and Outlook

In this thesis a number of functional materials such as shape-memory alloys, triboactive coatings, as well as amorphous ferrimagnets for data storage devices have been addressed from first principles. Various underlying microscopic structures, ranging from perfectly crystalline to completely disordered, is one of the keys to the great diversity of the properties of these materials. To summarize, we briefly review the main results presented in the thesis and discuss possible directions for future research.

- The mechanism behind the diffusionless martensitic transition in shape-memory AuZn is addressed from the density functional perturbation theory, as well as from phenomenological approach based on Landau theory of phase transitions. The coupling between the anomaly in the phonon dispersion relations and Fermi surface nesting is shown to drive the phase transition from the parent $B2$ phase to the low-temperature martensite. Pressure-induced stabilization of the high-temperature $B2$ structure of AuZn hints a possibility of the formation of the global minimum in the potential energy surface at low temperatures, which due to the strong electron-phonon coupling suggests a superconducting state. We also pinpoint the computational challenges associated with the proper description of lattice dynamics in this highly anharmonic Hume-Rothery phase.

  As a continuation of this work, it could be interesting to address Fermi surface changes, especially, regarding the nesting feature, as a result of temperature-induced atomic disorder. A possible alteration in the Fermi surface topology can be, in practice, investigated using the molecular dynamics simulations for a supercell of $B2$ AuZn and further reconstruction of the Fermi surface by backfolding of the electronic band structure. Phenomenological approach to the martensitic phase transition in this shape memory alloy can be also expanded by recalling the fact that, typically, martensitic phase transitions involve strain. Hence, considering the potential energy surface as a function of two order parameters, i.e. phonon amplitude of the acoustic TA_2 mode and the strain, might be helpful in understanding the structural transition in this alloy.

- We investigated the origin of the ferroelectric-like phase transition in the metallic perovskite oxide $LiOsO_3$ by means of molecular dynamics simulations. Theoretical study of this material is mainly driven by the fundamental understanding of the mechanism behind this, by far, sole realization of the Andersen and Blount's idea, i.e. a possibility of the ferroelectric-like structural transition in the metallic state. We find that at high temperatures the centrosymmetric $R\overline{3}c$ phase is dynamically stabilized by anharmonic effects. Further, our simulations show, that above the experimental phase transition temperature, the ferroelectric-like $R3c$ phase develops a collective shift in the Li atomic positions towards the centrosymmetric one, i.e transforming to the high-temperature structure.

Recent theoretical studies have predicted that a multiferroic can be designed by constructing a superlattice of the non-magnetic metallic $LiOsO_3$ and polar dielectric $LiNbO_3$ [81]. It would be, hence, interesting to address various heterostructures of the metallic $LiOsO_3$ and other perovskites, such as ferroelectric $BaTiO_3$ and $SrTiO_3$, antiferromagnetic $LaFeO_3$ and others, in search for the new artificial multiferroics and other functional materials.

- The ultra-low friction in triboactive amorphous W-S-N thin film is found to be associated with its complex atomic structure and preformed WS_3 building blocks that are characteristic to WS_2 with outstanding lubricating properties. More important, we show the formation of the quasi-free N_2 molecules trapped inside the S cages. From the structural and Bader population analysis we find that the N_2 molecules are weakly bonded with other N_2 molecules and S atoms of the cages. Overall, we refer virtually vanishing friction in amorphous W-S-N to a dense and stable coating surface, and easy access of W and S atoms for a continuous formation of a low-friction WS_2 tribofilm. In addition, due to a weak bonding with the local environment, quasi-free N_2 molecules are easily released from amorphous W-S-N, and do not hinder the formation of the lubricating tribofilm.

  Amorphous W-S-N has been shown as a very promising triboactive coating yielding an extremely low-friction [12] due to formation of a TMDC WS_2 tribofilm. Molybdenum diselenides, $MoSe_2$, also belonging to the TMDC family, exhibits good lubricating properties [232]. In analogy to W-S-N, it would be interesting to investigate from first principles another ternary compounds such as Mo-Se-N/C, Mo-S-N/C and W-Se-N/C and address their atomic and electronic structures on microscopic level.

- Disorder on atomic level can also induce a non-trivial magnetic phenomena in ferromagnetic materials, e.g. an ultrafast magnetization reversal in Gd-Fe driven by femtosecond laser pulse. By employing various techniques, including stochastic quenching method, density functional theory and atomistic spin dynamics, we address the complex atomic structure of Gd-Fe ferrimagnet and model the response of the magnetic sublattice under the influence of femtosecond laser pulse. We also address chemical inhomogeneity in amorphous Gd-Fe and its influence on the magnetic response to the external excitation. Finally, a mechanism for the experimentally observed magnetization switching in Gd-Fe, based on a combination of the exchange frustration and Dzyaloshinskii-Moriya interaction is proposed.

Amorphous ferrimagnet GdFeCo is a unique material, regarding its potential application in data storage processing. Here, by applying different approximations and models, we could successfully reproduce the experimental finding and suggest a possible mechanism of ultrafast magnetization reversal in this material. However, many important issues have not been addressed so far, i.e. long-wavelength magnons and their coupling to atomic vibrations, as well as a distribution of exchange coupling parameters J_{ij}. Another interesting problem to address in the future is a direct calculation of the Dzyaloshinskii-Moriya interaction in amorphous magnetic systems.

The main results of this thesis can be also extended in several possible directions, in particular, by merging the fields of amorphous topologically disordered materials with our knowledge of collective excitations. The phonon is a quanta of collective atomic vibrations, which in a periodic lattice can be defined as a plane wave. In the amorphous structure one can not use notions of reciprocal space and periodicity, and as a result, atomic vibrations can no longer be described in terms of plane waves (normal modes). In noncrystalline materials collective excitations, which can be referred to as *quasi-phonons*, can have a sufficiently long lifetime only for the long wave length limit (small $\mathbf{q}$), where the stochasticity of the structure is averaged out. Another collective excitation, i.e. *spin waves*, has been experimentally observed in magnetic amorphous materials. Hence, a variation in the population of quasi-magnons in noncrystalline magnetic samples influenced by femtosecond laser pulses, would be quite an interesting topic to address. Heat transport in liquids (or amorphous materials) from first-principles can also be a possible direction of our work in future.

6. Sammanfattning på Svenska

Med funktionella material menar man sådana vars egenskaper skräddarsys för ett specifikt syfte. Dessa egenskaper uppstår som respons till en extern stimulans. Några exempel på funktionella material är minnesmetaller och magnetiska minnesmetaller, piezoelektricitet, och multiferroer. I denna avhandling behandlas en mängd olika funktionella material med många olika strukturella egenskaper och tillämpningsområden, allt från tribologi till magnetiska minnen. För att poängtera den atomära sammansättningens vikt för produktion och kontroll av de olika materialens egenskaper vid olika tillämpningar så är denna avhandling indelad i två delar. De två delarna skiljer sig åt genom att den underliggande atomära strukturen hos de undersökta systemen antingen är *kristallin* eller *amorf*.

Avhandlingens första del är helt ägnad åt de kristallina strukturerna metallisk β'-AuZn och perovskitoxiden $LiOsO_3$. Den första av dessa är representativ för en stor familj av minnesmetaller. Dessa material har ett stort användningsområde inom medicin där de används för att fånga upp "fritt vandrande" blodproppar i blodkärl, i termomekaniska och termostatiska apparater, liksom i flyg- och rymdindustrin där de t.ex. kan användas i rymdantenner som aktiveras genom att de värms upp av solstrålning [1, 2]. Minnesmetaller utmärker sig genom att de inre spänningarna helt återställer sig när de värms över en viss kritisk temperatur. Denna effekt är strukturellt associerad med en reversibel temperatur-, tryck- eller magnetiskt fältinduceard fasövergång och har observerats i många metalliska system, däribland Hume-Rothery faser (CuZn, AuZn, AuCd, etc.) och magnetiska Heuslerlegeringar (NiMnIn [3], NiFeGa [4], NiMnGa [5] etc.), vilket indikerar en samverkan mellan dynamiska elektron- och gitteregenskaper. Det är denna fråga vi behandlar för AuZn med hjälp av beräkningar utgående från första princip. Vi finner att kopplingen mellan Kohn-anomalin i fonondispersionen och Fermi-ytsnästningen är den drivande mekanismen bakom AuZn's strukturella fasövergången.

Perovskitoxiden $LiOsO_3$ är ett annat mycket regelbundet system och vårt intresse för detta material är rent fundamentalt eftersom $LiOsO_3$ genomgår en ferroeliktricitetslik fasövergång i det metalliska tillståndet. Vid en första anblick verkar en ferroelektisk fasövergång och ett metallsikt tillstånd vara inkompatibla med varandra eftersom ledningselektronerna bör skärma alla interna elektriska fällt. Trotts detta föreslog Anderson och Blount redan 1965 att vissa strukturella fasövergångar i metaller kan vara ferroelektriska [6]. Sådana "ferroelektriska" fasövergångar har nyligen observerats i det metalliska $LiOsO_3$ vilket gör det till den första kända manifestationen av Anderson och

Blounts idé [7]. Det finns för närvarande flera teorier som förklarar denna "ferroelektricitet" men fasövergångens typ (ordnad-oordnad eller förflyttad typ) och de gitterdynamiska egenskaperna vid ändliga temperaturer hos $LiOsO_3$ har ännu inte studerats. Utgående från första princip molekyldynamikssimulationer visar vi här den dynamiska stabiliseringen av högtemperatur $R\overline{3}c$-fasen via en anharmonisk effekt och undersöker mekanismen bakom den strukturella övergången.

Avhandlingens andra del behandlar teoretisk modellering och karakterisering av topologiskt oordnade material, dvs. amorfa material. Det finns många välkända industriella tillämpningar av amorfa material, t.ex. amorf Se-film för xerografiska fotoreceptorer i kopiatorer, ultratransparent glasfiber för optisk kommunikation, tunna Ge-Sb-Te filmer för DVD, amorf hydrerat kisel, a-Si:H, för solceller och tunnfilmstransistorer (TFT) [8]. Här fokuserar vi på två andra viktiga tillämpningsområden, tribologi och data minnen.

Först behandlar vi tillämpningar av amorfa material inom tribologi. Denna vetenskapsgren ängnar sig åt interaktioner mellan ytor i relativ rörelse och relaterade fenomen så som friktion, slitage och smörjning. Flytande smörjmedel är de äldsta kända exemplen av smörjmedel. Flytande smörjmedel som innehåller olika kemikaliska tillsatser är dock inte alltid de bästa valen i ingenjörsmässiga tillämpningar, speciellt vid extrema förhållanden. I dessa fall är användandet av en lågfriktionsbeläggning, dvs. ett solitt smörjmedel, optimalt. Övergångsmetalsdikalkogenider (TMDC) så som WS_2, MoS_2, etc. är välkända solida smörjmedel och deras lågfriktionsegenskaper beror på deras skiktade och starkt anisotropa atomstruktur [9, 10]. Ytterligare ämnen har kombinerats med TMDC:er för att åstadkomma en stabil yta som förenklar skapandet av WS_2 tribologisk film. Samtidigt introducerar höga halter av tillsatt N oordning i strukturen, så den blir amorf [11]. Det har visats att tunna amorfa W-S-N-filmer med ungefär 37 at.% N får ultralåg friktion genom att forma en WS_2 tribolisk film, dvs. ett tunt smörjlager som formas direkt i den tribologiska kontakten, med näst intill försvinnande friktion ($\mu < 0.003$) [12]. Vi kopplar den näst intill försvinnande friktionen i amorft W-S-N till den täta och stabila ytbeläggningen och enkel tillgång till W- och S-atomer för kontinuerlig formation av lågfriktions WS_2 tribologisk film. Dessutom visar vi att nästan en fjärdedel av N-atomerna i den amorfa matrisen är bundet i fria N_2-molekyler. På grund av den svaga kopplingen till den lokala omgivningen så frigörs dessa N_2-molekyler lätt från det amorfa W-S-N och förhindrar därför inte formationen av den smörjande tribologiska filmen.

Att lagra och hantera information i material för magnetiska minnen, där elektronens spin fungerar som informationsbärare, är en av anledningarna som motiverar studiet av spindynamik. Den hastighet med vilken spinnen kan vändas bestämmer hur snabbt information kan skrivas. Nuvarande magnetiska minnen har en karakteristisk magnetiseringsförändringstid som är i storleksordningen nanosekunder, vilket tillåter ungefär en miljard bitar at skrivas per sekund. För att uppnå snabbare förändring av spinnet kan starka magnetiska eller dämpfällt användas, men för industriella tillämpningar är ingen av dessa metoder att föredra. Ett annat sätt att kontrollera vändandet av spinnen är genom att använda en femtosekundslaserpuls så som i undersökningar av den amorfa ferromagneten GdFeCo [13]. I detta fall är den magnetiska förändringen termiskt inducerad och involverar inget extern magnetiskt fällt och möjliggör snabbare vändning av spinnen än nuvarande teknologier. Nyligen har två olika magnetiseringsdynamiker blivit experimentellt realiserade för Gd och Fe delgitter i GdFeCo system (med 9.5 at.% Co) där det beroende på homogeniteten hos den undersökta regionen antingen Gd eller Fe delgittren bytt magnetiseringsriktning först [14]. Dessa experiment antyder en möjlighet att manipulera magnetiska bitar med hjälp av femtosekundslaserpulser. I den sista delen av avhandlingen försöker vi förstå den mikroskopiska mekanismen bakom magnetiseringsförändringen i amorfa ferromagnetiska Gd-Fe-legeringar, vilken drivs av en femtosekundslaserpuls, och vi tar hänsyn till den underliggande topologiskt oordnade strukturen. Vi behandlar också en kemisk inhomogenitet i amorf Gd-Fe-legering och dess inverkan på den magnetiska responsen till den externa excitationen. Till sist föreslår vi en mekanism för den experimentellt observerade magnetiseringsförändringen i Gd-Fe som baseras på en kombination av utbytesfrustration och Dzyaloshinskii-Moriya växelverkan.

7. Acknowledgements

There are many people without whom this thesis would not have been possible. First and foremost, I would like to thank my supervisor Olle Eriksson for always helping me, for his endless optimism, for encouragement in time of need and for constant support. Thank you, Olle, I learnt a lot from you!

I would like to thank Jason Lashley for our fruitful collaboration on shape memory alloys. Also, I would like to sincerely acknowledge Igor Abrikosov and Olle Hellman for introducing me to TDEP.

I am grateful to you, Krisztina, for all our projects on amorphous materials. It has been a great journey!

Uppsala would not be so special place without many great people I met here. I want to express my gratitude to all my colleagues and friends in the Materials Theory group: Rafael, Yaroslav, Johan, Kristofer, Samara, Inka, Wei Wei, Anna, Johann, Jakob, Iulia, Diana, Sumanta, Vancho, Alex E., Rocio, Pablo, Ritwik, Amitava, Robert, Jonathan, Ralph, Barbara, Moyses, Kostas, Anders, Debora, Jan, Alex A., Marco, Simone, Sudip, Igor, Soumyajyoti, Anton, Swarup, Attila, Heike, Susanne, my roommates, Erna and Raghuveer, and many others - thank you for all the interesting discussions during tea/coffee breaks, for all the activities and for creating such a friendly environment!

Annica, Jonas and Biplab, a special thank to you for all the various courses I had an opportunity to take. I really enjoyed them!

Special thanks to Manuel, Pablo and Lars for proof-reading the thesis and providing valuable suggestions and criticism. You made this thesis better! Ett stort tack till dig, Kristofer, för din hjälp med Svensk sammanfattning!

Lars, thank you for all your kindness and friendship, and always answering tons of my stupid questions. Hope, we will have a common project in future! Manuel, thank you for all the scientific discussions we had, for all your funny stories and your cheerful attitude! Cecilia, thank you for our long-term friendship and random trips to Stockholm! Thank you Anton N. for everything! You are just a great friend!

I would also like to thank my landlady, Marie-Louise, for a warm atmosphere at home. Tusen tack till dig, Marie-Louise, för alla dina underbara blåbärs- och rabarberpajer!

Finally, I want to thank my mom for all her support and always being there for me.

References

[1] K.Otsuka and C.M.Wayman. *Shape memory materials*. Cambridge Univ. Press, 1998.

[2] C.M.Wayman. Some applications of shape-memory alloys. *JOM*, 32:129, 1980.

[3] Y.Sutou, Y.Imano, N.Koeda, T.Omori, R.Kainuma, K.Ishida, and K. Oikawa. Magnetic and martensitic transformations of NiMnX (X=In,Sn,Sb) ferromagnetic shape memory alloys . *Appl. Phys. Lett.*, 85:4358, 2004.

[4] K.Oikawa, T.Ota, T.Ohmori, Y.Tanaka, H.Morito, A.Fujita, R.Kainuma, K.Fukamichi, and K.Ishida. Magnetic and martensitic phase transitions in ferromagnetic NiâGaâFe shape memory alloys . *Appl. Phys. Lett.*, 81:5201, 2002.

[5] S.J.Murray, M.Marioni, S.M.Allen, R.C.O'Handley, and T.A.Lograsso. 6ferromagnetic NiâMnâGa. *Appl. Phys. Lett.*, 77:886, 2000.

[6] P.W.Anderson and E.I.Blount. Symmetry considerations on martensitic transformations: "ferroelectric" metals? . *Phys. Rev. Lett.*, 14:217, 1965.

[7] Y.Shi, Y.Guo, X.Wang, A.J.Princep, D.Khalyavin, P.Manuel, Y. Michiue, A. Sato, K.Tsuda, S.Yu, M.Arai, Y.Shirako, M.Akaogi, N.Wang, K.Yamaura, and A.T. Boothroyd. A ferroelectric-like structural transition in a metal . *Nat. Mater.*, 12:1024, 2013.

[8] K.Tanaka and K.Shimakawa. *Amorphous chalcogenide semiconductors and related materials*. Springer, New-York, Dodrecht, Heidelberg, London, 2011.

[9] P.D.Fleischauer. Fundamental aspects of the electronic structure, materials properties and lubrication performance of sputtered MoS_2 films. *Thin Solid Films*, 154:309, 1987.

[10] M.Chhowalla, H.S.Shin, G.Eda, L.-J.Li, K.P.Loh, and H.Zhang. The chemistry of two-dimensional layered transition metal dichalcogenide nanosheets. *Nature Chemistry*, 5:263, 2013.

[11] A.Nossa and A.Cavaleiro. The influence of the addition of C and N on the wear behaviour of W-S-C/N coatings. *Surface and Coatings Technology*, 142-144:984, 2001.

[12] F.Gustavsson, S.Jacobson, A.Cavaleiro, and T.Polcar. Ultra-low friction W-S-N solid lubricant coating. *Surface and Coatings Technology*, 232:541, 2013.

[13] I. Radu, K.Vahaplar, C.Stamm, T.Kachel, N.Pontius, H.A.Dürr, T.A.Ostler, J.Barker, R.F.L.Evans, R.W.Chantrell, A.Tsukamoto, A.Itoh, A.Kirilyuk, Th.Rasing, and A.V.Kimel. Transient ferromagnetic-like state mediating ultrafast reversal of antiferromagnetically coupled spins. *Nature*, 472:205, 2011.

[14] C.E.Graves, A.H.Reid, T.Wang, B.Wu, S. de Long, K.Vahaplar, I.Radu, D.P.Bernstein, M.Messerschmidt, L.Müller, R.Coffee, M.Bionta, S.W.Epp,

R.Hartmann, N.Kimmel, G.Hauser, A.Hartmann, P.Holl, H.Gorke, J.H.Mentink, A.Tsukamoto, A.Fognini, J.J.Turner, W.F.ASchlotter, D.Rolles, H.Soltau, L.Strüder, Y.Acremann, A.V.Kimel, A.Kirilyuk, Th.Rasing, J.Stöhr, A.O.Scherz, and H.A.Dürr. Nanoscale spin reversal by non-local angular momentum transfer following ultrafast laser excitation in ferrimagnetic GdFeCo. *Nature Materials*, 12:293, 2013.

[15] M.Born and R.Oppenheimer. Zur Quantentheorie der Molekeln . *Annalen der Physik*, 84(20):0457, 1927.

[16] P.Hohenberg and W.Kohn. Inhomogeneous electron gas. *Phys. Rev.*, 136(3B):864, 1964.

[17] W.Kohn and L.Sham. Self-consistent equations including exchange and correlation effects. *Phys. Rev.*, 140(4A):1133, 1965.

[18] H.Eschrig. *The fundamentals of density functional theory*. Teubner-Texte zur Physik, 1996.

[19] J.P.Perdew and A.Zunger. Self-interaction correction to density-functional approximations for many-electron systems. *Phys. Rev. B*, 23:5048, 1981.

[20] J.P.Perdew and Y.Wang. Accurate and simple analytic representation of the electron-gas correlation energy. *Phys. Rev. B*, 45:13244, 1992.

[21] J.P.Perdew, K.Burke, and M.Ernzerhof. Generalized gradient approximation made simple. *Phys. Rev. Lett.*, 77:3865, 1996.

[22] J.Phillips and L.Kleinman. New method for calculating wave functions in crystals and molecules. *Phys. Rev.*, 116:287, 1959.

[23] W.E.Pickett. Pseudopotential methods in condensed matter applications. *Computer Physics Reports*, 9.

[24] S.Cottenier. *Density functional theory and the family of (L)APW-methods: a step-by-step introduction*. 2nd edition, 2002-2013.

[25] D.Vanderbilt. Soft self-consistent pseudopotentials in a generalized eigenvalue formalism. *Phys. Rev. B*, 41:7892, 1990.

[26] P.E.Blöchl. Projector augmented-wave method. *Phys. Rev. B*, 50.

[27] D.Marx and J.Hutter. *Ab inio molecular dynamics: basic theory and advanced methods*. Cambridge university press, 2009.

[28] R.M.Martin. *Electronic Structure: Basic Theory and Practical Methods*. 2004.

[29] D.Frenkel and B.Smit. *Understanding Molecular Simulation: From Algorithms to Applications*. Academic Press (A division of Harcourt, Inc.), 2002.

[30] H.C.Andersen. Molecular dynamics simulations at constant pressure and/or temperature. *Journal of Chemical Physics*, 72.

[31] S.Nosé. A molecular dynamics method for simulations in the canonical ensemble. *Molecular Physics*, 52.

[32] M.Born and K.Huang. *Dynamical theory of crystal lattices*. Oxford University Press, 1954.

[33] W.Cochran. Theory of the lattice vibrations of germanium. *Proc. R. Soc. (London)*, 253.

[34] P.Y.Yu and M.Cardona. *Fundamentals of Semiconductors: Physics and Materials Properties*. Springer, 1996.

[35] S.Baroni, S. de Gironcoli, A. Dal Corso, and P. Giannozzi. Phonons and related crystal properties from density-functional perturbation theory. *Rev.*

Mod. Phys., 73:515, 2001.

[36] P.Giannozzi, S.Baroni, and N.Bonini et.al. QUANTUM ESPRESSO: a modular and open-source software project for quantum simulations of materials. *Journal of Physics: Condensed Matter*, 21.

[37] D.Alfe. PHON: A program to calculate phonons using the small displacement method. *Comput. Phys. Commun.*, 180:2622, 2009.

[38] O.Hellman, I.A.Abrikosov, and S.I.Simak. Lattice dynamics of anharmonic solids from first principles. *Phys. Rev. B*, 84.

[39] O.Hellman and I.A.Abrikosov. Temperature-dependent effective third-order interatomic force constants from first principles. *Phys. Rev. B*, 88.

[40] L.Landau and E.Lifshitz. *Statistical physics*. Oxford University Press, 1938.

[41] K.Bhattacharya. *Microstructure of martensite*. Oxford Univ. Press, 2003.

[42] G.B.Olson and H.Hartman. Martensite and life - displacive transformations as biological processes. *J. Physique*, 43:855, 1982.

[43] W.Falk and R.D.James. Elasticity theory for self-assembled protein lattices with application to the martensitic phase transition in bacteriophague T4 tail sheath. *Phys. Rev. E*, 73:011917, 2006.

[44] C.M.Wayman and J.D.Harrison. The origins of the shape memory effect. *JOM*, 41:26, 1989.

[45] A.Ölander. The crystal structure of AuCd. *Zeit. für Kristal.*, 83A:145, 1932.

[46] A.Ölander. An electrochemical investigation of solid cadmium-gold alloys. *J. Am. Chem. Soc.*, 54:3819, 1932.

[47] M.W.Burkart and T.A.Read. Diffusionless phase change in the indium-thallium system. *Journal of Metals, Trans. AIME*, 197:1516, 1953.

[48] H.C.Donkersloot and J.H.N. Van Vucht. Martensitic transformations in gold-titanium, palladium-titanium and platinum-titanium alloys near the equiatomic composition. *Journal of the Less Common Metals*, 20.

[49] W.J.Buehler, J.W.Clifrich, and R.C.Wiley. Effect of low-temperature phase changes on the mechanical properties of alloys near composition TiNi . *J. Appl. Phys.*, 34:1475, 1963.

[50] J.C.Lashley, H.Ledbetter, T.W.Darling, A.Saxena, A.Malinowski, M.F.Hundley, J.L.Smith, and D.J.Thoma. Free-energy density of the shape-memory alloy AuZn. *Materials Transactions*, 47:587, 2006.

[51] C.Zener. Contributions to the theory of β-phase alloys. *Phys. Rev.*, 71:846, 1947.

[52] G.Grimvall, B.Magyari-Köpe, V.Ozolinš, and K.A.Persson. Lattice instabilities in metallic elements. *Rev. Mod. Phys.*, 84:945, 2012.

[53] N.Ridley and H.Pops. Martensitic transformation in binary and ternary alloys based on the AuZn β'-phase. *Metallurgical Transactions*, 1:2867, 1970.

[54] H.Pops. Martensite in ternary CuZn-based β-phase alloys. *Trans. TMS-AIME*, 236:1532, 1966.

[55] P.A.Goddard, J.Singleton, R.D.McDonald, N.Harrison, J.C.Lashley, H.Harima, and M.-T.Suzuki. Catastrophic Fermi surface reconstruction in the shape-memory alloy AuZn. *Phys. Rev. Lett.*, 94:116401, 2005.

[56] J.C.Lashley, S.M.Shapiro, B.L.Winn, C.P.Opeil, M.E.Manley, A.Alatas, W.Ratcliff, T.Park, R.A.Fisher, B.Mihaila, P.Riseborough, E.K.H.Salje, and J.L.Smith. Observation of a continuous phase transition in a shape-memory

alloy. *Phys. Rev. Lett.*, 101:135703, 2008.

[57] T.Makita, A.Nagasawa, Y.Morii, N.Minakawa, and H.Ohno. Phonon dispersion relations of premartensite β'-phase in AuZn alloys. *Physica B*, 213-214:430, 1995.

[58] M.Sanati, R.C.Albers, T.Lookman, and A.Saxena. First-order versus second-order phase transformation in AuZn. *Phys. Rev. B*, 88:024110, 2013.

[59] H.Tietze, M.Mullner, and B.Renker. Dynamical properties of premartensitic NiTi. *J. Phys. C*, 17:L529, 1984.

[60] S.M.Shapiro, B.X.Yang, Y.Noda, L.E.Tanner, and D.Schryvers. Neutron-scattering and electron-microscopy studies of the premartensitic phenomena in Ni_xAl_{100-x} alloys. *Phys. Rev. B*, 44:9301, 1991.

[61] E.I.Isaev, A.I.Lichtenstein, Yu.Kh.Vekilov, E.A.Smirnova, I.A.Abrikosov, S.I.Simak, R.Ahuja, and B.Johansson. Ab initio phonon calculations for L12 Ni_3Al and B2 NiAl. *Solid. State. Commun.*, 129:809, 2004.

[62] T.Ohba. Study of martensitic transformation in AuCd alloys by means of neutron scattering and X-ray scattering. *Phase Transitions: A Multinational Journal*, 69:289, 1999.

[63] J.Kästner, W.Petry, S.M.Shapiro, A.Zheludev, J.Neuhaus, Th.Roessel, E.F.Wassermann, and H.Bach. Influence of atomic order on TA1 [110] phonon softening and displacive phase transition in $Fe_{72}Pt_{28}$ Invar alloys . *Eur. Phys. J. B*, 10:641, 1999.

[64] W.Kohn. Image of the Fermi surface in the vibration spectrum of a metal. *Phys. Rev. Lett.*, 2:393, 1959.

[65] G.L.Zhao and B.N.Harmon. Phonon anomalies in β-phase Ni_xAl_{1-x} alloys. *Phys. Rev. B*, 45:2818, 1992.

[66] S.B.Dugdale, R.J.Watts, J.Laverock, Zs.Major, M.A.Alam, M.Samsel-Czekałla, G.Kontrym-Sznajd, Y.Sakurai, M.Itou, and D.Fort. Observation of a strongly Nested Fermi Surface in the Shape-Memory Alloy $Ni_{0.62}Al_{0.38}$. *Phys. Rev. Lett.*, 96:2006, 046406.

[67] J.C.Lashley and S.M.Shapiro. Unpublished data.

[68] G.R.Barsch. Landau theory of the displacive phase transformations in gold-cadmium and titanium-nickel alloys. *Materials Science Forum*, 327-328:367, 2000.

[69] W.Cochran. Crystal stability and the theory of ferroelectricity. *Advances in Physics*, 9:387, 1960.

[70] I.A.Sergienko, V.Keppens, M.McGuire, R.Jin, J.He, S.H.Curnoe, B.C.Sales, P.Blaha, D.J.Singh, K.Schwarz, and D.Mandrus. Metallic "Ferroelectricity" in the Pyrochlore $Cd_2Re_2O_7$. *Phys. Rev. Lett.*, 92:2004, 065501.

[71] M.Tachibana, N.Taira, H.Kawaji, and E.Takayama-Muromachi. Thermal properties of $Cd_2Re_2O_7$ and $Cd_2Nb_2O_7$ at the structural phase transitions. *Phys. Rev. B*, 82:2010, 054108.

[72] T.Kolodiazhnyi, M.Tachibana, H.Kawaji, J.Hwang, and E.Takayama-Muromachi. Persistence of Ferroelectricity in $BaTiO_3$ through the Insulator-Metal Transition. *Phys. Rev. Lett.*, 104:2010, 147602.

[73] C.Paduani and C.A.Kuhnen. Martensitic phase transition from cubic to tetragonal V_3Si: an electronic structure study. *Eur. Phys. J. B*, 66:353, 2008.

[74] L.R.Testardi. Structural instability and superconductivity in A-15 compounds.

Rev. Mod. Phys., 47:637, 1975.

[75] I.-K.Jeong, S.Lee, S.-Y.Jeong, C.J.Won, N.Hur, and A. Llobet. Structural evolution across the insulator-metal transition in oxygen-deficient $BaTiO_3$-delta studied using neutron total scattering and Rietveld analysis . *Phys. Rev. B*, 84:064125, 2011.

[76] H.Boysen and F.Altorfer. A neutron powder investigation of the high-temperature structure and phase transition in $LiNbO_3$. *Acta Cryst. B*, 50:405, 1994.

[77] H.Sim and B.G.Kim. First-principles study of octahedral tilting and ferroelectric-like transition in metallic $LiOsO_3$. *Phys. Rev. B*, 89:201107, 2014.

[78] G.Giovannetti and M.Capone. Dual nature of the ferroelectric and metallic state in $LiOsO_3$. *Phys. Rev. B*, 90:195113, 2014.

[79] H.M.Liu, Y.P.Du, Y.L.Xie, J.-M.Liu, C.-G.Duan, and Xiangang Wan. Metallic ferroelectricity induced by anisotropic unscreened Coulomb interaction in $LiOsO_3$. *Phys. Rev. B*, 91:064104, 2015.

[80] H.Xiang. Origin of polar distortion in $LiNbO_3$-type “ferroelectric” metals: role of A-site instability and short-range interactions. *Phys. Rev. B*, 90:094108, 2014.

[81] D.Puggioni, G.Giovannetti, M.Capone, and J.M.Rondinelli. Design of a Mott Multiferroic from a Nonmagnetic Polar Metal. *Phys. Rev. Lett.*, 115:087202, 2015.

[82] R.Zallen. *The physics of amorphous solids*. 1998.

[83] K.Klement, R.H.Willens, and P.Duwez. Non-crystalline structure in solidified gold-silicon alloys. *Nature*, 187:1960, 869.

[84] L.Greer. Metallic glasses. *Science*, 267:1947, 1995.

[85] A.L.Greer. Confusion by design. *Nature*, 366:303, 1993.

[86] J.Schroers. Glasses made from pure metals. *Nature*, 512:142, 2014.

[87] L.Zhong, J.Wang, H.Sheng, Z.Zhang, and S.X.Mao. Formation of monoatomic metallic glasses through ultrafast liquid quenching. *Nature*, 512:177, 2014.

[88] W.L.Johnson. Bulk glass-forming metallic alloys: science and technology. *MRS Bulletin*, 24:42, 1999.

[89] D.Turnbull and J.C.Fisher. Rate of nucleation in condensed systems. *J. Chem. Phys.*, 17:71, 1949.

[90] M.Wuttig and N.Yamada. Phase-change materials for rewriteable data storage. *Nature Materials*, 6:824, 2007.

[91] W.Kauzmann. The nature of the glassy state and the behavior of liquids at low temperatures. *Chemical Reviews*, 43(2):219, 1948.

[92] L.Pauling. The principles determining the structure of complex ionic crystals. *J. Am. Chem. Soc.*, 51:1010, 1929.

[93] H.W.Sheng, W.K.Luo, F.M.Alamgir, J.M.Bai, and E.Ma. Atomic packing and short-to-medium-range order in metallic glasses. *Nature*, 439:419, 2006.

[94] K.Binder and D.W.Heerman. *Monte Carlo simulations in statistical physics*. Springer Verlag 1997, 1997.

[95] R.L.McGreevy and L.Pusztai. Reverse Monte Carlo simulation: a new technique for the determination of disordered structures. *Mol. Simulat.*, 1:359, 1988.

[96] R.M.Wentzcovitch, C. da Silva, J.R.Chelikowsky, and N.Binggeli. A new

phase and pressure induced amorphization in silica. *Phys. Rev. Lett.*, 80:2149, 1998.

[97] D.Hohl and R.O.Jones. First-principles molecular-dynamics simulation of liquid and amorphous selenium. *Phys. Rev. B*, 43:3856, 1991.

[98] A.Gambirasio and M.Bernasconi. Ab initio study of boron doping in tetrahedral amorphous carbon. *Phys. Rev. B*, 60:1999, 12007.

[99] J.Li and D.A.Drabold. First-principles molecular-dynamics study of glassy As_2Se_3. *Phys. Rev. B*, 61:11998, 2000.

[100] E.Kim, Y.H.Lee, J.J.Lee, and Y.G.Hwang. Defects in amorphous SiGe alloys an explanation of electron spin resonance signals. *Europhysics letters*, 40:147, 1997.

[101] X.Y.Zhao, D.Ceresoli, and D.Vanderbilt. Structural, electronic, and dielectric properties of amorphous ZrO_2 from ab initio molecular dynamics. *Phys. Rev. B*, 71:085107, 2005.

[102] G.Kresse and J.Hafner. Ab inito molecular-dynamics simulation of the liquid-metal - amorphous-semiconductor transition in germanium. *Phys. Rev. B*, 49:14251, 1994.

[103] D.C.Wallace. Statistical mechanics of monoatomic liquids. *Phys.Rev.E*, 56:4179, 1997.

[104] E.Holmström, N.Bock, T.B.Peery, R.Lizárraga, G.De Lorenzi-Venneri, E.D.Chisolm, and D.C.Wallace. Ab initio method for locating characteristic potential-energy minima of liquids. *Phys.Rev.E*, 80:051111, 2009.

[105] E.Holmström, N.Bock, T.Peery, E.Chisolm, R.Lizárraga, G.De Lorenzi-Venneri, and D.Wallace. Structure discovery for metallic glasses using stochastic quenching. *Phys.Rev.B*, 82:024203, 2010.

[106] K.Kádas, M.Andersson, E.Holmström, H.Wende, O.Karis, S.Urbonaite, S.M.Butorin, S.Nikitenko, K.O.Kvashnina, U.Jansson, and O.Eriksson. Structural properties of amorphous metal carbides: Theory and experiment. *Acta Materialia*, 60:4720, 2012.

[107] C.Arhammar, A.Pietzsch, N.Bock, Erik Holmström, C.M.Araujo, J.Gråsjö, S.Zhao, S.Green, T.Peery, F.Hennies, S.Amerioun, A.Föhlisch, J.Schlappa, T.Schmitt, V.N.Strocov, G.A.Niklasson, D.C.Wallace, J.-E.Rubensson, B.Johansson, and R.Ahuja. Unveiling the complex electronic structure of amorphous metal oxides. *PNAS*, 108:6355, 2011.

[108] C.M.Araujo, S.Nagar, M.Ramzan, R.Shukla, O.D.Jayakumar, A.K.Tyagi, Y.-S.Liu, J.-L.Chen, P.-A.Glans, C.Chang, A.Blomqvist, R.Lizárraga, E.Holmström, L.Belova, J.Guo, R.Ahuja, and K.V.Rao. Disorder-induced room temperature ferromagnetism in glassy chromites. *Scientific reports*, 4:4686, 2014.

[109] N.Axen, S.Hogmark, and S.Jacobson. Friction and wear measurement techniques. In Bharat Bhusan, editor, *Modern tribology handbook*. CRC Press, Oxford, 2000.

[110] Ali Erdemir. Boron-nased solid nanolubricants and lubrication additives. In Jean Michel Martin and Nobuo Ohmae, editors, *Nanolubricants*. Wiley, 2008.

[111] A.Erdemir, S.Li, and Y.Jin. Relation of Certain Quantum Chemical Parameters to Lubrication Behavior of Solid Oxides. *Int. J. Mol. Sci.*, 6:203, 2005.

[112] U.Mäkelä and J.Valli. Tribological properties of PVD TiN and TiC coatings.

Finnish J. Tribol., 4 (2):74, 1985.

[113] K.Miyoshi. Studies of mechanochemical interactions in the tribological behavior of materials. *Surf. Coat. Technol.*, 43-44:799, 1990.

[114] I.P.Hayward, I.L.Singer, and L.E.Seitzman. Effect of roughness on the friction of diamond on CVD diamond coatings. *Wear*, 157:215, 1992.

[115] A.Erdemir and Ch.Donnet. Tribology of diamond and diamond-like carbon films: an overview. In G.W.Stachowiak, editor, *Wear - Materials, Mechanism and Practice*. John Wiley and Sons, Ltd, 2005.

[116] F.P.Bowden and D.Tabor. *Friction and lubrication of solids*. Clarendon Press, 1950.

[117] K.Holmberg and A.Mathews. Coating tribology: a concept, critical aspects and future directions. *Thin Solid Films*, 253:173, 1994.

[118] T.Tokoya, T.Kiss, A.Chainani, S.Shin, M.Nohara, and H.Takagi. Fermi surface sheet-dependent superconductivity in 2H-NbSe$_2$. *Science*, 294:2518, 2001.

[119] B.Sipos, A.F.Kusmartseva, A.Akrap, H.Berger, L.Forró, and E.Tutiš. From Mott state to superconductivity in 1T-TaS$_2$. *Nature Materials*, 7:960, 2008.

[120] J.C.Meyer, A.G.Geim, M.I.Katsnelson, K.S.Novoselov, and S.Roth. The structure of suspended graphene sheets. *Nature*, 446:60, 2006.

[121] S.Bertolazzi, J.Brivio, and A.Kis. Stretching and breaking of ultrathin MoS$_2$. *ACS Nano*, 5:9703, 2011.

[122] A.Splendiani, L.Sun, Y.Zhang, T.Li, J.Kim, C.-Y.Chim, G.Galli, and F.Wang. Emerging photoluminescence in monolayer MoS$_2$. *Nano Letters*, 10:1271, 2010.

[123] K.F.Mak, C.Lee, J.Hone, J.Shan, and T.F.Heinz. Atomically thin MoS$_2$: a new direct-gap semiconductor. *Phys. Rev. Lett.*, 105:136805, 2010.

[124] T.Li and G.Galli. Electronic properties of MoS$_2$ nanoparticles. *J. Phys. Chem. C*, 111:16192, 2007.

[125] A.Kuc, N.Zibouche, and T.Heine. Influence of quantum confinement on the electronic structure of the transition metal sulfide of TS$_2$. *Phys. Rev. B*, 83:245213, 2011.

[126] Q.H.Wang, K.Kalantar-Zadeh, A.Kis, J.N.Coleman, and M.S.Strano. Electronics and optoelectronic of two-dimensional transition metal dichalcogenides. *Nature Nanotechnology*, 7:699, 2012.

[127] X.Xu, W.Yao, D.Xiao, and T.F.Heinz. Spin and pseudospin in layered transition metal dichalcogenides. *Nature Physics*, 10:343, 2014.

[128] I.L.Singer, S.Fayeulle, and P.D.Ehni. Wear behaviour of triode-sputtered MoS$_2$ coating in dry sliding contact with steel and ceramics. *Wear*, 195:7, 1996.

[129] T.Spalvins. Lubrication with sputtered MoS$_2$ films: principles, operation, and limitations. *Journal of Materials Engineering and Performance*, 1:347, 1992.

[130] T.Polcar and A.Cavaleiro. Review on self-lubricant transition metal dichalcogenide nanocomposite coatings alloyed with carbon. *Surface and Coatings Technology*, 206:686, 2011.

[131] A.A.Voevodin, J.P.O'Neill, and J.S.Zabinski. Nanocomposite tribological coatings for aerospace applications. *Surface and Coatings Technology*, 116-119:36, 1999.

[132] M.Remškar, A.Mrzel, Z.Skraba, A.Jesih, M.Ceh, J.Demšar, P.Stadelmann, F.Levévy, and D.Mihailovic. Self-assembly of subnanometer-diameter

single-wall MoS_2 nanotubes. *Science*, 292:479, 2001.

[133] M.Remškar. Inorganic nanotubes. *Advanced materials*, 16:1497, 2004.

[134] L.Rapoport, Yu.Bilik, Y.Feldman, M.Homyonfer, S.R.Cohen, and R.Tenne. Hollow nanoparticles of WS_2 as potential solid-state lubricants. *Nature*, 387:791, 1997.

[135] M.Chhowalla and G.A.J.Amaratunga. Thin films of fullerene-like MoS_2 nanoparticles with ultra-low friction and wear. *Nature*, 407:164, 2000.

[136] J.M.Martin, C.Donnet, and Th.Epicier Th.Le Monge. Superlubricity of molybdenum disulphide. *Phys.Rev.B*, 48:10583, 1993.

[137] A.R.Lansdown. *Molybdenum Disulphide Lubrication*. Elsevier, 1999.

[138] B.Deepthi, H.C.Barshilia, K.S.Rajam, M.S.Konchady, D.M.Pai, and J.Sankar. Mechanical and tribological properties of sputter deposited nanostructured Cr-WS_2 solid lubricant coatings. *Surface and Coatings Technology*, 205:1937, 2010.

[139] D.G.Teer, J.Hampshire, V.Fox, and V.Bellido-Gonzalez. The tribological properties of MoS_2/metal composite coatings deposited by closed field magnetron sputtering. *Surface and Coatings Technology*, 94-95:572, 1997.

[140] T.Spalvins. Frictional and morphological properties of Au-MoS_2 films sputtered from a compact target. *Thin Solid Films*, 118:375, 1984.

[141] K.J.Wahl, D.N.Dunn, and I.L.Singer. Wear behavior of Pb-Mo-S solid lubricating coatings. *Wear*, 230:175, 1999.

[142] A.Nossa and A.Cavaleiro. Tribological behaviour of N(C)-alloyed W-S films. *Tribol. Lett.*, 28:59, 2007.

[143] A.Nossa and A.Cavaleiro. Mechanical behaviour of W-S-N and W-S-C sputtered coatings deposited with a Ti interlayer. *Surface and Coatings Technology*, 163-164:552, 2003.

[144] A.Nossa and A.Cavaleiro. On the microstructure of tungsten disulfide films alloyed with carbon and nitrogen. *Thin Solid Films*, 484:389, 2005.

[145] T.Polcar, F.Gustavsson, T.Thersleff, S.Jacobson, and A.Cavaleiro. Complex frictional analysis of self-lubricant W-S-C/Cr coating. *Faraday Discussions*, 156:383, 2012.

[146] N.Schönberg. Ternary metallic phases in the Ta-C-N, Ta-C-O, and Ta-N-O Systems. *Acta Chem. Scand.*, 8:204, 1954.

[147] S.S.Lu and Y.L.Chang. The accurate evaluation of lattice spacings from back-reflection powder photographs. *Proc. Phys. Soc.*, 53:517, 1941.

[148] V.L.Kalikhman. Features of the crystal-structure,electrophysical properties, and model of the spectrum of the valence bands of layered compounds of the MoS_2 type. *Neorg. Mater.*, 19:1060, 1983.

[149] A.E. van Arkel. Über die Kristalstruktur der Verbindungen Manganfluorid, Bleijodid und Wolframsulfid. *Recl. Trav. Pays.-B*, 45:437, 1926.

[150] W.J.Schutte, J.L. De Boer, and F.Jellinek. Crystal structures of tungsten disulfide and diselenide. *J. Solid State Chem.*, 70:207, 1987.

[151] V.I.Khitrova. An electron-diffraction study of cubic tungsten nitride. *Kristallografiya*, 4:513, 1959.

[152] M.Yuki, T.Midorikawa, Y.Miyake, and Y.Nishibayashi. Synthesis and Protonolysis of Tungsten- and Molybdenum- Dinitrogen Complexes Bearing Ruthenocenyldiphosphines. *Organometallics*, 28:4741, 2009.

[153] K.Arashiba, K.Sasaki, S.Kuriyama, Y.Miyake, H.Nakanishi, and Y.Nishibayashi. Synthesis and Protonation of Molybdenum- and Tungsten-Dinitrogen Complexes Bearing PNP-Type Pincer Ligands. *Organometallics*, 31:2035, 2012.

[154] S.C.Abrahams. The crystal and molecular structure of orthorhombic sulfur. *Acta Crystallogr.*, 8:661, 1955.

[155] B.D.Sharma and J.Donohue. The crystal and molecular structure of sulfur nitride, S_4N_4. *Acta Crystallogr.*, 16:891, 1963.

[156] E.J.Friebele, D.L.Griscom, M.Stapelbroek, and R.A.Weeks. Fundamental defect centers in glass: the peroxy radical in irradiated, high-purity, fused silica. *Phys. Rev. Lett.*, 42:1346, 1979.

[157] A.R.Beal and W.Y.Liang. Excitons in 2H-WSe_2 and 3R-WS_2. *J.Phys.C: Solid State Phys.*, 9:2459, 1976.

[158] A.Inoue, Y.Bizen, H.M.Kimura, T.Masumoto, and M.Sakamoto. Compositional range, thermal stability, hardness and electrical resistivity of amorphous alloys in Al-Si (or Ge)-transition metal systems. *J.Mater.Sci.*, 23:3640, 1988.

[159] S.T.Oyama. *Chemistry of Transition Metal Carbides and Nitrides*. Blackie Academic and Professional, Glasgow, 1996.

[160] N.Turova. *Inorganic Chemistry in Tables*. Springer-Verlag, Berlin Heidelberg, 2011.

[161] J.M.Martin, H.Pascal, C.Donnet, T. Le Mongue, J.L.Loubet, and T.Epicier. Superlubricity of MoS_2: crystal orientation mechanisms. *Surf. Coat. Technol.*, 68-69:427, 1994.

[162] J.M.D.Coey. Amorphous magnetic order. *J.Appl.Phys*, 49:1646, 1978.

[163] G.Marchal, P.Mangin, M.Piecuch, and C. Janot. Mössbauer study of magnetic ordering in amorphous Fe-Si alloys. *J.Physicque*, 37:763–768, 1976.

[164] J.Chappert, R.Arresse-Boggiano, and J.M.D.Coey. Appearance of magnetism in amorphous Y_{1-x} Fe_x. *J.Magnetism Magnetic Materials*, 1978.

[165] R.Harris, M.Plischke, and M.J.Zuckermann. New model for amorphous magnetism. *Phys. Rev. Lett.*, 31:160–162, 1973.

[166] In J.A.Fernandez-Baca and W.-Y.Ching, editors, *The Magnetism of Amorphous Metals and Alloys*. World Scientific Pub Co Inc, 1995.

[167] J . Stöhr and H.C. Siegmann. *Magnetism.* Springer, Berlin, Heidelberg, 2006.

[168] Th.Gerrits, H.A.M. van den Berg, J.Hohlfeld, L.Bär, and Th.Rasing. Ultrafast precessional magnetization reversal by picosecond magnetic field pulse shaping. *Nature*, 418:509, 2002.

[169] L. Berger. Emission of spin waves by a magnetic multilayer traversed by a current. *Phys. Rev. B*, 54:9353–9358, 1996.

[170] J. C. Slonczewski. Current-driven excitation of magnetic multilayers. *J. Magn. Magn. Mat.*, 159:L1–L7, 1996.

[171] E. Beaurepaire, J.-C. Merle, A. Daunois, and J. Y. Bigot. Ultrafast spins dynamics in ferromagnetic nickel. *Phys. Rev. Lett.*, 76:4250, 1996.

[172] E.Carpene, E.Mancini, C.Dallera, M.Brenna, E.Puppin, and S. De Silvestri. Dynamics of electron-magnon interaction and ultrafast demagnetization in thin iron films. *Phys. Rev. B*, 78:174422, 2008.

[173] M.Vomir, L.H.F.Andrade, L.Guidoni, E.Beaurepaire, and J.-Y.Bigot. Real

space trajectory of the ultrafast magnetization dynamics in ferromagnetic fetals. *Phys. Rev. Lett.*, 94:237601, 2005.

[174] A. Vaterlaus, T. Beutler, and F. Meier. Spin-lattice relaxation time of ferromagnetic gadolinium determined with time-resolved spin-polarized photoemission. *Phys. Rev. Lett.*, 67:3314â3317, 1991.

[175] E. Kojima, R. Shimano, Y. Hashimoto, S. Katsumoto, Y. Iye, and M. Kuwata-Gonokami. Observation of the spin-charge thermal isolation of ferromagnetic $Ga_{0.94}Mn_{0.06}As$ by time-resolved magneto-optical measurements. *Phys. Rev. B*, 68:193203, 2003.

[176] J. Wang, Y. C. Sun, J. Hashimoto, G. Kono, A. Khodaparast, L. Cywinski, L. J. Sham, G. D. Sanders, C. J. Stanton, and H.Munekata. Dynamics of photo-enhanced magneto-crystalline anisotropy in diluted ferromagnetic GaMnAs. *J. Phys.: Condens. Matter*, 18:R501, 2006.

[177] A. V. Kimel, R. V. Pisarev, J. Hohlfeld, and Th. Rasing. Ultrafast Quenching of the Antiferromagnetic Order in $FeBO_3$: Direct Optical Probing of the Phonon-Magnon Coupling. *Phys. Rev. Lett.*, 89:287401, 2002.

[178] T. Kise, T. Ogasawara, M. Ashida, Y. Tomioka, Y. Tokura, and M. Kuwata-Gonokami. Ultrafast Spin Dynamics and Critical Behavior in Half-Metallic Ferromagnet: Sr_2FeMoO_6. *Phys. Rev. Lett.*, 85:1986, 2000.

[179] Q. Zhang, A. V. Nurmikko, G. X. Miao, G. Xiao, and A.Gupta. Ultrafast spin-dynamics in half-metallic CrO_2 thin films. *Phys. Rev. B*, 74:064414, 2006.

[180] M. van Kampen, C. Jozsa, J. T. Kohlhepp, P. LeClair, L. Lagae, W. J. M. de Jonge, and B. Koopmans. All-Optical Probe of Coherent Spin Waves. *Phys. Rev. Lett.*, 88:227201, 2002.

[181] G.Ju, J.Hohfeld, B.Bergman, R.J.M. Van de Veerdonk, O.N.Mryasov, J.-Y.Kim, X.Wu, D.Weller, and B.Koopmans. Ultrafast Generation of Ferromagnetic Order via a Laser-Induced Phase Transformation in FeRh Thin Films. *Phys. Rev. Lett.*, 93:197403, 2004.

[182] G. V. Astakhov, A. V. Kimel, G. M. Schott, A. A. Tsvetkov, A.Kirilyuk, D. R. Yakovlev, G. Karczewski, W. Ossau, G.Schmidt, L. W. Molenkamp, and Th. Rasing. Magnetization manipulation in (Ga,Mn)As by subpicosecond optical excitation. *Appl. Phys. Lett.*, 86:152506, 2005.

[183] T.Ogasawara, N.Iwata, Y.Murakami, H.Okamoto, and Y.Tokura. Submicron-scale spatial feature of ultrafast photoinduced magnetization reversal in TbFeCo thin film. *Appl. Phys. Lett.*, 94:162507, 2009.

[184] C.D.Stanciu, F.Hansteen, A.V.Kimel, A.Kirilyuk, A.Tsukamoto, A.Itoh, and Th.Rasing. All-optical magnetic recording with circularly polarized light. *Phys. Rev. Lett.*, 99:047601, 2007.

[185] N.Ogawa, S.Seki, and Y.Tokura. Ultrafast optical excitation of magnetic skyrmions. *Scientific Reports*, 5:9552, 2015.

[186] A. Kirilyuk and Th. Rasing. Magnetization-induced-second-harmonic generation from surfaces and interfaces. *J. Opt. Soc. Am. B*, 22:148–167, 2005.

[187] C. Stamm, T. Kachel, N. Pontius, R. Mitzner, T. Quast, K.Holldack, S. Khan, C. Lupulescu, E. F.Aziz, M. Wietstruk, H.A. Dürr, and W. Eberhardt. Femtosecond modification of electron localization and transfer of angular momentum in nickel. *Nature Mater.*, 6:740, 2007.

[188] B.Koopmans, M. van Kampen, J.T.Kohlhepp, and W.J.M. de Jonge. Ultrafast

magneto-optics in nickel: magnetism or optics? *Phys. Rev. Lett.*, 85:844, 2000.

[189] F.Dalla Longa, J.T.Kohlhepp, W.J.M. de Jonge, and B.Koopmans. Influence of photon angular momentum on ultrafast demagnetization in nickel. *Phys. Rev. B*, 75:224431, 2007.

[190] D. M. Edwards and J. A. Hertz. Electron-magnon interactions in itinerant ferromagnetism. II. Strong ferromagnetism. *J. Phys. F: Met. Phys.*, 3:2191, 1973.

[191] V. P. Zhukov and E. V. Chulkov. The femtosecond dynamics of electrons in metals. *Phys. Usp.*, 52:105, 2009.

[192] R. J. Elliott. Theory of the effect of spin-orbit coupling on magnetic resonance in some semiconductors. *Phys. Rev.*, 96:266, 1954.

[193] Y. Yafet. g Factors and spin-lattice relaxation of conduction electrons. *Solid State Physics*, 14, 1963.

[194] D. Steiauf and M. Fähnle. Elliott-Yafet mechanism and the discussion of femtosecond magnetization dynamics. *Phys. Rev. B*, 79:140401, 2009.

[195] B.Koopmans, G.Malinowski, F.Dalla-Longa, D.Steiauf, M. Fähnle, T.Roth, M.Cinchetti, and M.Aeschlimann. Explaining the paradoxical diversity of ultrafast laser-induced demagnetization. *Nature Materials*, 9:259–265, 2010.

[196] M.Battiato, K.Carva, and P.M.Oppeneer. Superdiffusive spin transport as a mechanism of ultrafast demagnetization. *Phys. Rev. Lett.*, 105:027203, 2010.

[197] D. Rudolf, C. La o Vorakiat, M. Battiato, R. Adam, J. M. Shaw, E. Turgut, P. Maldonado, S. Mathias, P. Grychtol, H. T. Nembach, T. J. Silva, M. Aeschlimann, H. C. Kapteyn, M. M. Murnane, C. M.Schneider, and P. M. Oppeneer. Ultrafast magnetization enhancement in metallic multilayers driven by superdiffusive spin current. *Nat. Commun.*, 3:1037, 2012.

[198] A. Eschenlohr, M. Battiato, P. Maldonado, N. Pontius, T. Kachel, K. Holldack, R. Mitznerand, A. Föhlisch, P. M. Oppeneer, and C. Stamm. Ultrafast spin transport as key to femtosecond demagnetization. *Nat. Mater.*, 12:332, 2013.

[199] E. Turgut, Chan La−o−vorakiat, J. M. Shaw, P. Grychtol, H. T.Nembach, D. Rudolf, R. Adam, M. Aeschlimann, C. M. Schneider, T. J. Silva, M. M. Murnane, H. C. Kapteyn, and S. Mathias. Controlling the competition between optically induced ultrafast spin-flip scattering and spin transport in magnetic multilayers. *Phys.Rev. Lett.*, 110:197201, 2013.

[200] A. J. Schellekens, W. Verhoeven, T. N. Vader, and B. Koopmans. Investigating the contribution of superdiffusive transport to ultrafast demagnetization of ferromagnetic thin films. *Appl. Phys. Lett.*, 102:252408, 2013.

[201] P.Hansen. Thermomagnetic switching in amorphous rare-earth transition-metal alloys with high compensation temperature. *J.Appl.Phys.*, 63:2364, 1988.

[202] P.Chaudhari, J.J.Cuomo, and R.J.Gambino. Amorphous metallic films for magneto-optic applications. *Appl.Phys.Lett.*, 22:337, 1973.

[203] A.E.Clark. High-field magnetization and coercivity of amorphous rare-earth-Fe_2 alloys. *Appl.Phys.Lett.*, 23:642, 1973.

[204] N.Heiman, K.Lee, and R.I.Potter. Exchange coupling in amorphous rare earth-iron alloys. *AIP Conference Proceedings*, 29:130, 1976.

[205] J.J.Rhyne, J.H.Schelleng, and N.C.Koon. Anomalous magnetization of amorphous $TbFe_2$, $GdFe_2$, and YFe_2. *Phys.Rev.B*, 10:4672, 1974.

[206] P.Hansen, C.Clausen, G.Much, M.Rosenkranz, and K.Witter. Magnetic and

magneto-optical properties of rare-earth transitionâmetal alloys containing Gd, Tb, Fe, Co. *J.Appl.Phys.*, 66:756, 1989.

[207] M.Aeschlimann, A.Vaterlaus, M.Lutz, M.Stampanoni, F.Meier, H.C.Siegmann, S.Klahn, and P.Hansen. High-speed magnetization reversal near the compensation temperature of amorphous GdTbFe. *Appl. Phys. Lett.*, 59:2189, 1991.

[208] J.H.Mentink, J.Hellsvik, D.V.Afanasiev, B.A.Ivanov, A.Kirilyuk, A.V.Kimel, O.Eriksson, M.I.Katsnelson, and Th.Rasing. Ultrafast spin dynamics in multisublattice magnets. *Phys.Rev.Lett.*, 108:057202, 2012.

[209] J.Barker, U.Atxitia, T.A.Ostler, O.Hovorka, O.Chubykalo-Fesenko, and Chantrell R.W. Two-magnon bound state causes ultrafast thermally induced magnetisation switching. *Scientific Reports*, 3:3262, 2013.

[210] T.A.Ostler, J.Barker, R.F.L.Evans, R.W.Chantrell, U.Atxitia, O.Chubykalo-Fesenko, S.El Moussaoui, L. Le Guyader, E.Mengotti, L.J.Heyderman, F.Nolting, A.Tsukamoto, A.Itoh, D.Afanasiev, B.A.Ivanov, A.M.Kalashnikova, K.Vahaplar, J.Mentink, A.Kirilyuk, Th.Rasing, and A.V.Kimel. Ultrafast heating as a sufficient stimulus for magnetization reversal in a ferrimagnet. *Nature Communications*, 3:666, 2012.

[211] B.Skubic, J.Hellsvik, L.Nordström, and Olle Eriksson. A method for atomistic spin dynamics simulations: implementation and examples. *J.Phys.:Cond.Matt.*, 20:315203, 2008.

[212] L.D.Landau and E.M.Lifshitz. On the theory of the dispersion of magnetic permeability in ferromagnetic bodies. *Phys. Z. Sowjet*, 8:153–169, 1935.

[213] S.Mizukami, S.Iihama, N.Inami, T.Hiratsuka, G.Kim, H.Naganuma, M.Oogane, and Y.Ando. Fast magnetization precession observed in $L1_0$-FePt epitaxial thin film. *Appl.Phys.Lett.*, 98:052501, 2011.

[214] T.L.Gilbert. A phenomenological theory of damping in ferromagnetic materials. *IEEE Transactions on magnetics*, 40:3443, 2004.

[215] R.Kubo and N.Hashitsume. Brownian motion of spins. *Prog.Theor.Phys.Suppl.*, 46:210, 1970.

[216] J.H.Mentink, M.V.Tretyakov, A.Fasolino, M.I.Katsnelson, and Th.Rasing. Stable and fast semi-implicit integration of the stochastic Landau-Lifshitz equation. *J.Phys.:Condens. Matter*, 22:176001, 2010.

[217] K.Yano, E.Kita, K.Tokumitsu, H.Ino, and A.Tasaki. Magnetic Properties of Amorphous Fe_{100-x} Gd_x ($18 \leq X \leq 70$) Alloys. *IEEE Trans. J. Magnetics Japan*, 7:943, 1992.

[218] F. H. Spedding, J. J. Hanak, and A. H. Daane. High temperature allotropy and thermal expansion of the rare-earth metals. *Journ. of the Less-Common Metals*, 3:110, 1961.

[219] Z. S. Basinski, W. Hume-Rothery, and A. L. Sutton. The lattice expansion of iron. *Proc.Roy. Soc. London Ser. A*, 229:459, 1955.

[220] J. F. Smith and D. A. Hansen. The structures of YNi_3, YCo_3, $ThFe_3$ and $GdFe_3$. *Acta Cryst.*, 19:1019, 1965.

[221] F. Endter and W. Klemm. Die Kristallstrukturen von Fe_2Gd und Mn_2Gd. *Z. Anorg. Chem.*, 252:377, 1944.

[222] V. Petkov, K. Yano, and E. Kita. Atomic-scale structure of Gd_xFe_{100x} melt-quenched amorphous alloys (x= 22, 33, 56) by X-ray diffraction. *Phys.*

Stat. Sol. (a), 157:365, 1996.

[223] W. M. Brown, P. Wang, S. J. Plimpton, and A. N. Tharrington. Implementing molecular dynamics on hybrid high performance computersâshort range forces. *Comp. Phys. Comm.*, 182:898, 2011.

[224] N. X. Chen, J. Shen, and X. P. Su. Theoretical study on the phase stability, site preference, and lattice parameters for Gd(Fe, T)$_{12}$. *J. Phys.: Condens.Matter*, 13:2727, 2001.

[225] J. Inoue and M. Shimizu. Electronic structure and magnetic properties of Y-Co, Y-Fe and Y-Mn intermetallic compounds. *J. Phys. F: Met. Phys.*, 15:1525, 1985.

[226] T.A.Ostler, R.F.L.Evans, R.W.Chantrell, U.Atxitia, O.Chubykalo-Fesenko, I.Radu, A.Abrudan, F.Radu, A.Tsukamoto, A.Itoh, A.Kirilyukand T.Rasing, and A.Kimel. Crystallographically amorphous ferrimagnetic alloys: comparing a localized atomistic spin model with experiments. *Phys. Rev. B*, 84:024407, 2011.

[227] M. E. Fisher and M. N. Barber. Scaling theory for finite-size effects in the critical region. *Phys. Rev. Lett.*, 28:1516, 1972.

[228] K. Binder. Finite size scaling analysis of Ising model block distribution functions. *Z. Phys. B-Condensed Matter*, 43:119, 1981.

[229] Y. Mimura, N. Imamura, T. Kobayashi, A. Okada, and Y. Kushiro. Magnetic properties of amorphous alloy films of Fe with Gd, Tb, Dy, Ho, or Er. *J. Appl. Phys.*, 49:1208, 1978.

[230] E.Jäger. Structure fluctuations in the molecular field theory of amorphous ferrimagnets. *Phys.Status Solidi B*, 80:K81, 1977.

[231] R.Medapalli, I.Razdolski, M.Savoini, A.R.Khorsand, A.Kirilyuk, A.V.Kimel, Th.Rasing, A.M.Kalashnikova, A.Tsukamoto, and A.Itoh. Efficiency of ultrafast laser-induced demagnetization in Gd$_x$Fe$_{100-x-y}$Co$_y$ alloys. *Phys. Rev. B*, 86:054442, 2012.

[232] Temperature dependence of tribological properties of MoS2 and MoSe2 coatings. *Surface and Coatings Technology*, 193:230, 2005.

[233] D.Marx and J.Hutter. *Ab initio Molecular Dynamics: Basic Theory and Advanced Methods*. Cambridge University Press, 2009.

[234] Y.Murakami and S.Kachi. Lattice softening and phase stability of CuZn, AgZn and AuZn β-phase alloys. *Japanese Journal of Applied Physics*, 71:846, 1947.

[235] W.Webb. A study of beta-brass in single crystal form. *Phys. Rev.*, 55:297, 1939.

[236] S.Raymond, J.Bouchet, G.H.Lander, M. Le Tacon, G.Garbarino, M.Hoesch, J.-P.Rueff, M.Krisch, J.C.Lashley, R.K.Schulze, and R.C.Albers. Understanding the complex phase diagram of uranium: the role of electron-phonon coupling. *Phys. Rev. Lett.*, 107:136401, 2011.

[237] J.C.Lashley and M. Häggblad Sahlberg. . *private communication*.

[238] N.M.Renevier, N.Lobiondo, V.C.Fox, D.G.Teer, and J.Hampshire. Performance of MoS$_2$/metal composite coatings used for dry machining and other industrial applications. *Surface and Coatings Technology*, 123:84, 2000.

[239] I. Tudosa, C. Stamm, A. B. Kashuba, F. King, H. C. Siegmann, J. Stöhr, G. Ju, B. Lu, and D. Weller. The ultimate speed of magnetic switching in granular recording media. *Nature*, 428:831–833, 2004.

[240] M. B. Agranat, S. I. Ashitkov, A. V. Kirillin, V. E. Fortov, S. I. Anisimov, A. B. Granovskii, and P. S. Kondratenko. Dynamics of first- and second-order phase transitions in amorphous magnetooptic TbFeCo films. *JETP Lett.*, 67:953–958, 1998.

[241] J.-W. Kim, K.-D. Lee, J.-W. Jeong, and S.-C. Shin. Ultrafast spin demagnetization by nonthermal electrons of TbFe alloy film. *Appl.Phys. Lett.*, 94:192506, 2009.

Acta Universitatis Upsaliensis

Digital Comprehensive Summaries of Uppsala Dissertations from the Faculty of Science and Technology 1276

Editor: The Dean of the Faculty of Science and Technology

A doctoral dissertation from the Faculty of Science and Technology, Uppsala University, is usually a summary of a number of papers. A few copies of the complete dissertation are kept at major Swedish research libraries, while the summary alone is distributed internationally through the series Digital Comprehensive Summaries of Uppsala Dissertations from the Faculty of Science and Technology. (Prior to January, 2005, the series was published under the title "Comprehensive Summaries of Uppsala Dissertations from the Faculty of Science and Technology".)

Distribution: publications.uu.se
urn:nbn:se:uu:diva-260704

ACTA
UNIVERSITATIS
UPSALIENSIS
UPPSALA
2015